



Skolkovo Institute of Science and Technology

Skolkovo Institute of Science and Technology

VANADIUM REDOX FLOW BATTERIES MODELING AND
PERFORMANCE ANALYSIS

Doctoral Thesis

by

MIKHAIL PUGACH

DOCTORAL PROGRAM IN ENGINEERING SYSTEMS

Supervisor

Assistant Professor Aldo Bischi

Moscow - 2020

© Mikhail Pugach 2020

I hereby declare that the work presented in this thesis was carried out by myself at Skolkovo Institute of Science and Technology, Moscow, except where due acknowledgement is made, and has not been submitted for any other degree.

Mikhail Pugach
Assistant Prof. Aldo Bischi

Abstract

Batteries are the key technology for the sustainable development of electrical grids with a high share of renewable power generation. Among different battery technologies, Vanadium Redox Flow Batteries (VRFB) are considered one of the most promising solutions for large-scale energy storage systems suitable for integration with renewables. Despite its competitive features (e.g., low self-discharge and long lifetime), the VRFB technology is still relatively young. Thus, the ways to better exploit their potential are still under investigation. VRFB modeling helps to achieve a better understanding of VRFB systems, simulates their behavior estimating and optimizing their performance for different applications before constructing expensive experimental facilities.

However, to date, VRFB models are either too complicated, thus computationally demanding and not suitable for fast calculations needing real-time feedback, or oversimplified, thus not reflecting the peculiarities of VRFB technology. Hence, the development of modeling tools that would be a bridge between these two extremes is a decisive point for designing reliable and efficient VRFB systems. In this study, a computationally efficient 0-D model has been developed, targeting optimal balance between computational complexity and accuracy. The model is based on the general conservation principles of charge and mass transfer; hence it can simulate a wide range of VRFB systems with different sizes and specifications. The key feature of the model is the accurate simulation of internal processes based on analytical solutions. Such an approach

allows obtaining high accuracy (average error of less than 5%) while having low computational complexity simulating dynamic VRFB behavior in real-time.

Leveraging upon the developed model, a methodology for estimation of the key VRFB characteristics under different operating conditions is proposed. The method is based on a set of simplified correlations that allow estimating VRFB rated power, capacity and operation time directly from the geometry of stack and tank without detailed numerical simulation of the battery. The proposed methodology improves state of the art, allowing to determine the battery power and capacity with an accuracy of 94% and define optimal VRFB usage protocols avoiding over/underestimation of committed battery energy and power. In addition, the model is deployed to design a feedback control strategy for electrolyte flow rate regulation. The proposed control ensures stable battery operation in a wide range of loads providing required battery performance at flow rates reduced by two times than the existing solutions, thus decreasing pumping losses by more than three times.

To sum up, the modeling approaches developed in this work enable a better understanding of the main VRFB intrinsic features to determine the proper constraints for battery design and operating conditions necessary for long service life and reliable battery operation.

Publications

1. Pugach M, Parsegov S, Gryazina E, Bischi A. Output feedback control of electrolyte flow rate for Vanadium Redox Flow Batteries. *J Power Sources* 2020;455:227916. doi:10.1016/j.jpowsour.2020.227916.
2. Pugach M, Vyshinsky V, Bischi A. Energy efficiency analysis for a kilowatt class vanadium redox flow battery system. *Appl Energy* 2019;253:113533. doi:10.1016/j.apenergy.2019.113533.
3. Pugach M, Kondratenko M, Briola S, Bischi A. Zero dimensional dynamic model of vanadium redox flow battery cell incorporating all modes of vanadium ions crossover. *Appl Energy* 2018;226:560–9. doi:10.1016/j.apenergy.2018.05.124.
4. Pugach M, Kondratenko M, Briola S, Bischi A. Numerical and experimental study of the flow-by cell for Vanadium Redox Batteries. *Energy Procedia* 2017;142:3667–74. doi:10.1016/j.egypro.2017.12.260.

Acknowledgments

First of all, I would like to thank my supervisor, Prof. Aldo Bischi, for giving me the opportunity to work under this challenging topic, supporting my ideas, guiding for their realization and believing in me.

Also, I would like to thank my co-supervisor, Prof. Keith Stevenson, for introducing me to this topic, giving valuable advices and supporting me through the whole PhD. His course was a milestone in my research, forming a critical understanding of the main processes in the VRFB systems.

I would like to express my gratitude to Prof. Victor Vyshinsky, Prof. Elena Gryazina, Dr. Mikhail Kondratenko and Dr. Sergei Parsegov for their support, interesting collaborative work and co-supervision in some phases of my work.

I would like to thank my colleagues from the Center of Energy Systems and Technologies with whom we shared our challenges, had interesting scientific discussions, learned from each other and helped each other.

I also would like to express my gratitude to my family and my friends. They have always been with me, supporting in all difficult moments, believing in me and giving me strength.

Table of Contents

Abstract.....	3
Publications	5
Acknowledgments	6
List of Symbols, Abbreviations.....	10
List of Figures.....	16
List of Tables.....	22
Chapter 1. Introduction.....	24
1.1 Objectives of the work	26
1.2 Thesis structure	27
1.3 Scientific novelty	29
Chapter 2. Electricity storage: why vanadium?.....	31
2.1 Introduction.....	31
2.2 Main types of ESS	33
2.3 ESS application.....	35
2.4 Technical indicators of ESS.....	37
2.5 Redox Flow Batteries.....	44
2.6 Vanadium redox battery (VRFB).....	52
2.7 VRFB capital cost.....	54
2.8 Conclusions.....	56

Chapter 3. Mathematical modeling of VRFB systems	57
3.1 Introduction.....	57
3.2 Literature review	60
3.3 VRFB mathematical model.....	65
3.4 Energy performance indicators	74
3.5 Initial conditions	76
3.6 Numerical details	76
3.7 Experimental measurements and model validation	79
3.8 Results and discussion	81
3.9 Conclusions.....	90
Chapter 4. Energy losses analysis.....	93
4.1 Introduction.....	93
4.2 Mathematical model.....	98
4.3 Model validation	99
4.4 Simulated case studies	100
4.5 Performance indicators	104
4.6 Results and discussion	107
4.6.1 Voltage efficiency.....	110
4.6.2 Coulombic efficiency.....	116
4.6.3 Charge-discharge operation	119
4.7 Conclusions.....	126

Chapter 5. Control of electrolyte flow rate.....	129
5.1 Introduction.....	129
5.2 Timescales and three-stage flow rate control.....	136
5.3 Controller design.....	138
5.4 Mathematical model.....	140
5.5 Optimal OCV and reference trajectory	143
5.6 Results and discussion	150
5.6.1 Short-term operation and transient battery behavior	150
5.6.2 Long-term battery operation	152
5.7 Conclusions.....	158
Chapter 6. Conclusions.....	161
Bibliography	165
Appendix	187

List of Symbols, Abbreviations

A	matrix of the system of mass balance equations
A_{ch}	half-cell channels cross-section area [m ²]
A_{ed}	cross-section area of electrode's inlet [m ²]
A_m	electrode-membrane interface area [m ²]
BMS	battery management system
c	molar concentration [mol m ⁻³]
c_0	initial molar concentration of vanadium in the electrolyte [mol m ⁻³]
c_{ref}	referenced molar concentration [mol m ⁻³]
c_f	fixed sites molar concentration [mol m ⁻³]
CE	roundtrip coulombic efficiency [-]
D	diffusion coefficient [m ² s ⁻¹]
d_m	membrane thickness [m]
E	energy [J]
EE	roundtrip energy efficiency [-]
EU	electrolyte utilization [-]
F	Faraday constant [C mol ⁻¹]
FF	feedforward
H	height of the electrode [m]
j	current density [A cm ⁻²]
\bar{j}	dimensionless current density [-]

J	molar flux [$\text{mol m}^{-2} \text{s}^{-1}$]
I	current [A]
\mathbf{I}_4	identity matrix 4x4
k_i	integral gain
k_f	feedforward gain
k_m	mass transfer coefficient electrode-electrolyte interface [m s^{-1}]
k_p	proportional gain
L	length of the electrode [m]
n_{ce}	number of cells [-]
OCV	open circuit voltage [V]
P	permeability coefficient [$\text{m}^2 \text{s}^{-1}$]
$\langle P \rangle$	power averaged over the operation time [kW]
Δp	pressure drop [Pa]
PI	proportional-and-integral
Q	electrolyte flow rate [$\text{m}^3 \text{s}^{-1}$]
R_{ce}	cell equivalent electric resistance [Ω]
R	gas constant $\text{J K}^{-1} \text{mol}^{-1}$
R^*	equivalent electric resistance [Ω]
\vec{S}	vector of sources
SOC	state of charge

t	time [s]
T	ambient temperature [K]
u	electrolyte velocity [m s^{-1}]
$\langle U \rangle$	voltage averaged over the operation time [V]
U_{ce}	cell voltage [V]
U_{bat}	battery voltage [V]
U_{eq}	cell equilibrium potential [V]
U_0	redox couples standard reduction potential [V]
U_0^*	formal reduction potential [V]
V	volume [m^3]
VE	roundtrip voltage efficiency
$VRFB$	vanadium redox flow battery
w	width of the electrode [m]
z_i	valence of i-th ion [-]
\vec{x}	vector of concentrations
<i>greek symbols</i>	
α	first empirical constant in mass transfer coefficient
β	second empirical constant in mass transfer coefficient
γ	reversed volume of cell or stack [m^{-3}]
$\mathcal{E}^a_{ch/dis}$	charge or discharge coulombic efficiency [-]

$\varepsilon^{v\ ch/dis}$	charge or discharge voltage efficiency [-]
$\varepsilon^{e\ ch/dis}$	charge or discharge energy efficiency [-]
η_{act}	activation overvoltage [V]
η_{con}	concentration overvoltage [V]
η_{ohm}	ohmic overvoltage [V]
κ	permeability of porous electrode [m ²]
ξ	water electro-osmotic coefficient [-]
λ	water content coefficient
σ^m	membrane conductivity [s m ⁻¹]
θ	reversed volume of tank [m ⁻³]
τ	process duration [s]

acronyms, subscripts, superscripts

<i>bat</i>	battery
<i>ch</i>	charge
<i>calc</i>	calculated value
<i>chn</i>	channel
<i>contr</i>	controlled
<i>ce</i>	cell
<i>cr</i>	crossover
<i>dis</i>	discharge

<i>eff</i>	effective
<i>ed</i>	electrode
<i>exp</i>	experimental value
<i>i</i>	i-th vanadium ion
<i>in</i>	input
<i>init</i>	initial value
<i>m</i>	membrane
<i>max</i>	maximum
<i>min</i>	minimum
<i>ne</i>	negative electrode
<i>pe</i>	positive electrode
<i>out</i>	output
<i>opt</i>	optimal
<i>react</i>	reactant
<i>ref</i>	reference
<i>s</i>	stored
<i>tk</i>	tank
<i>th</i>	theoretical
<i>tot</i>	total
<i>van</i>	vanadium
2	V^{2+} ion

- 3 V^{3+} ion
- 4 VO^{2+} ion
- 5 VO_2^+ ion

List of Figures

- Fig. 1. The forecast for wind and power installations in 2030 and 2050 [1]
- Fig. 2. The forecast for stationary storage installations in 2030 and 2050 (IRENA) [1].
- Fig. 3. Different tasks of electrical energy storage in grids [25].
- Fig. 4. Capital cost of energy and power units for different storage technologies [25,26].
- Fig. 5. Energy and power density of different storage technologies [22].
- Fig. 6. Applicability of different stationary storage technologies [25].
- Fig. 7. Conventional battery operation during charge and discharge cycles.
- Fig. 8. Flow battery working scheme, namely Vanadium one.
- Fig. 9. Electrochemical cell construction [30]: end plate (1), current collector (2), graphite plate with channels (3), silicon gasket (4), porous electrode (5), membrane (6).
- Fig. 10. Flow-by and flow-through configurations.
- Fig. 11. VRFB cells stack.
- Fig. 12. Increase of RFB power and capacity.
- Fig. 13. Colors of vanadium electrolyte contained different vanadium ions [35].
- Fig. 14. Battery capacity in cycling operation [36].
- Fig. 15. VRFB capital cost structure for 1 MW/ 4 MWh system [38], PCS – power conditioning system (inverter, converter, battery management system).
- Fig. 16. Vanadium reserves in the world [39].

Fig. 17. Classification of modeling approaches, their applications and CPU time.

Fig. 18. Direction of current and diffusion flux in charge and discharge modes.

Fig. 19. Experimental setup: a) photo of the test bench (MSU lab); b) flow cell assembly scheme. The cell consisted of fixing plates (1), gold plated current collector plates (2), graphite polar plates (3) with double serpentine flow channels (8) having inlet-outlet openings located on the side faces of the plates (9), 25 μm thick PEEK gaskets (4), electrodes (5), 0.5 mm thick silicon gaskets (6) and a membrane (7).

Fig. 20. Discharge polarization curves for different electrolyte flowrates corresponding to initial SOC=0.5 (calc – calculations ($\alpha=2, \beta=0.7$); th – literature data [64] ($\alpha=1.6, \beta=0.4$))

Fig. 21. Experimental and simulated charge-discharge curves (exp – experimental data, calc (D) – calculations of crossover flux with only diffusion component, $Q_3 = 8.6 \cdot 10^{-7} \text{ m}^3 \text{ s}^{-1}$)

Fig. 22. Experimental and simulated charge-discharge curves (exp – experimental data; calc – calculations; $Q_3 = 8.6 \cdot 10^{-7} \text{ m}^3 \text{ s}^{-1}$)

Fig. 23. Contribution of crossover components to capacity decay: a) influence of crossover modes on the coulombic efficiency; b) share of crossover components in the capacity loss

Fig. 24. Experimental and theoretical efficiencies of a single VRFB cell for $Q_3 = 8.6 \cdot 10^{-7} \text{ m}^3 \text{ s}^{-1}$ and varying current density.

Fig. 25. Voltage of 1 kW-class VRFB stack in charge-discharge operation at fixed current density (exp – experimental data [109], calc – simulation results).

Fig. 26. The block-schema of proposed approach for estimation of the main VRFB characteristics.

Fig. 27. Effective amount of stored/released energy and capacity losses: a) charge process; b) discharge process

Fig. 28. Polarization curve with influence of internal processes depending on current density: exp – experimental data [111], calc – simulation results, OCV – open circuit voltage.

Fig. 29. Influence of internal processes on the battery voltage: a) charge; b) discharge; ohm – ohmic losses; conc – concentration losses; cros – crossover losses.

Fig. 30. Stack voltage efficiency at different charging and discharging current densities (red – charge mode, black – discharge mode).

Fig. 31. Contribution of internal processes to the voltage losses in the stack: a) charge; b) discharge (ohm – ohmic losses, conc – concentration losses, cros – crossover losses).

Fig. 32. Battery operation time at different charging and discharging current densities (blue – ideal case (no losses), red – simulations for charge mode, black – simulations for discharge mode).

Fig. 33. Coulombic efficiency (useable battery capacity) at different charging and discharging current densities (red – charge mode, black – discharge mode).

Fig. 34. Contribution of internal processes to the capacity decay during battery operation: a) charge; b) discharge (conc – concentration losses; cros – crossover losses).

Fig. 35. Current profiles and voltage curves for SC-SD and FC-FD operation modes: a) voltage profile (slow mode); b) voltage profile (fast mode); c) loading current (slow mode); d) loading current (fast mode).

Fig. 36. Energy required for battery charge and delivered to the grid during discharge: a) SC-SD mode; b) FC-FD mode; NS – numerical simulations; PR – proposed approach; ST – standard approach.

Fig. 37. Simplified battery usage profiles in different operation modes: a) slow mode; b) fast mode; NS – numerical simulations; PR – proposed approach; ST – standard approach.

Fig. 38. Current profiles and voltage curves for SC-FD and FC-SD operation modes: a) voltage profile SC-FD mode; b) voltage profile FC-SD mode; c) loading current SC-FD mode; d) loading current FC-SD mode.

Fig. 39. Energy required for battery charge and delivered to the grid during discharge: a) FC-SD mode; b) SC-FD mode; NS – numerical simulations; PR – proposed approach; ST – standard approach.

Fig. 40. Simplified battery usage profiles in mixed operation modes: a) SC-FC mode; b) FC-SD mode; NS – numerical simulations; PR – proposed approach; ST – standard approach.

Fig. 41. Grid connection of the battery. AC and DC are alternative and direct current, respectively; BMS – the battery management system; SOC – the battery state of charge.

Fig. 42. The battery response for a sudden change of the loading current: a) loading current profile; b) battery power at maximum (blue line) and minimum (red line) flow rates.

Fig. 43. Flowrate control system with proportional-and-integral (PI) and feedforward (FF) controllers.

Fig. 44. Parametric sweep calculations for varied flow rate at loading current $I = 100$ A, a) charge process, b) discharge process, c) zoom (charge), d) zoom (discharge); black dashed line – $Q_{\max} = 1.0 \text{ L s}^{-1}$; blue line – $Q_{\min} = 0.5 \text{ L s}^{-1}$; red dashed line – $Q_{\text{opt}} = 0.25 \text{ L s}^{-1}$;

Fig. 45. Sensitivity of battery OCV to the change of flow rate at fixed loading current, a) charge (SOC = 90%), b) discharge (SOC = 10%).

Fig. 46. Battery transient behavior in short-term charging operation: a) loading current; b) flow rate profile; c) battery OCV voltage.

Fig. 47. Battery transient behavior in short-term discharging operation: a) loading current; b) flow rate profile; c) battery OCV voltage.

Fig. 48. Battery operation in charging process at different flow rates: a) loading current; b) flow rates; c) reference and actual OCVs; d) battery power; green line – $Q_{\max} = 1.0 \text{ L s}^{-1}$; red line – $Q_{\min} = 0.05 \text{ L s}^{-1}$; blue line – Q_{contr} = the proposed control strategy.

Fig. 49. Battery operation in discharging process at different flow rates. a) loading current. b) flow rates. c) reference and actual OCVs. d) battery power; green line – $Q_{\max} = 1.0 \text{ L s}^{-1}$; red line – $Q_{\min} = 0.05 \text{ L s}^{-1}$; blue line – Q_{contr} = the proposed control strategy.

Fig. 50. Discharging process: a) loading current; b) flow rates; c) battery power; PR – control strategy proposed in this study; Li – control strategy proposed in [67].

Fig. A1. Membrane and coordinate direction.

List of Tables

- Table 1. Technical indicators of ESS [26,27].
- Table 2. The source term for mass transport equation [64,73,74].
- Table 3. Reactant concentration on the electrodes during charge and discharge.
- Table 4. Initial OCV for charge-discharge curves measured in experiments.
- Table 5. Specification of experimental setup and parameters in the simulation.
- Table 6. Specifications of the VRFB and parameters in the simulation [43].
- Table 7. The key VRFB parameters for different current densities.
- Table 8. Control strategies for flow rate regulation.
- Table 9. Three-stage control hierarchy.
- Table 10. Effect of different flow rate strategies on the main VRFB efficiency indicators.

“Per aspera ad astra”

Chapter 1. Introduction

The boom of renewable power generation requires new technological solutions to develop electrical grids with a stable power supply. The chaotic behavior of renewable energy sources requires large energy storage systems that can accumulate energy at high generation periods and release it when needed. In addition, several joint tasks related to power quality and grid optimization require the application of energy storage systems with flexible power ratings, high energy efficiency, long lifetime and high reliability. The International Renewable Energy Agency (IRENA) forecasts that for the pessimistic scenario, the installed power of wind plants will reach 2037 GW, and the power of solar plants will be around 1455 GW by 2030. For the optimistic case, these numbers will be nearly 1,5 times more: 3227 GW and 2526 GW, respectively [1]. Such high renewable power generation, even in the pessimistic scenario, will create a need for stationary storages with a total capacity of 370 GWh that is nearly 12 times larger of the capacity of all stationary storages in 2019. In the optimistic case, this number will be nearly two times higher, exceeding 740 GWh [1]. As a result, the development of new technologies that could be used for the construction of large scale stationary storages is highly important for the stable operation of future electric power grids.

Among different storage systems, the Redox Flow Batteries (RFB) are considered as one of the most promising technological pathways towards the development of large scale energy storage systems suitable for integration with renewables. RFB stores electrical

energy in the chemical form of electrolyte solutions converting it inside of electrochemical cells and storing the electrolytes in two separate external tanks. Thus, the energy and power are decoupled: applications requiring more energy only need larger volumes of the electrolytes, while more power can be obtained by adding more electrochemical cells. There are several types of RFB among which the Vanadium Redox Flow Batteries (VRFB) are the most matured technology that has already demonstrated rather good performance in the applications for large scale energy storage systems. Vanadispower flow batteries have been tested in Germany (0.3 MW / 1.3 MWh) [2] and in Italy (0.45 MW / 1.44 MWh) [3]; UniEnergy Technologies storage system was deployed at commercial scale in Washington, USA, for load leveling (2 MW / 8 MWh) [4]; Hokkaido Electric Power Co Inc (HEPCO) commercial solutions are currently under construction in Japan for intermittent balancing and load leveling [5].

Moreover, VRFB might be especially interesting for Russia, which is one of the top vanadium producers worldwide [6]. Thus, having a good excess to raw vanadium, Russia could produce very competitive VRFB systems that could be attractive both for internal and European markets.

Despite the competitive features, the VRFB technology is still rather young, and thus, there is no clear vision of how it can be leveraged for the specific tasks of electrical power grids. Modeling of VRFB is a strong tool that can provide a better understanding of VRFB systems, simulate their behavior and estimate their performance in the context of different application tasks before construction of expansive pilot plants and experimental

facilities. However, the models developed for simulation of VRFB systems to date are either too complex, and thus, applicable only for simulation of small lab-scale systems (several W) or too oversimplified and do not reflect the peculiarities of VRFB technology. As a result, the development of new modeling tools that would be a bridge between these two extremes is a key point for the further development of efficient VRFB systems.

1.1 Objectives of the work

This work aims to develop modeling tools for simulation of VRFB systems that should assist the researchers and engineers in better understanding of main VRFB intrinsic features and allow determining the proper constraints of battery design and operating conditions. Targeting that, the development of a mathematical model that would simulate dynamic VRFB behavior has been a thesis objective. Towards this respect, the model accuracy has always been considered together with a computational efficiency aiming at an optimal tradeoff between these two opposite entities. At the same time, the model flexibility has been set as another important criterion to simulate VRFB systems with different sizes and specifications. As a result, the model also has the long term objective to serve as a basis for the development of a methodology for the determination of proper battery usage protocols and control algorithm of internal VRFB parameters to improve battery efficiency and reliability. This is especially related to the development of VRFB systems with high efficiency, long service life and reliable operation.

1.2 Thesis structure

The current chapter gives an overview of the thesis, describes the general concept of the work, structure of the research and scientific novelty.

Chapter 2 describes the main trends in modern power systems and the central role of Electricity Storage Systems (ESS). A short overview of different storage technologies is presented. Their classification for different applications is performed considering their technical indicators. After that, the capital cost is discussed and the most promising ESS for large scale applications are highlighted, pointing out the VRFB as one of the most prospective technologies, especially concerning conventional batteries. The main advantages and disadvantages of the VRFB technology and its comparison with other storage systems is performed, showing a good potential of VRFB for the development of large scale storage systems.

Chapter 3 describes a zero-dimensional mathematical model of VRFB able to simulate its dynamic behavior under different operating conditions such as loading currents and electrolyte flow rates. The model is successfully validated with original experimental data. First, the general working principle of the VRFB systems is discussed and the fundamental physical processes taking place inside the battery are described. After that, a zero-dimensional model is derived and presented as a dynamical model for mass transfer between the cell and the tanks, and the electrochemical model for the battery voltage calculation. The key point of the presented model is a detailed simulation of crossover across the membrane that significantly improves the accuracy of the considered simulation

approach as compared to state of the art. The presented model is validated for different loading conditions demonstrating good agreement with experimental data (with an average error less than 5 %).

Chapter 4 is devoted to the investigation of the energy losses in the VRFB systems during their operation. First, an original methodology for estimation of the key battery characteristics is proposed. The method is based on a set of simplified correlations that allow estimating VRFB rated power, capacity and operation time directly from the geometry of stack and tank without detailed numerical simulations of the battery. The approach is verified with the data obtained by the numerical simulations within the validated model presented in Chapter 3. Such a simplified approach allows estimating battery performance separately in charging and discharging operation that can significantly improve the energy performance assessments of real VRFB systems. The proposed approach is validated considering the most representative cases of battery operation strategies related to slow and fast charge-discharge demonstrating high accuracy with an average deviation less than 6% regarding the results of detailed numerical simulations (the conventional approach with constant efficiencies demonstrated notably lower accuracy with an error of 40% for the same cases).

Chapter 5 is devoted to the development of a control strategy for electrolyte flow rate regulation. First, a methodology for the classification of flow rate control tasks is proposed. The methodology provides guidelines for the development of simple but robust feedback control algorithms based on the hierarchical control logic with the

implementation of multistage controller design. In addition, an original approach for the determination of optimal voltage reference is presented. The approach allows tuning the control algorithm according to specifications of the considered VRFB system without a thorough knowledge of hidden (not measurable) internal parameters and can be easily used for determination of optimal flow rates in real systems where the voltage reference can be determined from direct experimental measurements of charge-discharge curves at different flow rates. After that, a control algorithm for flow rate regulation is developed, relying on the dynamical model described in Chapter 3. The designed controller ensures stable battery operation under dynamic loading conditions tracking the reference trajectory with high accuracy (average error less than 0.0005%) while decreasing pumps energy consumption by more than three times as compared to the existing solutions.

Chapter 6 presents the conclusions of this work. The main results of the previous chapters are summarized, indicating their importance and future application.

1.3 Scientific novelty

- Development of an accurate zero-dimensional model for simulation of VRFB dynamic behavior under different operating conditions.
- Detailed simulation of crossover phenomenon using an analytical solution obtained in the framework of a macroscopic approach elaborating it with main modes of ions transport across the membrane adopted from microscopic models.

- Development of an approach for determination of mass transport coefficient on the surface of the electrode that allows simulating mass transport losses according to specifications of the electrodes and cell structure.

- Development of simplified and reliable (error less than 5 %) analytical approach for estimation of main battery indicators (rating power, capacity and time) at different loading conditions. The method is based on a set of simplified correlations that allow estimating VRFB rated power, capacity and operation time directly from the geometry of stack and tank without detailed numerical simulation of the battery.

- Design of efficient and robust feedback controller that ensures stable battery operation under drastically changing loads while minimizing flow rates, thus reducing pump losses and mechanical stress of the hydraulic system, and thus, improving the reliability of the VRFB. The control algorithm is designed in the framework of a multilevel control paradigm with the application of the original approach for the determination of optimal voltage reference.

Chapter 2. Electricity storage: why vanadium?

2.1 Introduction

Renewable energy generation has significantly increased in the last decay due to notable cost reduction, innovations and policy support. For example, the global installed power of wind plants had increased from 416 GW in 2015 to 624 GW in 2019 while the power of solar plants increased from 222 GW in 2015 to 583 GW in 2019 (Fig. 1). According to the forecast of the International Renewable Energy Agency (IRENA) published in April 2020 (Fig. 1), these numbers will significantly increase in the next decades. In the pessimistic scenario by 2030, the renewable generation will present nearly 20% of the total power generation with an installed power of solar and wind plants around 2037 GW and 1455 GW, respectively. In the optimistic scenario, the share of renewables is expected to reach 35%, and the installed power of solar and wind plants will grow to 3227 GW and 2526 GW, respectively [1]. In the scenario by 2050, for the pessimistic case, the wind and solar generation are expected to reach 4474 GW and 2434 GW respectively while, in the optimistic case, these numbers will be nearly doubled, reaching 8828 GW and 6044 GW. Such rapid expansion of renewable generation creates a need for a more flexible energy system to ensure reliable and cost-effective operation of power systems with large shares of variable renewable energy resources.

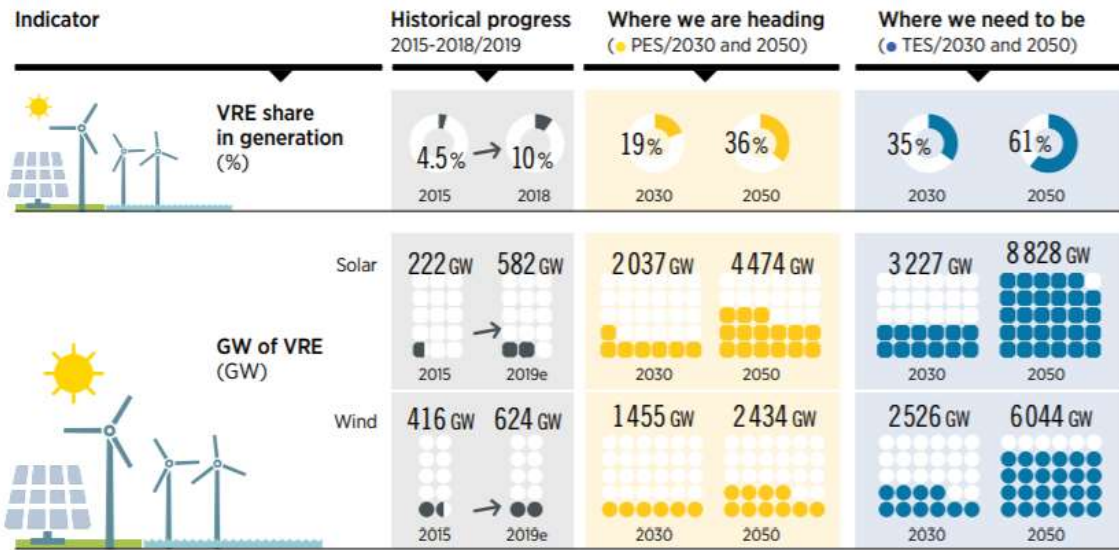


Fig. 1. The forecast for wind and power installations in 2030 and 2050 [1].

Electricity Storage Systems (ESS) is seen as a prominent solution to address many technical and economic challenges of renewables integration due to their unique capabilities to absorb, store and then reinject electricity. ESS can provide a wide range of services supporting solar and wind integration, also addressing some of the new challenges related to variability and uncertainty of solar and wind power generation. Thus, the boom of renewables is expected to lead to an increase in stationary ESS installations. In the pessimistic scenario, the global capacity is expected to reach 370 GWh by 2030 and 3400 GWh by 2050, while in the optimistic case, these numbers can be significantly larger: 745 GWh by 2030 and 9000 GWh by 2050 (Fig. 2) [1].



Fig. 2. The forecast for stationary storage installations in 2030 and 2050 (IRENA) [1].

In addition, ESS can participate in capacity and ancillary services markets, offering grid services related to primary and secondary reserves. Indirectly storage can support cost reduction, cutting down the need for generation and transmission capacity by reducing the need for peaking plants and easing line congestion. ESS can also support the integration of distributed renewables and the active participation of prosumers in demand management, reducing average electricity bills of households. Thus, ESS can efficiently provide multiple services simultaneously, improving reliability and increasing the profitability of power systems. In order to do that, ESS should have high efficiency, flexible design, long lifetime and high tolerance to instabilities of external conditions.

2.2 Main types of ESS

ESS technology refers to the process of converting energy from one form (mainly electrical energy) to the other form that can be stored in various mediums; then, the stored energy can be converted back into electrical energy when needed. Further, we consider the main types of technologies that have already shown their applicability for power systems services (that will be discussed in the next section). There are several suggested methods for the classification of various ESS technologies considering their functions, response

times, and suitable storage durations. One of the most widely used methods is based on the form of energy stored in the system, which can be categorized into:

Mechanical energy storage technologies (electricity at first is converted into mechanical energy and then stored as kinetic or potential energy). The main technologies of this type are represented by Pumped Hydro Storage (PHS) [7,8], Compressed air energy storage (CAES) [9] and Flywheels [10,11]. In PHS, the electricity is stored in the potential energy of water in the upper reservoir, while in CAES the energy is stored in the potential energy of compressed air and in Flywheels – in the kinetic energy of rotating wheels.

Chemical energy storage technologies (electricity is converted into potential energy of chemical compounds). Depending on the chemical process, there are several types of such storage technologies that in general can be called as Power-to-X (PtX): Power-to-Gas (PtG) that is based on the synthesis of gaseous fuels (e.g., methane) [12,13], Power-to-Liquids (PtL) with a synthesis of liquid fuels and Hydrogen based on the hydrogen produced by excess electricity within electrolysis [14,15]. The generated fuels and gases can be further used for the generation of electricity or in other parts of the industry as an energy source.

Electrical energy storage technologies (electricity is directly stored as the potential energy of electrostatic or magnetic fields). The main technologies of this type are presented by Super Capacitors (SC) and Superconducting Electromagnetic Storage (SMES). In SC, the electricity is stored in the potential energy of the electric field [16], while in SMES, the magnetic field is used instead [17,18].

Electrochemical energy storage technologies (electricity is stored as the potential energy of electrochemical reactions). The main technologies of this type are presented by conventional batteries and Redox Flow Batteries (RFB). The conventional batteries (e.g., Li-ion, Lead acid, NaS) are formed by solid electrodes (anode and cathode) composed of active species participating in electrochemical reactions [19], while in RFB, the reactants are contained in liquid electrolytes [20].

2.3 ESS application

Application of ESS technologies can be mainly classified into two large groups: energy applications related to larger storage capacity for long term oscillations (seasonal or daily) and power applications, larger rated power for mitigations of short-term fluctuations (e.g., below 15 minutes) [21,22].

The following tasks mainly present energy applications:

Intermittent balancing is a storage of energy for the smoothing instability of renewable energy sources (RES) by storing excess electricity at the periods of high generation and providing it into the grid when the generation is low. In this task, ESS is used to cover different variations of RES from hours to months.

Load leveling is a storage of excess electricity to distribute the load during the day storing energy at low consumption and injecting it in the grid at peak hours. Charging and discharging processes take place in long time ranges, and the amount of stored energy (charging) and produced energy (discharging) are relevant.

Time shifting (or Arbitrage) is the storage of electricity at a low price to use or sell during peak hours and thus increasing the revenue.

The following tasks mainly present power applications:

Peak shaving is a storage of excess electricity to fulfill the demand in peak hours [23], charging and discharging processes take place in short time ranges and the amount of stored energy (charging) and produced energy (discharging) are modest.

Primary frequency regulation is a reserve of generating systems (which are working in the idling regime, spinning reserve) for a grid to be able for fast response in case of an occasional fast increase in the generation (or decrease in load). ESS can be used instead of a spinning reserve [24].

Power quality is the storage of electricity to ensure a stable voltage and frequency in the power supply when the power grid has instabilities.

Depending on the required discharge time and rated power of the storage system, the described tasks can be presented by the area of the squares on the graph (Fig.3), where the red dashed line shows the area of RFB application that will be discussed in the next section (Sec. 2.4).

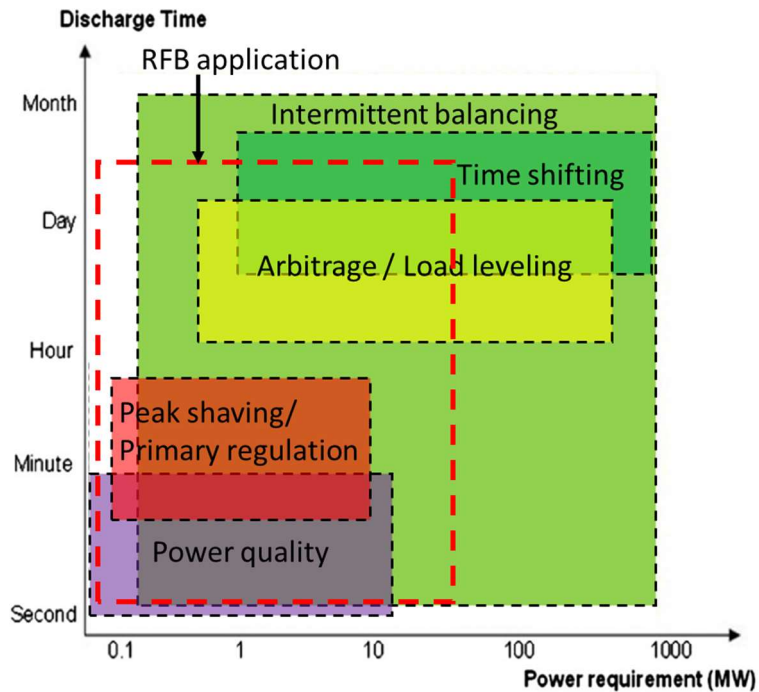


Fig. 3. Different tasks of electrical energy storage in grids [25].

2.4 Technical indicators of ESS

Technical indicators describe the performance of the ESS, therefore allow estimating its applicability for different real-world applications. They can be presented by the following pointers that are summarized in Table 1:

Power rating is a nominal power provided by the storage during operation;

Energy rating is an amount of energy that can be stored in the technology;

Discharge time is a duration of the discharge phase at nominal power;

Response time is a time that required for the ESS to respond to the changes in the operating conditions (switch on/off, switch between charge and discharge modes, decrease/increase of power generation);

Self-discharge rate is a ration of lost energy to the storage capacity during stand-by periods;

Suitable storage duration is a typical period of time during which the technology can hold the stored energy;

Efficiency presents the overall energy efficiency that is calculated as the ratio of energy exiting of the device over the energy entering into the device.

Lifetime is the time when the technology can operate without the replacement of principal components (power and storage units).

Table 1. Technical indicators of ESS [26,27].

ESS technology	Power rating (MW)	Energy rating (MWh)	Discharge time	Response time	Self-discharge (%/day)	Suitable storage duration	Efficiency	Lifetime (years)	Cycles
PHS	100-5000	1000+	24 h +	3 min	very small	h-month	70-85%	50	N/A
CAES	5-500	1000+	4 h	10 min	very small	h-month	45-70%	20-40	N/A
Flywheel	0.1-100	up to 5	s-min	ms-s	50%	s-min	85-98%	15-20	up to 100000
Conv. batteries (Li-ion)	0.001-50	up to 100	s-h	ms	0.1-0.3%	min-h	70-85%	7	5000
RFB	0.001-500	up to 1000	s-10 h	ms	very small	min-day	70-85%	20	up to 100000
SC	0.001-10	0.1	ms-h	ms	20-40%	s-h	85-98%	10-20	100000 +
SMES	0.001-10	0.1	ms-min	ms	10-15%	min-h	85-98%	15-20	100000 +
PtX (PtL/PtG)	0.1-10000	1000+	24 h +	min	very small	h-month	30-45%	30	N/A

Table 1 shows that energy storage technologies have some advantages and limitations that determine their technical suitability for specific services in power systems. As it was discussed before in Sec. 2.3 the storage applications can be mainly classified into two broad groups (energy and power services) that determine two opposite boundaries.

The first boundary presents energy-related services with the storage of large amounts of energy for an extended period (intermittent balancing, load leveling and time shifting). Such applications require storage technology with large energy capacity and low self-discharge; as a result, PHS and CAES are typically applied for such tasks. However, these technologies have a slow response and low energy efficiency, also requiring a specific location. All of these factors significantly limit their prevalence.

The second boundary presents power related services with the release of significant energy amounts in a short period (primary regulation, power quality). Such applications require storage with a high power rating and fast response time. Typically, Flywheels and supercapacitors are applied for the provision of such services. However, these technologies have colossal self-discharge and thus are not applicable for long storage durations.

Batteries fill the gap between these two boundaries having fast response time and extended discharge duration. Nevertheless, different batteries technologies have different intrinsic features (scalability, discharge duration, toxicity) that place them closer to the first or the second boundary. Among various batteries technologies, RFB has the broadest range for power and energy ratings due to their unique features (separate scaling of power and capacity and very low self-discharge) that will be discussed in the next section 2.4.

In addition to technical indicators, it is also essential to consider the economic aspects of the technologies by looking at the capital cost of power and energy units (Fig.4). As can be seen, PHS and CAES have a meager capital cost of energy, and thus, they can be used for the construction of cheap storage systems with large capacity. At the same time,

the increase of their power is rather expensive due to the high capital cost of power units. Hence, the economic analysis also supports the application of these technologies for bulk energy storage. On the contrary, the Flywheels and SC have an enormous capital cost of energy and thus are not feasible for the construction of large-capacity storage, while their capital cost of power is very low that reinforces their application for power-related services. Batteries are in the middle of these two extremes having a capital cost of power in the same order of magnitude as PHS and CAES, while their capital cost of energy is significantly lower than the price of SC and Flywheels. In addition, it should be noted that among the batteries technologies, the RFB demonstrates the lowest capital cost both for power and energy, hence, presenting the most economically attractive solution for storage with flexible power and energy ratings.

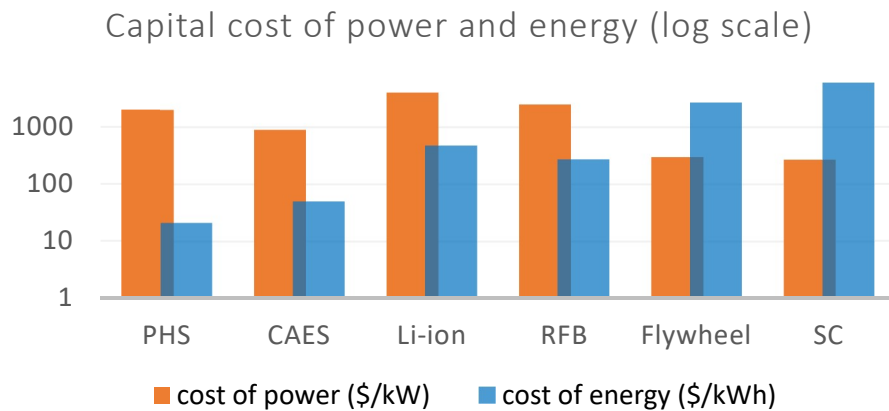


Fig. 4. The capital cost of energy and power units for different storage technologies [25,26].

Another important indicator is related to energy and power densities as they allow estimating the size of the storage facility for each technology. As can be seen from Fig. 5, PHS and CAES have deficient power and energy density (less than 10 W/L and 10 Wh/L), and thus, they require a lot of volume for construction that restricts their application (in addition to specific location requirements discussed above) only for stationary storage systems where sufficient space is available excluding for example urban applications. On the other hand, SC, SMES and Flywheels have large power density that makes them applicable for storage services where high power needs to be provided, e.g., fast-charging electric vehicles. Batteries have the widest range of energy and power densities, e.g., Li-ion has the highest numbers (2000 W/L and 400 Wh/L) while VRFB has significantly lower values (5 W/L and 40 Wh/L) that also determines different areas for their application.

Having lower energy and power density, VRFB technology is considered for stationary storage applications. In addition, the strong feature of VRFB related to fast response time, a wide range of operating state of charges, good tolerance to deep discharge make them suitable for multiple scenarios related to energy and power storage applications discussed above.

On the grid scale level, VRFB also can be compared with NaS batteries, which also have found application as large energy storage. Positive and negative electrodes of NaS batteries are composed of molten sulfur and molten sodium, respectively. Hence, for these materials to be presented in a liquid state, the battery must be kept at high temperatures (290 – 360 °C). During working cycles, NaS batteries are able to keep such temperatures

by themselves. A special feature of NaS batteries is the ability to operate in a pulse power mode when the battery can provide electricity in a power rate several times higher than the nominal power rating for periods ranging from seconds to hours. However, during standby, when there are no reactions generating heat, NaS batteries use electric heaters to keep their temperature over 290 °C that causes high self-discharge (20 %/ day) [28]. For these reasons NaS are not suitable for long term energy storage and are currently considered mainly for power applications. Another drawback of NaS batteries is that molten sodium is hazardous material for the environment as it is combustible if exposed to water.

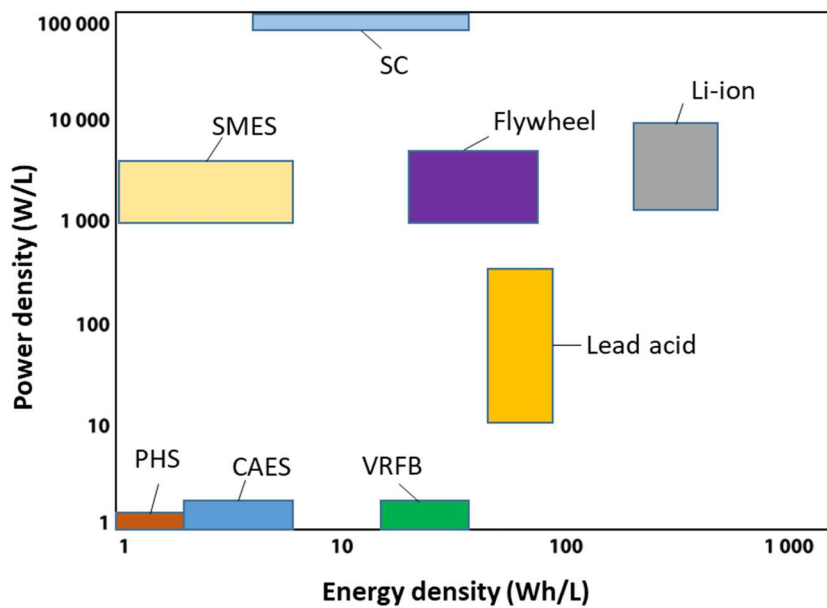


Fig. 5. Energy and power density of different storage technologies [22].

To understand the suitability of different technologies, they can be plotted in the simplified graph (Fig. 6) where the area of their application is shown by the rectangular boxes (the color of the boxes reflects energy efficiency), taking into account their intrinsic

features as response time, power and energy ratings, self-discharge, suitable discharge duration and capital cost of power and energy units.

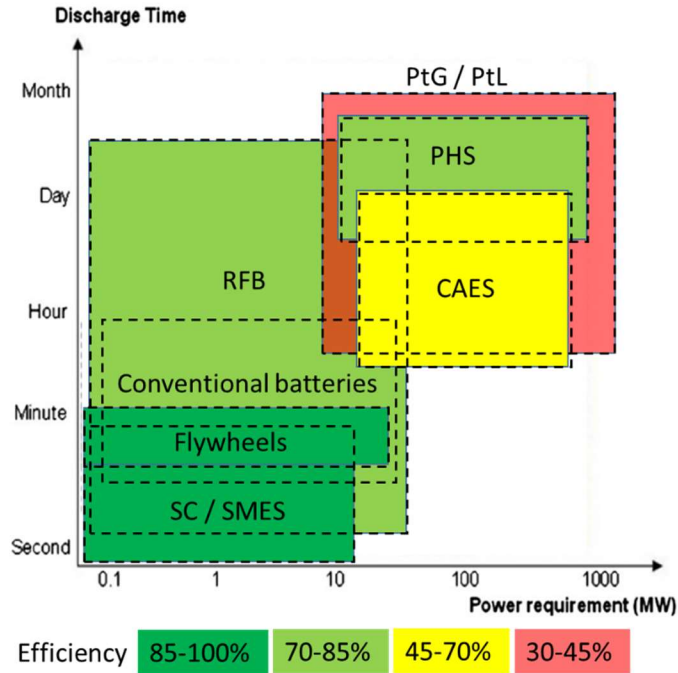


Fig. 6. Applicability of different stationary storage technologies [25].

As can be seen from Fig. 6, only RFB can be applied in the wide range of rated powers and discharge times, thus covering nearly all tasks of storage systems in the grid that was discussed in Sec. 2.3 and plotted in the same coordinates (Fig. 3). On the one hand, RFB has a wide range of energy ratings and goes close to PHS and CAES being suitable for bulk energy management services. On the other hand, RFB is close to Flywheels, SC and SMES due to fast response time and a broad range of power ratings, and thus, being suitable for power quality services. Hence, RFB technology has excellent potential for

development solutions “all in one” when the same storage unit can be used for multiple services simultaneously that gives more flexibility for power systems optimization.

2.5 Redox Flow Batteries

Conventional batteries are devices that store electrical energy in the form of chemical energy of reduction and oxidation reactions. A typical battery consists of three main elements (Fig. 7) [27]:

- positive electrode;
- negative electrode;
- electrolyte.

Materials of electrodes have different electrochemical potential that provokes spontaneous reduction (on the cathode) and oxidation (on the anode) reactions generating external electrical current when the circuit is closed for discharge cycle [23,27]. These electrochemical reactions are reversible, and thus, the battery can be recharged by applying an external voltage [23]. Fig. 7 shows the cathode, anode and current direction in charge and discharge cycles, where, due to the definition, the cathode and anode are the opposite in charge and discharge phase. Thus, further, we use a standard convention where the names of electrodes (positive and negative) are fixed for charge and discharge.

The battery performance mainly depends on three indicators:

- *depth of discharge (DOD)*, which shows the amount of used energy in respect to the storage capacity: full charged battery has 0% DOD, while the empty battery has 100% DOD (as a general rule coming from experimental evidence but

quantitatively depending on specific battery technology, high DOD cycling results in a shorter battery lifetime [27]);

- *discharge and charge rates*, which means how fast a battery can be discharged or charged, that is usually connected with energy to power ration and depends on the specific battery technology (e.g., Li-ion has a rigid charge rate as their power and capacity are bound, while for RFB this number is very flexible due to independence of power and energy ratings);
- battery operating *temperature*, the broader range of operating temperatures is better; however, usually, batteries work in a rather narrow range of temperatures, and thus, require additional auxiliary systems for their heating or cooling.

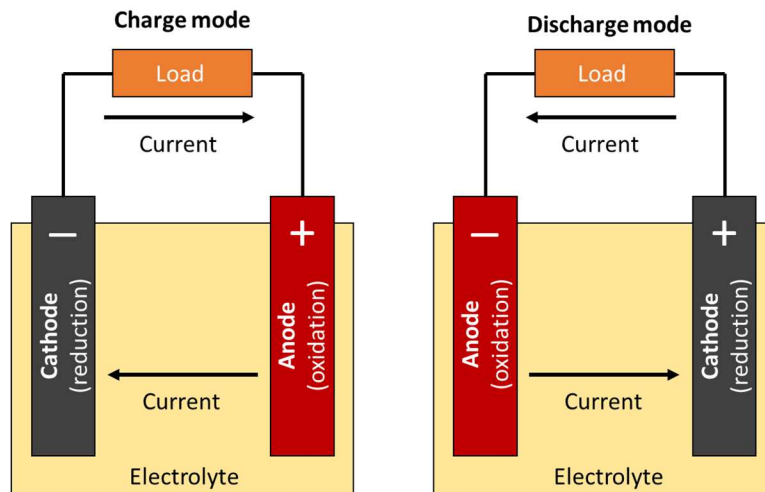


Fig. 7. Conventional battery operation during charge and discharge cycles

Redox Flow Batteries specific features

RFB works in the same principle as conventional batteries, but they have a different configuration. Typical RFB configuration consists of (Fig. 8):

- electrochemical cell (1);
- tanks with electrolytes (2);
- pumps (3).

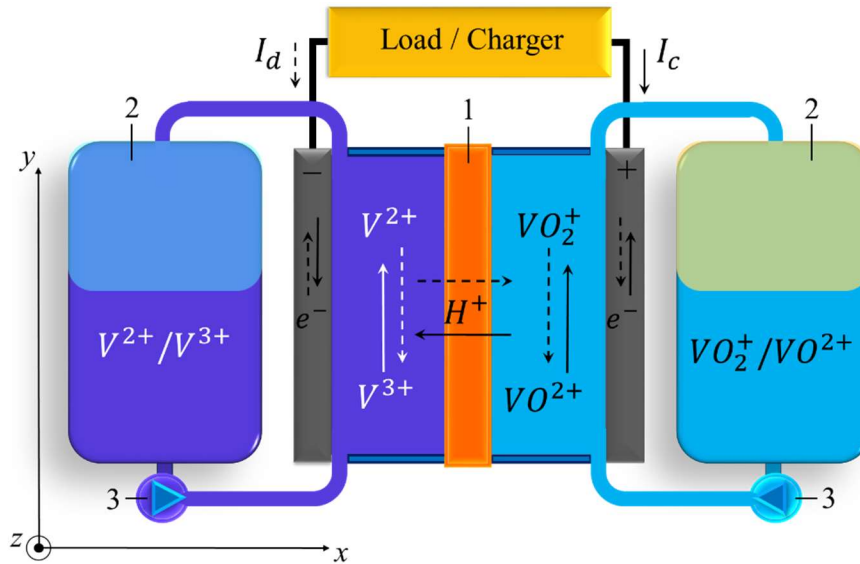


Fig. 8. Flow battery working scheme, namely Vanadium one.

The electrolyte (primarily stored in the tanks) is based on the two soluble couples (in Fig. 8, the solution is comprised of vanadium couples V^{2+}/V^{3+} and VO_2^+/VO^{2+}) and is pumped through the cell where electrochemical conversion takes. In charge mode, the electrolyte is reduced at the cathode and oxidized at the anode. Thus, the excess electrical energy from the grid is stored in the electrolyte chemical energy. During discharge, the above-mentioned electrochemical reactions go in the opposite direction, releasing electrons in the external circuit and producing additional electrical power. Depending on the

electroactive species used in the electrolyte, flow batteries can be classified into different categories [24,27]: Vanadium redox flow battery (VRFB), Zinc bromine battery (ZBB) and Polysulfide bromide battery (PSB).

Zinc-bromine battery (ZBB) uses a zinc-bromine solution as electrolytes for both tanks. During the charge phase, metallic zinc is disposed on the negative side, while elemental bromine is formed on the positive electrode [27]. The zinc and bromine ions migrate to the opposite electrolyte through the micro-porous separator to achieve charge equalization.

Polysulfide-bromide battery (PSB) uses sodium polysulfide and sodium bromine solutions stored in two separate tanks [24]. During the discharge, a solution of sodium disulfide (Na_2S_2) is pumped to the negative electrode where sodium disulfide becomes sodium polysulfide (Na_2S_4). At the same time, on the positive side, sodium tribromide (NaBr_3) transforms into sodium bromide (NaBr). The solutions in the cell are separated by a polymeric membrane that is permeable only for positive sodium ions, which transfer from one side to the other to equalize electric charge in the cell [23].

Vanadium Redox Flow Battery (VRFB) works with vanadium ions in both electrolytes as vanadium is available in 4 different valences, and thus, can be used in positive and negative sides: the positive electrolyte (catholyte) uses $\text{VO}^{2+}/\text{VO}_2^+$ redox couple and the negative electrolyte (anolyte) uses $\text{V}^{2+}/\text{V}^{3+}$ redox couple.

Energy efficiency of these RFB technologies lies in the range of 65 – 75%, in addition, all of them have rather fast response time (ms) and good tolerance to deep discharge. Speaking

about material selection, there are more expensive materials as vanadium, or more common and cheap as zinc and sodium. The solubility of active species used in ZBB and PSB is higher than the solubility of vanadium salts used in VRFB solutions resulting in two times higher energy density (80 Wh L^{-1}) than VRFB (40 Wh L^{-1}). Nevertheless, ZBB and PSB have some shortcomings in comparison to VRFB technology that limited their applications. For example, ZBB requires a specific recirculation system to handle a thick bromine oil flow to the bottom of the tank, while PSB has pure cycle life (approx. 2000 cycles) [27]. In addition, VRFB solution is non-toxic electroactive material, while ZBB and PSB have corrosive bromine solutions and bromine itself is a toxic material that requires special handling [29]. Moreover, using vanadium in both sides prevents cross-contamination and VRFB can work without capacity fade that is not the same for ZBB and PSB. All these factors made the VRFB technology more attractive for practical applications than the other RFB types. Therefore, further, we will focus on the investigation of VRFB systems.

RFB cells and stacks

A typical RFB cell (Fig. 9) is formed by two half-cells constituted of:

- current collector (that collects electrons providing them to the external circuit);
- graphite plate with channels (where electrolyte flows through);
- porous electrode (where redox reactions take place).

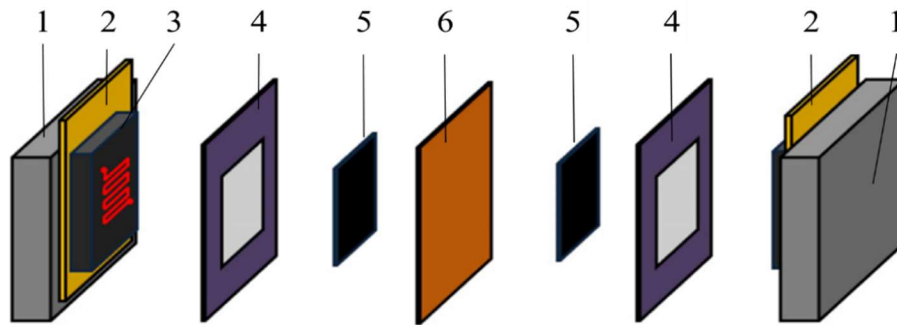


Fig. 9. Electrochemical cell construction [30]: end plate (1), current collector (2), graphite plate with channels (3), silicon gasket (4), porous electrode (5), membrane (6).

Depending on the ways how electrolyte passes through the cell, there are two different cells' concepts: flow-by and flow-through configurations (Fig. 10).

In the flow-through configuration, the only way for electrolytes to go through the cell is to percolate through a thick porous electrode.

In flow-by configuration, the electrolyte flows in the channels inside the graphite plate partially diffusing in the porous electrode, which contacts with channels.

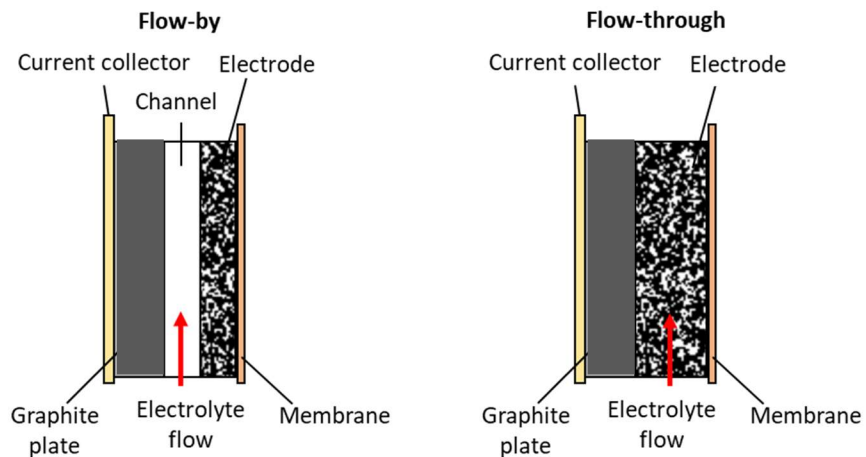


Fig. 10. Flow-by and flow-through configurations.

The two half-cells are separated by the membrane to prevent the mixing of positive and negative electrolytes (some active species ions can also transfer across the membrane (crossover), leading to side reactions, which result in self-discharge of the battery). The membrane is permeable for cations, cation exchange membrane (CEM), or anions, anion exchange membrane (AEM), that go through it and complete the electrochemical circuit to provide continuous occurrence of electrochemical reactions, which generate electricity.

Usually, the voltage of a single cell is about 1.5 V, thus to obtain higher voltages, the cells are joined together in the stack (Fig. 11). Typical fuel cell stack design with bipolar plates is used to connect one cell with the other.

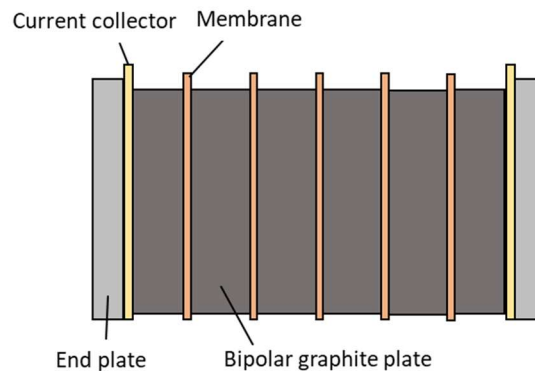


Fig. 11. VRFB cells stack.

Advantages of Redox Flow Batteries

The RFB configuration gives several benefits that determine a wide range of suitable tasks for the application of this technology. First, the topology of flow batteries allows separating the power rating and energy capacity: power depends on the number of cells in the stack, while capacity is connected with the volume of electrolytes in the tanks

(Fig. 12) [31]. As a result, both of these characteristics can be scaled up independently and RFB facilities can be easily scaled up to 1 GWh [32].

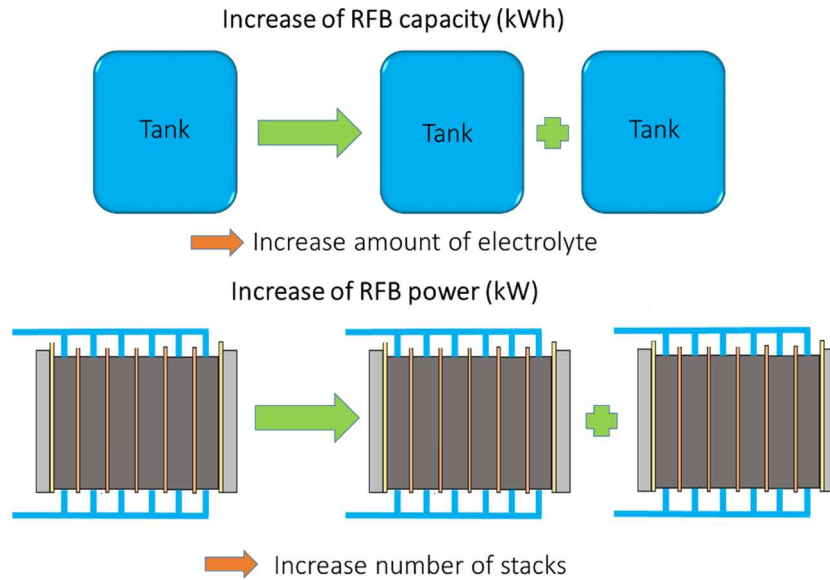


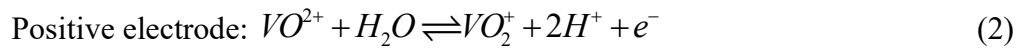
Fig. 12. Increase of RFB power and capacity.

In addition, such a modular design provides excellent flexibility for the design of individual storage systems according to the user's specifications. Moreover, storage of active species in the separated tanks results in very low self-discharge (related to reactions in the stacks occurring between electrolytes from different half-cells due to the transfer of active ions across the membrane), allowing to use RFB systems for storage of large amounts of energy and for long periods. Secondly, the active species contained in the liquid electrolyte can be fully used in charge-discharge operation without risk of damage. Thus RFB has a good tolerance to deep discharge that provides additional flexibility for a set of optimal operating constraints. Finally, the RFB has a rather long lifetime (20+ years,

several tens thousands of cycles) that makes this technology competitive in long-term operation as RFB can work during this time without replacement of main internal components.

2.6 Vanadium redox battery (VRFB)

As it has been mentioned before, Vanadium Redox Flow Battery (VRFB) is one of the most mature types of flow batteries that uses vanadium ions in both electrolytes as vanadium is available in 4 different valences, and thus, can be used in positive and negative sides: the positive electrolyte (catholyte) uses VO^{2+}/VO_2^+ redox couple with the redox potential of 1 V (at 298 K) and negative electrolyte (anolyte) uses V^{2+}/V^{3+} redox couple with the redox potential of -0.26 V (at 298 K). During the charge phase, V^{3+} ions become V^{2+} ions at the negative electrode, while VO^{2+} ions become VO_2^+ ions at the positive electrode [33,34]:



In the discharge phase, the reactions go in the opposite direction.

In addition, the solutions with different vanadium valences have different colors that also help to estimate the VRFB state of charge (Fig. 13). In the charge state, the anolyte contains mainly (about 90%) V^{2+} ions and thus has a violet color, while the catholyte contains mainly (about 90%) VO_2^+ ions and has a yellow color. In the discharge state, V^{2+} ions transform to V^{3+} ions, and the anolyte changes color to green, while the VO_2^+ transforms to VO^{2+} changing catholyte color from yellow to blue.

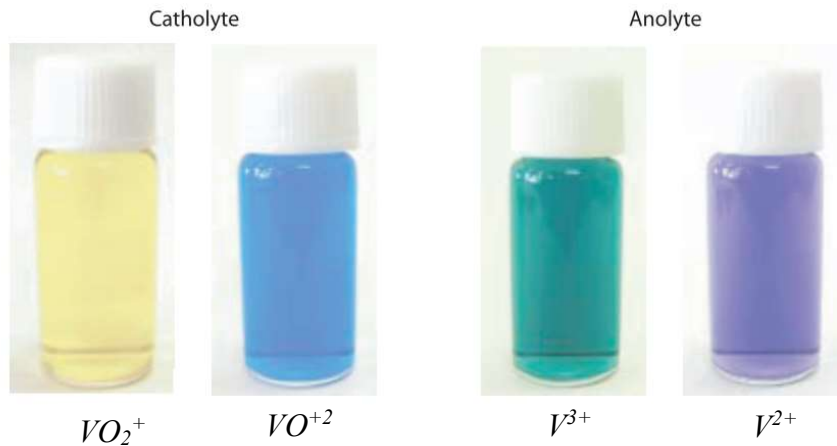


Fig. 13. Colors of vanadium electrolyte contained different vanadium ions [35].

Moreover, vanadium can be easily transferred from one valence to the other one as the reactions between these states are fully reversible. Hence, the degradation of the electrolyte caused by the vanadium ions crossing over the membrane can be mitigated by the special rebalancing procedures that allow recovering the initial state of electrolyte. Thus, VRFB works without capacity fade. (Fig. 14), while such an option is not available for conventional solid batteries.

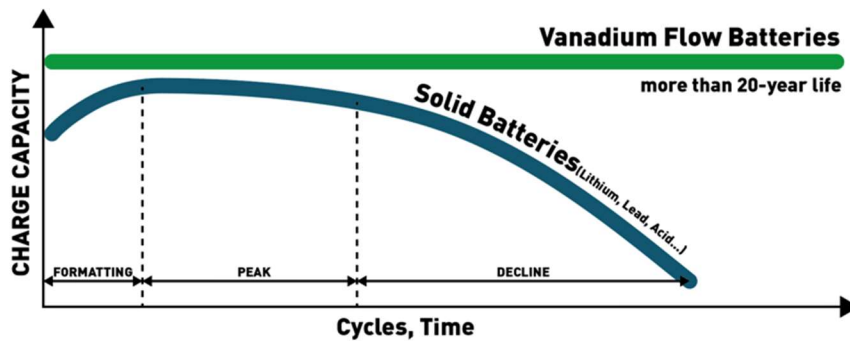


Fig. 14. Battery capacity in cycling operation [36].

The capital cost of VRFB per unit of energy stored is another strong point of this technology in comparison to other types of batteries. According to the latest data from IRENA provided in April 2020, the VRFB capital cost is 268 \$/kWh, which is nearly two times lower than the price of Li-ion batteries (466 \$/kWh) and NaS batteries (436 \$/kWh) [26].

Speaking about weak points of VRFB technology, one should highlight that due to a rather low solubility of vanadium compounds in the sulfuric solution, the VRFB has low energy density (ca. 25 Wh L⁻¹) that is ten times lower as compared to Li-ion batteries (ca. 400 Wh L⁻¹) [26]. As a result, VRFB has limited applicability for non-stationary electricity storage services. Another concern is related to precipitation of vanadium ions (presented by V₂O₅ compound) at the electrolyte temperatures higher than 50⁰C that restricts operating limits related to loading currents [26].

2.7 VRFB capital cost

The capital cost of VRFB is mainly formed by the cost of the ion-selective membrane (or separator) [37] and the cost of electrolyte. The membrane (or separator) cost presents nearly a third part of the total capital cost of the VRFB facility (Fig. 15). Besides, the price of vanadium plays a vital role in the capital cost of VRFB. Its share can be exceptionally high for large-scale systems (MWh), where it can present nearly half of the total battery cost [38].

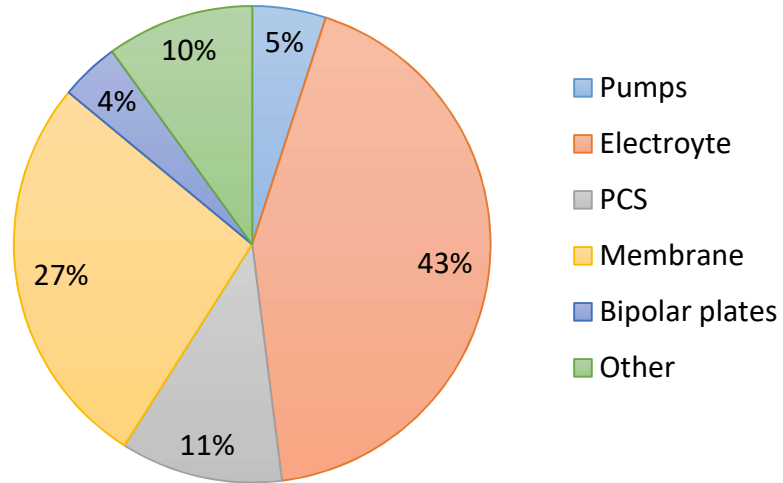


Fig. 15. VRFB capital cost structure for 1 MW/ 4 MWh system [38], PCS – power conditioning system (inverter, converter, battery management system).

Russia is among the leading countries for vanadium resources having $\frac{1}{4}$ of the global vanadium reserves (Fig. 16) [39]. Thus, with available vanadium resources, the VRFB technology can be very attractive for Russian manufacturers that could produce very competitive VRFB systems both for internal and European energy markets.

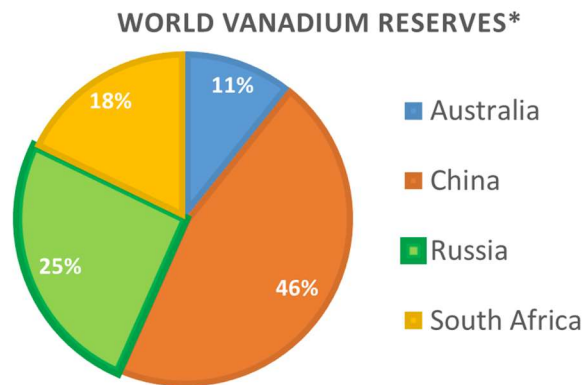


Fig. 16. Vanadium reserves in the world [39].

2.8 Conclusions

The share of renewable power generation is constantly increasing since the last decades. Due to their intermittent nature, renewable energy sources need to be balanced by energy storage systems to ensure stable energy supply. Electric energy storage systems with flexible energy and power ratings, long lifetime, and low operational costs are required. In the framework of these constraints, Vanadium Redox Flow Batteries (VRFB) are among the most promising solutions, which can tackle these challenges due to their strong features:

- modularity and independent scalability of capacity and power ratings;
- very low self-discharge;
- reversible capacity fade;
- long lifetime (more than 20 years/ 10000+ full cycles).

In addition, the VRFB can be interesting for Russian manufactures, as Russia has nearly 25% of the world's vanadium reserves and thus has direct access to vanadium resources.

Chapter 3. Mathematical modeling of VRFB systems

3.1 Introduction

Modeling of VRFB allows simulating the batteries with different sizes and at different operating conditions. A variety of models presents a set of powerful tools that target different applications (will be discussed further) related to the design, monitoring and control of VRFB systems. First, numerical simulations can provide a better understanding of the physical phenomena taking place in the battery that allows determining the proper constraints of the VRFB design and operating conditions. Also, modeling gives guidelines for researchers and engineers to avoid mistakes in the design and building of experimental facilities. Moreover, the numerical modeling approaches can be applied for techno-economic studies that could determine future trends for market penetration of VRFB systems.

In general, all modeling approaches can be divided into two large groups: macro-level approach and micro-level approach (Fig.17). The micro-level approaches, in turn, are presented by the material level models and continuum models. The material modeling provides a lot of details of internal processes in the system, considering the chemical and physical interactions between the molecules. This level is the most accurate but also the most complicated for simulations as it requires a lot of information about the internal properties of the system that, in many cases, are not available for measurements. In addition, it has high computational complexity requiring large CPU time (h-days) (Fig. 17).

This level of simulations is important for modeling of material properties and searching for new materials.

More simplified micro-level approaches are based on the continuum models within 2D or 3D modeling approaches (Fig.17). Even though this level of simulations is more simple than the previous one, it still has rather high computational complexity and requires significant CPU time (around several hours). The continuum models allow simulating internal processes on the cell level, investigating electrolyte distribution, mass transfer in the electrode, and gradients of temperatures and concentrations on the surfaces of internal components (membrane, electrodes, channels, bipolar plates). The approach is important for the determination of cell configuration and understanding the effect of the internal physical process.

The macro-level approaches are also presented by the zero-dimensional (or lumped-parameter) models and empirical models. The zero-dimensional and equivalent circuits models combine physical equations with some analytical or empirical correlations. Such approaches are less accurate as compared to the above-mentioned models, but they are fast (min-s) having small computational complexity. As a result, they allow simulating the dynamic behavior of the batteries on the system level, and thus, they are essential for practical application (e.g., they can be applied for the estimation of VRFB performance at real operating conditions for commercial-scale systems). Hence, such models allow determining the optimal battery usage protocols and can be used for real-time simulations in advanced control monitoring tools with feedback loops.

The lightest macro-level models are based on the empirical models [40] and applied for the market level simulations [41]. Such modeling approaches are the fastest among the all listed above as they provide the results almost immediately. Still, they have low accuracy, not considering the physical properties of internal components and specifications of the system configuration. As a result, they allow performing simulations of the batteries on the market level providing general trends and revealing their performance. They also help to determine the most prospective and economically efficient cases for the technology application.

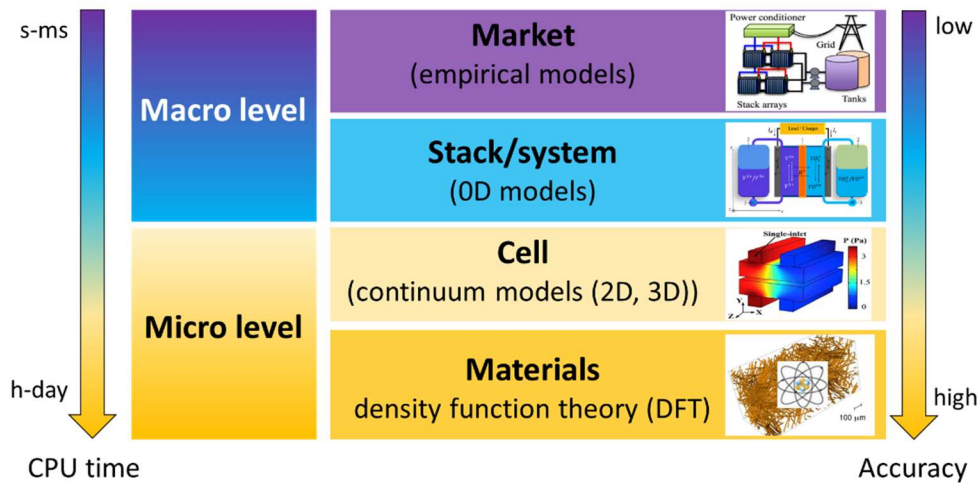


Fig. 17. Classification of modeling approaches, their applications and CPU time.

The idea of this work is to develop a multi-level simulation tool keeping the simplicity of lump parameter or zero-dimensional models. The developed approach should have a modest CPU time to simulate VRFB dynamic behavior in real-time while having the accuracy close to one of the continuum models. At the same time, the model should be able to simulate VRFB systems on different levels:

- cell level for an understanding of the internal process and their impact on the battery energy performance;
- system level for the development of advanced battery control strategies;
- market level for techno-economic assessments.

A detailed description of the developed model with key features is described in the next sections of the chapter.

3.2 Literature review

As was discussed in the previous chapter, VRFB stores electrical energy in the form of vanadium solutions in two separate external tanks. The solutions are pumped by two pumps through a stack comprised of cells where electrochemical conversion is taking place. The internal processes taking place in the cell during VRFB operation notably affect battery behavior. In general, intrinsic losses in the cell occur because of [42]:

- activation overvoltages (owing to the activation energy of electrochemical reactions);
- ohmic overvoltages (owing to the electric resistance of cell's components);
- concentration overvoltages (owing to mass transport limitations on the surface of the electrode);
- crossover (owing to the transfer of vanadium ions across the membrane).

The activation and ohmic overvoltages cause the deviation of battery voltage from the open-circuit voltage (OCV) in the whole range of operating state of charge (SOC) proportionally increasing to current density. The concentration overvoltages are affected

by the mass-transport processes on the electrode||electrolyte interface and depend on the battery SOC and loading current density. As a result, the concentration losses become pronounced at the end of charge and discharge processes when the concentration of active species becomes limited [43]. Moreover, the concentration overvoltages demonstrate significantly non-linear behavior, noticeably enlarging with the growth of current density and leading to a drastic drop in battery voltage. Such behavior can be addressed to the fact that the increase of current density requires more reactants for the current production. Hence a larger amount of reactants moves from electrolyte in the cell to the surface of the electrode to ensure higher currents. This, in turn, causes the growth of mass transport losses on the surface of the electrode that implies an increase of corresponding voltage drop. Hence, an accurate calculation of concentration overvoltages is essential for the proper prediction of the dynamic behavior of VRFB cells.

The crossover (transfer of vanadium ions across the membrane) [44] implies an increase of vanadium ions concentration in one half-cell and the corresponding decrease in the other half. Such an imbalance in electrolytes will consequently influence the battery capacity, which will become limited by the half-cell with the lowest vanadium concentration and volume [45], and as a result, the battery capacity loss will spring up. Arisen capacity decay will, in turn, limit the usable capacity in long-time operation and therefore needs to be detected and periodically corrected by electrolyte remixing [46]. Accordingly, to ensure a long operation of VRFB, it is compulsory to investigate the capacity decay mechanism caused by crossover and to develop reliable capacity restoration

methods [47]. Hence, modeling of crossover phenomenon is a very important issue in the development of sustainable VRFB facilities.

During the last decade, there were a number of works devoted to the modeling of VRFB on different levels. In general, they can be divided into two groups: equivalent circuit models and numerical models.

Equivalent circuit models simulate the cell by the electrical circuit with capacitors and resistors [48,49]. Recently, such an approach was adopted for real-time monitoring of capacity loss [50]. Modeling of VRFB with equivalent circuits has advantages and limitations. On the one hand, these models are able to capture the dynamics of VRFB, while they are simple and do not require significant computations, and as a result, they can be applied for control-oriented purposes. On the other hand, equivalent circuit models do not reflect the details of internal processes taking place in the cell. Therefore, the application of these models for simulation of real systems requires a lot of measured data and sophisticated optimization techniques [50], which could allow tuning the model in accordance with specifications of the certain system and its' operating conditions. Contrarily, numerical models are more comprehensive tools as they are based on the modeling of physical processes and hence, can be adapted to any system by changing only the coefficients related to the physical properties of cell components.

The first numerical dynamic 0-D model was developed by Li and Hikiyara in 2007 [51]. Then, Shah proposed a 2-D transient model in 2008 [52], which was based on the computational fluid dynamics approach (CFD). Further, this model was reduced to 0-D

unit cell model for control-oriented applications in 2011 [53]. Vynnycky simplified Shah's model with asymptotical methods suitable for large-scale VRFB stacks in 2011 [54]. Vynnycky's approach was transformed by Chen [55] into 1-D model that showed better results. You [56] simplified Shah's model transforming it into a steady-state model that was further extended into 3-D model by Ma [57], Xu [58], Oh [59] in 2012 - 2014. Recently, a non-uniform 3-D model was proposed by Wang [60] for the study of optimal electrode compression. However, all of these works did not model the crossover phenomenon, considering the membrane as an ideal separator conducting only the protons. The first model devoted to crossover modeling was developed by the group of Skyllas-Kazakos [44,61] in 2012. They proposed a 0-D dynamic model focusing on the diffusion-driven component for simulation of ions transport across the membrane. Further, they extended this approach into 1-D model [62]. Simulation of crossover, considering only diffusion-driven transport of ions, has advantages and limitations. On the one hand, it is rather simple, as the diffusion component can be easily calculated once the diffusion coefficients are known. On the other hand, such model is not able to predict the real effect of crossover. as electric field in the cell also provokes migration and convection of vanadium ions. These phenomena could have a significant effect on the total transport of ions in the cell [63]. The group of Kumbur developed first 2-D transient model [64], that considered all three transport mechanisms of the crossover (diffusion, migration and convection). This model demonstrated good results but was too sophisticated with many microscopic parameters. To simplify these conditions recently, Yang [65] developed a

single-domain model extending it on 3-D approach. Another 3-D model incorporated with crossover was proposed by Oh [66]. While these microscopic models can yield valuable information about internal processes and small-scale effects in the cell, they also require much more input microscopic parameters for each component. However, it is not feasible to incorporate this level of detail in the overall VRFB model or control-monitoring tools [53]. In addition, the development of an effective control system for electrolytes rebalancing requires a dynamic model that is able to predict VRFB behavior in real-time operation so that controller can be able to schedule such a rebalancing process [44]. However, the microscopic models require significant computational time, and therefore, are not suitable for this purpose. On the contrary, 0-D models are able to fulfill this requirement, having smaller time complexity. Moreover, they require significantly less computational power that allows to implement them on low-cost control hardware [67].

In this chapter, a control-oriented 0-D dynamic model able to accomplish precise simulation of crossover is presented. The model is based on a simple macroscopic approach for crossover simulation [61], elaborating it with an analytical solution for the crossover flux [63], which takes into account migration and convection components adopted from microscopic models. The considered method allows obtaining better accuracy (in comparison to existing solutions) for simulation of VRFB characteristics while it does not require significant computational power and time. Accordingly, the proposed model can be used for the development of advanced control strategies that could provide automated

battery management and ensure long-term operation of VRFB systems without significant loss of capacity.

3.3 VRFB mathematical model

The proposed mathematical model allows determining the voltage ($U_{ce}(t)$) of a single VRB cell [68] during charge and discharge processes, depending on the operating conditions: electric current ($I(t)$), electrolyte flow rate ($Q(t)$) and ambient temperature (T).

The following assumptions are made in deriving the mathematical model under consideration:

1. Isothermal conditions (cell and electrolyte temperatures remain constant at room temperature) [56];
2. The cells and tanks behave as continuously stirred tank reactors [61];
3. The concentration gradient in the pipes is very small and can be neglected;
4. In relation to the membrane:
 - absence of chemical reactions inside the membrane;
 - absence of i -th vanadium ion on the opposite side of the membrane due to rapid chemical reactions;
 - uniform distribution of the current density;
 - convection in the membrane is mainly determined by the water transfer, which is forced by electro-osmotic drag [63,69];
 - water velocity in the membrane is uniform and can be estimated with the following expression [63,69]:

$$u^m = u_w^m = \frac{\xi j^m}{\lambda c_f F} \quad (3)$$

5. Constant cell electric resistance [61];
6. The movement of electrolyte in the hydraulic circuit (tanks, pipes and half-cells) are mainly forced by convection;
7. Electrolyte velocity in the half-cell and in the tank is uniform and directed along the electrode longitude;
8. The flux of electrolyte in each domain is one dimensional and directed in a longitude coordinate;
9. Constant electrolyte flow rate.

In the presence of the electrical current, the internal losses cause the change of $U_{ce}(t)$ relative to the cell equilibrium potential ($U_{eq}(t)$). Such losses are constituted by activation ($\eta_{act}(t)$), ohmic ($\eta_{ohm}(t)$) and concentration overvoltages ($\eta_{con}(t)$) discussed in Sec.3.2.

The cell potential $U_{ce}(t)$ is calculated with the application of Eq.(4) where “+” and “-” are related to charge and discharge operation modes, respectively [42]:

$$U_{ce}(t) = U_{eq}(t) \pm (\eta_{act}(t) + \eta_{ohm}(t) + \eta_{con}(t)) \quad (4)$$

The equilibrium conditions take place in absence of the electric current in the cell. The $U_{eq}(t)$ is described by the Nernst equation with application of formal potential U_0^* [62]:

$$U_{eq}(t) = U_0^* + \frac{RT}{F} \ln \left\{ \left(\frac{c_2^{ce}(t)}{c_3^{ce}(t)} \right) \left(\frac{c_5^{ce}(t)}{c_4^{ce}(t)} \right) \right\} \quad (5)$$

where:

- R = gas constant [$\text{J K}^{-1}\text{mol}^{-1}$];
- T = ambient temperature [K];
- F = Faraday's constant [C mol^{-1}];
- U_0^* = formal potential [V];
- c_i^{hc} = concentration of the i -th vanadium ion in the half-cell [mol m^{-3}].

The formal potential (U_0^*) presents a joint effect of standard potential, proton concentrations and ion activity coefficients. It corresponds to the OCV at 50% SOC (SOC is the battery state of charge that will be discussed in Sec 3.4) [44,62], and thus, can be obtained from experiments. The measurements in our experiments showed that $U_0^* = 1.38$ V, which is slightly smaller than the reported value of 1.4 V [44]. This difference is likely due to different electrolyte compositions: 1 M vanadium in 2.5 M sulfuric acid (in our case) versus 2 M vanadium in 5 M sulfuric acid in [44].

The mass balance of vanadium ions in the respective half-cell and in the tank is expressed by the following systems of ordinary differential equations:

for V^{2+} ion:

$$\begin{cases} V_{ce} \frac{dc_2^{ce}(t)}{dt} = Q(c_2^{tk}(t) - c_2^{ce}(t)) - (J_2(t) + J_4(t) + 2J_5(t))A_m + S_2V_{ed} \\ \frac{dc_2^{tk}(t)}{dt}V_{tk} = Q(c_2^{ce}(t) - c_2^{tk}(t)) \end{cases} \quad (6)$$

for V^{3+} ion:

$$\begin{cases} V_{ce} \frac{dc_3^{ce}(t)}{dt} = Q(c_3^{tk}(t) - c_3^{ce}(t)) - (J_3(t) - 2J_4(t) - 3J_5(t))A_m + S_3V_{ed} \\ V_{tk} \frac{dc_3^{tk}(t)}{dt} = Q(c_3^{ce}(t) - c_3^{tk}(t)) \end{cases} \quad (7)$$

for VO^{2+} ion:

$$\begin{cases} V_{ce} \frac{dc_4^{ce}(t)}{dt} = Q(c_4^{tk}(t) - c_4^{ce}(t)) - (J_4(t) - 3J_2(t) - 2J_3(t))A_m + S_4V_{ed} \\ V_{tk} \frac{dc_4^{tk}(t)}{dt} = Q(c_4^{ce}(t) - c_4^{tk}(t)) \end{cases} \quad (8)$$

for VO_2^+ ion:

$$\begin{cases} V_{ce} \frac{dc_5^{ce}(t)}{dt} = Q(c_5^{tk}(t) - c_5^{ce}(t)) - (J_5(t) + 2J_2(t) + J_3(t))A_m + S_5V_{ed} \\ V_{tk} \frac{dc_5^{tk}(t)}{dt} = Q(c_5^{ce}(t) - c_5^{tk}(t)) \end{cases} \quad (9)$$

where:

- c_i^{tk} = concentration of the i-th vanadium ion in the tank [mol m^{-3}];
- c_i^{ce} = concentration of the i-th vanadium ion in the half-cell [mol m^{-3}];
- Q = electrolyte flowrate [$\text{m}^3 \text{s}^{-1}$];
- V_{tk} = volume of the tank [m^3];
- V_{ce} = volume of the half-cell [m^3];
- V_{ed} = volume of the electrode [m^3];
- S_i = source term [$\text{mol m}^{-3} \text{s}^{-1}$] (see Table 2);
- A_m = area of membrane surface [m^2];
- J_i = molar flux of i-th ion across the membrane [$\text{mol m}^{-2} \text{s}^{-1}$].

The systems of mass transfer equations can be joint together and written in more compact matrix form:

$$\frac{d\vec{x}}{dt} = \mathbf{Q}\mathbf{A}\vec{x} + \mathbf{J}\vec{x} + I\vec{S}, \quad (10)$$

where

$$\vec{x} = (x_1, x_2, x_3, x_4, x_5, x_6, x_7, x_8)^T = (c_2^{tk}, c_3^{tk}, c_4^{tk}, c_5^{tk}, c_2^{ce}, c_3^{ce}, c_4^{ce}, c_5^{ce})^T, \quad (11)$$

$$\vec{S} = \left(0, 0, 0, 0, \frac{1}{FV_{cell}}, -\frac{1}{FV_{cell}}, -\frac{1}{FV_{cell}}, \frac{1}{FV_{cell}} \right)^T, \quad (12)$$

$$\mathbf{A} = \begin{pmatrix} -\theta & 0 & 0 & 0 & \theta & 0 & 0 & 0 \\ 0 & -\theta & 0 & 0 & 0 & \theta & 0 & 0 \\ 0 & 0 & -\theta & 0 & 0 & 0 & \theta & 0 \\ 0 & 0 & 0 & -\theta & 0 & 0 & 0 & \theta \\ \gamma & 0 & 0 & 0 & -\gamma & 0 & 0 & 0 \\ 0 & \gamma & 0 & 0 & 0 & -\gamma & 0 & 0 \\ 0 & 0 & \gamma & 0 & 0 & 0 & -\gamma & 0 \\ 0 & 0 & 0 & \gamma & 0 & 0 & 0 & -\gamma \end{pmatrix} \quad (13)$$

$$\mathbf{J} = \begin{pmatrix} 0 & 0 & 0 & 0 & 0 & 0 & 0 & 0 \\ 0 & 0 & 0 & 0 & 0 & 0 & 0 & 0 \\ 0 & 0 & 0 & 0 & 0 & 0 & 0 & 0 \\ 0 & 0 & 0 & 0 & 0 & 0 & 0 & 0 \\ 0 & 0 & 0 & 0 & -J_2 & 0 & -J_4 & -2J_5 \\ 0 & 0 & 0 & 0 & 0 & -J_3 & 2J_4 & 3J_5 \\ 0 & 0 & 0 & 0 & 3J_2 & 2J_3 & -J_4 & 0 \\ 0 & 0 & 0 & 0 & -2J_2 & -J_3 & 0 & -J_5 \end{pmatrix} \quad (14)$$

Here, $\mathbf{A} \in \mathbb{R}^{8 \times 8}$ is the matrix related to convection between the cell and the tank,

$\mathbf{J} \in \mathbb{R}^{8 \times 8}$ is the matrix related to crossover in the cell, $\theta = 1 / V_{tk}$ and $\gamma = 1 / V_{ce}$.

Taking into account non-linear concentration profiles of vanadium ions in the membrane, the molar flux J_i is calculated analytically and presented in the form [63]:

$$J_i = \frac{P_i^m c_i^{ce}}{d_m} \frac{\chi_i}{1 - \exp(-\chi_i)} \quad (\text{when migration and convection } \uparrow\uparrow \text{ diffusion}) \quad (15)$$

$$J_i = \frac{P_i^m c_i^{ce}}{d_m} \frac{\chi_i}{\exp(\chi_i) - 1} \quad (\text{when migration and convection } \uparrow\downarrow \text{ diffusion}) \quad (16)$$

where χ_i is a dimensionless parameter presenting migration and convection:

$$\chi_i = \left(\frac{z_i F}{\sigma^m RT} + \frac{\xi K_i}{P_i^m F \lambda c_f} \right) d_m j^m \quad (17)$$

- P_i^m = permeability coefficient of the i-th ion [$\text{m}^2 \text{s}^{-1}$];
- K_i = partitioning coefficient of the i-th ion [-];
- z_i = valence of the i-th ion [-];
- c_i^{hc} = concentration of the i-th vanadium ion in the half-cell [mol m^{-3}];
- d_m = thickness of the membrane [m];
- σ^m = conductivity of the membrane [S m^{-1}];
- j^m = current density [A m^{-2}];
- ξ = water electro-osmotic coefficient [-];
- λ = water content coefficient [-];
- c_f = concentration of fixed sites in the membrane [mol m^{-3}].

In discharge mode, the current (and therefore, migration and convection) is directed from the negative to the positive half-cell (Fig. 18). Hence, in this case, the current has the same direction as the diffusion flux of V^{2+} and V^{3+} ions and their total flux is described by Eq.(15), the diffusion flux of VO_2^+ and VO^{2+} ions has the opposite direction and, accordingly, is described by Eq.(16), while in the charge mode, it is the other way round (Fig. 18).

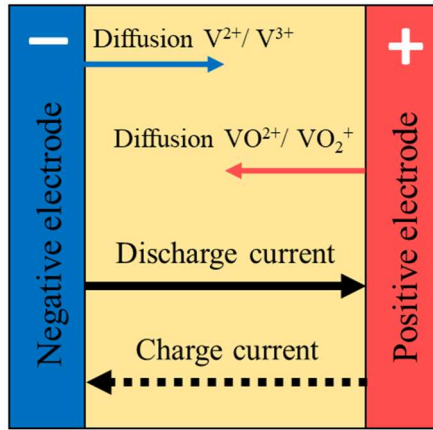


Fig. 18. Direction of current and diffusion flux in charge and discharge modes.

In parameter χ_i we also took into account that vanadium ion concentration in the membrane can be connected with its' concentration in the adjacent electrolyte through dimensionless partitioning coefficient K_i [69–71]. In addition, we considered the membrane in a liquid-equilibrated state that corresponds to real conditions, as the membrane is in constant contact with liquid electrolytes on both sides [53], and in this case water content coefficient $\lambda = 22$ [72].

Table 2. The source term for mass transport equation [64,73,74].

Type of ion	The source term S_i	
	Charge	Discharge
V^{2+}	$\frac{I}{V_{ed}F}$	$-\frac{I}{V_{ed}F}$
V^{3+}	$-\frac{I}{V_{ed}F}$	$\frac{I}{V_{ed}F}$
VO^{2+}	$-\frac{I}{V_{ed}F}$	$\frac{I}{V_{ed}F}$
VO_2^+	$\frac{I}{V_{ed}F}$	$-\frac{I}{V_{ed}F}$

Due to difficulties related to the evaluation of the activation overvoltages, for the sake of simplicity, they are included in the Ohm's law together with the ohmic losses by introducing the equivalent electric resistance of the cell [62]:

$$\eta_{act}(t) + \eta_{ohm}(t) = R_{ce}I(t) \quad (18)$$

The concentration overvoltages η_{con} are expressed as [43]:

$$\eta_{con}(t) = \frac{RT}{F} \ln \left(1 - \frac{I}{I_{lim}} \right) \quad (19)$$

where I_{lim} is a limiting current:

$$I_{lim} = k_m A_{ed} F C_{react}^{ce} \quad (20)$$

where:

- A_{ed} = area of electrode surface [m^2];
- k_m = mass transfer coefficient [$m \text{ s}^{-1}$];

- c_{react}^{hc} = reactant concentration on each electrode during charge and discharge processes [mol m^{-3}] (Table 3);
- I = electrical current [A].

Table 3. Reactant concentration on the electrodes during charge and discharge.

c_{react}^{ce} , mol m^{-3}	Charge	Discharge
Positive electrode	c_4^{ce}	c_5^{ce}
Negative electrode	c_3^{ce}	c_2^{ce}

The total concentration overvoltages $\eta_{con,tot}$ are presented as the sum of the overvoltages on the positive η_{con}^{pe} and negative η_{con}^{ne} electrodes, respectively:

$$\eta_{con,tot} = \left| \eta_{con}^{pe} \right| + \left| \eta_{con}^{ne} \right| \quad (21)$$

Mass transfer coefficient k_m considers the diffusion and convection of the reacting species on the electrode||electrolyte interface and can be approximated by Eq.(22) [75]:

$$k_m = \alpha u^\beta \quad (22)$$

where α and β are the empirical constants; u = electrolyte velocity in the channels of the electrode ($u=Q/A_{chn}$) [26].

It is worth noting that the empirical constants (α and β) are different for different cells ($1.3 \times 10^{-5} < \alpha < 1.9 \times 10^{-2}$, $0.39 < \beta < 1.18$ [56,75–77]) as far as the cell configuration influences on the convection while electrode material affects the diffusion on the surface of the electrode.

3.4 Energy performance indicators

The energy performances of a single VRB cell are evaluated by the state of charge ($SOC(t)$), roundtrip coulombic efficiency (CE), roundtrip voltage efficiency (VE) and roundtrip energy efficiency (EE) [78]. Here “roundtrip” means that the values are estimated for the charge-discharge cycle, and thus, show the losses in a cycle.

In particular, $SOC(t)$ is defined as the ratio between the instantaneous value of the stored energy in the tanks and the maximum allowable value of the stored energy in the tanks:

$$SOC(t) \equiv E_s(t) / E_{s,max} \quad (23)$$

The maximum value of SOC is equal to one at the end of the charging process and at the beginning of the discharge process, whereas the minimum value of SOC is equal to zero at the beginning of the charging process and at the end of the discharge process.

The maximum value of energy that could be stored in the battery is proportional to the sum of concentrations of the electrochemical couples, while the instant value of the energy is proportional to the concentration of the active species (V^{2+} and VO_2^+ ions):

$$SOC(t) = \frac{c_2(t)}{c_2(t) + c_3(t)} = \frac{c_5(t)}{c_5(t) + c_4(t)} \quad (24)$$

In reality, the crossover shortens the SOC causing the disbalance between the positive and negative electrolytes. Therefore, the SOC should be estimated by the minimum value of the above-mentioned ratios:

$$SOC(t) = \min \left(\frac{c_2(t)}{(c_2(t) + c_3(t))}, \frac{c_5(t)}{c_5(t) + c_4(t)} \right) \quad (25)$$

CE is defined as the ratio between the charge (in Coulombs) passed in discharge and charge processes, respectively. Due to the fact, the charge-discharge cycles are considered under operation at the constant current densities, the CE is evaluated as:

$$CE = \tau_d / \tau_c \quad (26)$$

where:

τ_c = duration of the charging process;

τ_d = duration of the discharge process.

VE is defined as the ratio between the averaged cell's voltage in discharge and charge processes, respectively:

$$VE = \langle U_{ce,d} \rangle / \langle U_{ce,c} \rangle \quad (27)$$

where:

$\langle U_{ce,d} \rangle$ = cell voltage averaged over the duration of the discharge process;

$\langle U_{ce,c} \rangle$ = cell voltage averaged over the duration of the charging process.

EE is defined as the ratio between the overall electric energy provided by the cell to the user at the end of a discharging process (E_{dis}) and the overall electric energy provided by the electric generator to the cell at the end of the charging process (E_{ch}), considering a single charging-discharging cycle. Taking into account Eq. (22) and (23), EE can be evaluated as:

$$EE = CE \cdot VE \quad (28)$$

3.5 Initial conditions

The initial values of vanadium ions concentrations in the tank and in the half-cell were obtained from the initial value of battery state of charge (SOC_0):

$$\begin{cases} c_2^{tk}(0) = c_2^{hc}(0) = c_{van,init} SOC_{init} \\ c_3^{tk}(0) = c_3^{hc}(0) = c_{van,init} (1 - SOC_{init}) \\ c_4^{tk}(0) = c_4^{hc}(0) = c_{van,init} (1 - SOC_{init}) \\ c_5^{tk}(0) = c_5^{hc}(0) = c_{van,init} SOC_{init} \end{cases} \quad (29)$$

They also can be written in the vector form:

$$\vec{x}(0) = (SOC_0, 1 - SOC_0, 1 - SOC_0, SOC_0, SOC_0, 1 - SOC_0, 1 - SOC_0, SOC_0)^T \quad (30)$$

The initial SOC was obtained from the OCV, which was determined at the beginning of each measurement (Table 4).

Table 4. Initial OCV for charge-discharge curves measured in experiments

Current density, [mA cm ⁻²]	OCV (charge), [V]	OCV (discharge), [V]
40	1.230	1.522
60	1.233	1.518
80	1.237	1.510
100	1.240	1.507

3.6 Numerical details

Numerical model is implemented in MATLAB with the application of Euler method for numerical solution of ODE systems. The battery voltage is calculated in the time loop

with time step 0.5 s. In addition, verification of the numerical approach was made and the calculations with smaller time steps (0.25 s, 0.1 s and 0.05 s) demonstrated the same results.

On the first step, the initial values of vanadium concentrations were determined from initial SOC (Eq.(29)). After that, the corresponding battery voltage was determined and calculations continued till the battery voltage did not reach the cutoff threshold (0.8 V for discharge and 1.6 V for charge). The calculations were made using the laptop with 2.4 GHz Intel Core i5 processor and 8GB RAM. The simulations demonstrated modest computational time, and the averaged time required for simulation of a charge or a discharge curve was around several seconds, while the time of corresponding experimental measurements was around several hours.

The values of the input parameters used in the proposed mathematical model are reported in Table 5.

Table 5. Specification of experimental setup and parameters in the simulation

Characteristics	Unit	Value
Faraday's constant, F	C mol ⁻¹	96485
Gas constant, R	J K ⁻¹ mol ⁻¹	8.31
Formal potential*, U_0^*	V	1.38
Initial concentration of vanadium ions, $C_{van,init}$	mol m ⁻³	1000
Tank volume, V_{tk}	m ³	2.0·10 ⁻⁵
Operating temperature, T	K	298

Membrane surface area, A_m	m^2	$5.0 \cdot 10^{-4}$
Electrode surface area, A_{ed}	m^2	$5.0 \cdot 10^{-4}$
Cross-section area of electrode channels, A_{ch}	m^2	$2.0 \cdot 10^{-6}$
Half-cell volume, V_{hc}	m^3	$2.6 \cdot 10^{-7}$
Mass transfer coefficient*, k_m	m s^{-1}	$2.0 \cdot 10^{-4} u^{0.7}$
Membrane thickness, d_m	m	$1.25 \cdot 10^{-4}$
Membrane conductivity*, σ^m	S m^{-1}	6.0
Concentration of fixed sites, c_f [56]	mol m^{-3}	1200
Water electro-osmotic coefficient, ξ	-	3.0
Water content coefficient, λ [72]	-	22.0
Permeability coefficients [79]		
P_2	$\text{m}^2 \text{s}^{-1}$	$9.4 \cdot 10^{-12}$
P_3	$\text{m}^2 \text{s}^{-1}$	$1.4 \cdot 10^{-11}$
P_4	$\text{m}^2 \text{s}^{-1}$	$4.4 \cdot 10^{-12}$
P_5	$\text{m}^2 \text{s}^{-1}$	$2.4 \cdot 10^{-12}$
Partition coefficients [70]		
K_2	-	1.15
K_3	-	0.76
K_4	-	0.6
K_5	-	0.77

Electrolyte flowrates

Q_1	$\text{m}^3 \text{s}^{-1}$	$0.7 \cdot 10^{-7}$
Q_2	$\text{m}^3 \text{s}^{-1}$	$2.5 \cdot 10^{-7}$
Q_3	$\text{m}^3 \text{s}^{-1}$	$8.6 \cdot 10^{-7}$

Current densities

j_1	mA cm^{-2}	40
j_2	mA cm^{-2}	60
j_3	mA cm^{-2}	80
j_4	mA cm^{-2}	100

3.7 Experimental measurements and model validation

The experimental VRB cell, which main characteristics are summarized in Table 5, was based on an Arbin fuel cell hardware having a 5 cm^2 active area (the photo of the experimental setup is shown on Fig. 19a and the assembly scheme is shown in Fig. 19b). The cell had a symmetric configuration. Two layers of Toray TGP-H-090 non-wetproofed carbon paper covered with Ketjenblack EC-600 JD carbon black and Nafion as a binder prepared according to the previously described procedure [78] were used as electrodes on both sides of the cell. Nafion 115 was used as a membrane material. The membrane was pretreated by sequential boiling in distilled water (1 h), aqueous H_2O_2 (3 wt. %, 1.5 h), distilled water (1 h), aqueous H_2SO_4 (0.5 M, 1.5 h), and distilled water (1 h).

Equal amounts (20 mL) of aqueous solutions containing 1.0 M of vanadium salt in 2.5 M sulfuric acid were used as the negative and the positive electrolyte, respectively. The

electrolytes were stored inside two separate sealed reservoirs under a high-purity argon atmosphere and were pumped through the cell by means of two peristaltic pumps. All the electrochemical measurements have been performed using an Autolab PGSTAT 302N potentiostat with Autolab Booster 20A for high current measurements. The experiments were carried out in order to measure the charge-discharge and polarization curves. All measurements were conducted at room temperature (298 K).

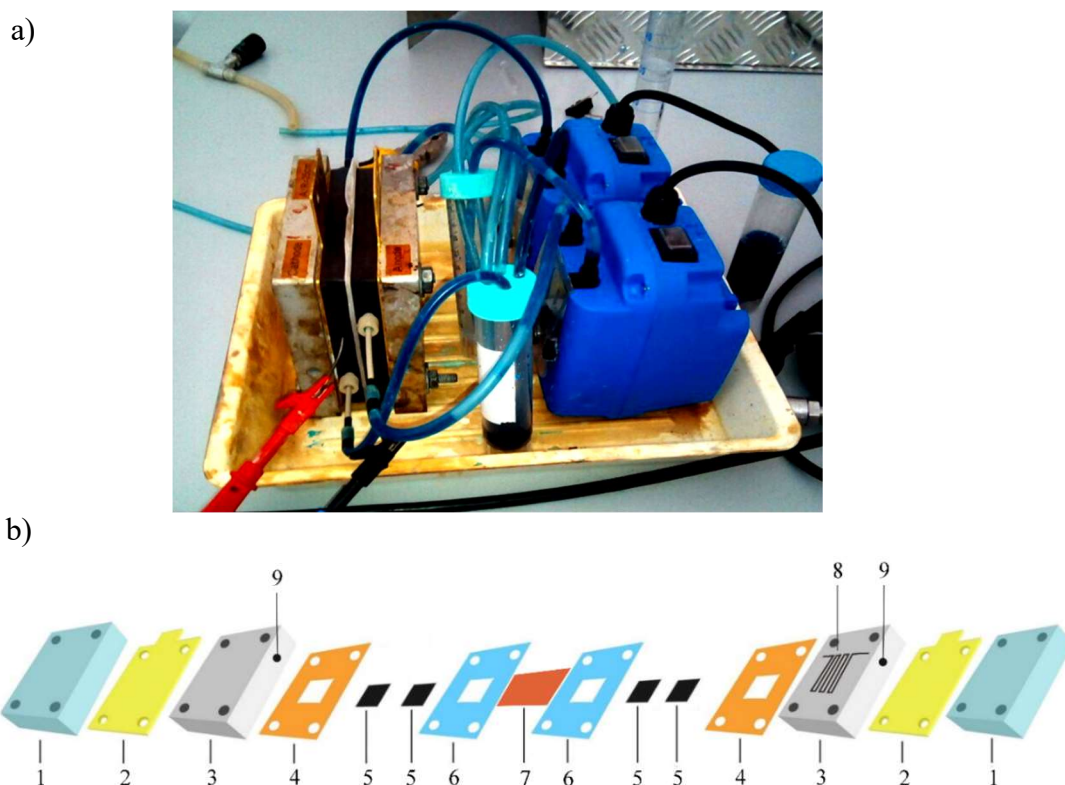


Fig. 19. Experimental setup: a) photo of the test bench (MSU lab); b) flow cell assembly scheme. The cell consisted of fixing plates (1), gold plated current collector plates (2), graphite polar plates (3) with double serpentine flow channels (8) having inlet-

outlet openings located on the side faces of the plates (9), 25 μm thick PEEK gaskets (4), electrodes (5), 0.5 mm thick silicone gaskets (6) and a membrane (7).

During charge-discharge curve measurements the cell was charged up to 1.6 V and discharged up to 0.8 V at fixed current densities of 20, 40, 60, 80 and 100 mA cm^{-2} . At the same time, the electrolyte flowrate was fixed and was equal to Q_3 . At least 3 charge-discharge cycles at each current density were performed.

Measurements of polarization curves were carried out from the initial $\text{SOC} = 0.5$ for discharge mode. In fact, the SOC decreased with the growth of the current for each value of the flowrate [80]. The decrease of SOC was due to the limited amount of electrolyte in the tanks and it could be reduced by increasing the volume of electrolyte in the tanks. The polarization curves were registered by a gradual increase of current density at a rate of 2 $\text{mA cm}^{-2} \text{ s}^{-1}$ with a step of 2 mA cm^{-2} and were measured for three different flowrates: Q_1 ; Q_2 and Q_3 .

3.8 Results and discussion

First, the experimental polarization curves (Fig. 20) were used in order to estimate the influence of internal losses on the cell voltage. The linear behavior of the curves in the low current density region indicates that activation overvoltages are small. This may be due to the high electrochemical surface area of carbon paper electrodes covered with an additional layer of carbon black, as described previously [78]. Thus, activation losses can be taken into account together with ohmic losses by using equivalent resistance [62]. The equivalent resistance of the cell was estimated from the linear part of the curves and was

equal to $0.65 \Omega \text{ cm}^2$, which is close to the value reported by Aaron [68]. This value was further used for the calculation of joint activation and ohmic overvoltages in charge and discharge cycles.

On the next step, the influence of concentration losses was determined. The concentration overvoltages can be found when the limiting current (Eq. (20)) is known, which can be obtained from the measurements of polarization curves. However, the value of limiting current by itself is a “black box” and is not able to yield the understanding of mass transport processes taking place in the electrode region. Hence, to make our model more comprehensive, we also determined the mass transfer coefficient, which is valid for our experimental setup. In order to do that, the polarization curves for three different flow rates were measured and the corresponding limiting current was obtained (a similar approach was proposed in [81]). Further, the mass transfer coefficient was determined by varying α and β coefficients in the way that calculated limiting currents were close to the measured one. The results showed that the values of $\alpha=2.0$ and $\beta=0.7$ can ensure the best agreement with experimental data (Fig. 18). The obtained values for α and β are different from those reported previously in the literature ($\alpha=1.6$ and $\beta=0.4$) [76], which in our case could provide a reasonable fit only for the high flow rate and significantly overestimate the limiting current for the lower flow rates (Fig. 20). The difference of α and β observed in our case might be attributed to the additional coverage of electrodes with carbon black that could significantly change the respect of convection and diffusion on the surface of the electrode.

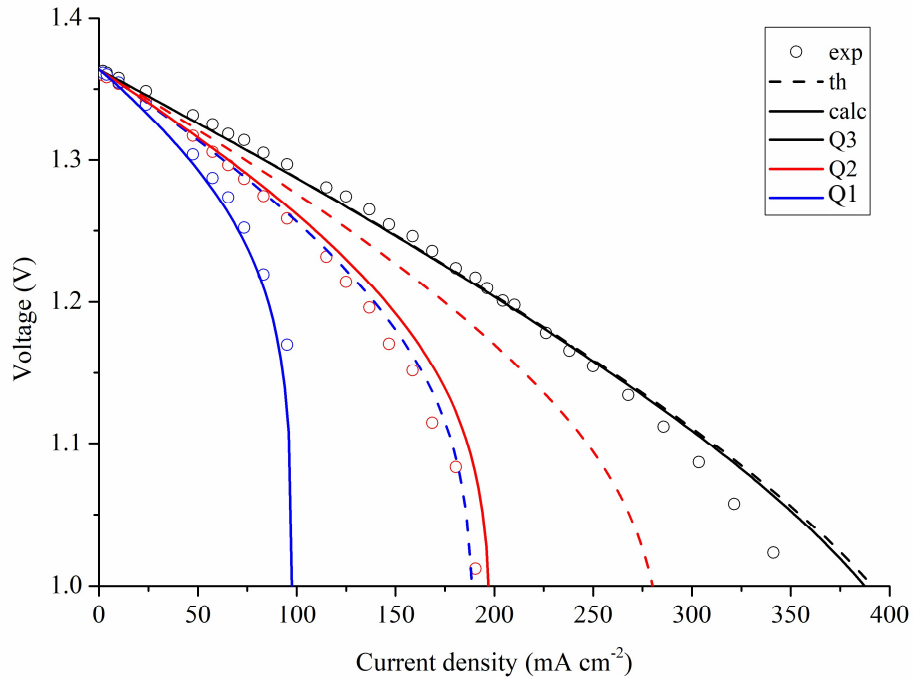


Fig. 20. Discharge polarization curves for different electrolyte flowrates corresponding to initial $SOC=0.5$ (calc – calculations ($\alpha=2, \beta=0.7$); th – literature data [76] ($\alpha=1.6, \beta=0.4$))

Experimental charge-discharge curves for different current densities were measured within the same cutoff voltage limits. The charge curves moved higher, while discharge curves moved lower with the increase of the applied current due to an increase in the corresponding overvoltages. In other words, the curves moved closer to the cutoff limits with an increase of the current, and as a result, the amount of charge passed through the cell was decreasing with the increase of the current. Due to this fact, the charge and discharge curves for different current densities started from the different initial SOC, which can be determined in accordance with the approach discussed in Sec. 3.4.

After that, the influence of crossover was investigated. First, the calculations were made considering only the diffusion-driven component (as it was proposed in [61]), which was calculated using the values of permeabilities for Nafion 115 widely available in the literature [79]. The comparison of numerical simulations with experiments is shown in the Fig. 21. Experimental data (black lines) indicate a significant difference in the charge and discharge capacity, which is mainly caused by crossover. However, obtained numerical results (red line) were not able to reflect sufficient capacity decay, noticeably underestimating the influence of crossover. Accordingly, simulation of crossover with diffusion fluxes based on the permeability values is not able to capture the influence of crossover observed in the real systems. That fact is consistent with [63,65] where authors pointed out the significant contribution of the migration and convection fluxes to the total crossover flux.

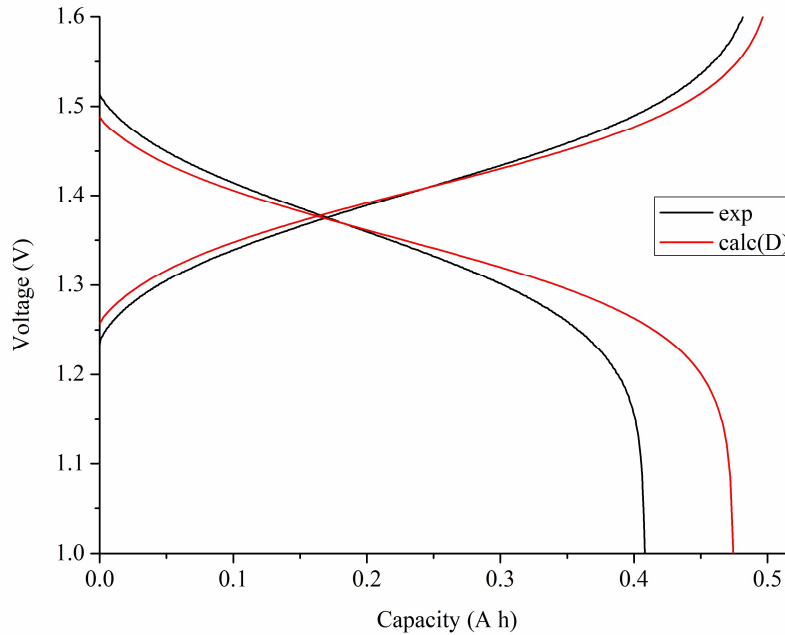


Fig. 21. Experimental and simulated charge-discharge curves (exp – experimental data, calc (D) – calculations of crossover flux with only diffusion component).

Therefore, crossover simulation was extended with migration and convection of vanadium ions. The presence of these phenomena leads to the non-linear distribution of vanadium ions in the membrane. Hence, a 0-D approach for crossover simulation proposed in [61] can not be directly implemented in this case, as it was based on the assumption of a linear concentration gradient. However, total crossover with all three components of mass transfer (diffusion, migration and convection) can be integrated across the membrane and written analytically (Eq. (15) and (16)) [63]. Such a solution allows taking into account the nonlinearity of ions distribution in the membrane keeping the simplicity of 0-D model but obtaining significantly better results (Fig. 22).

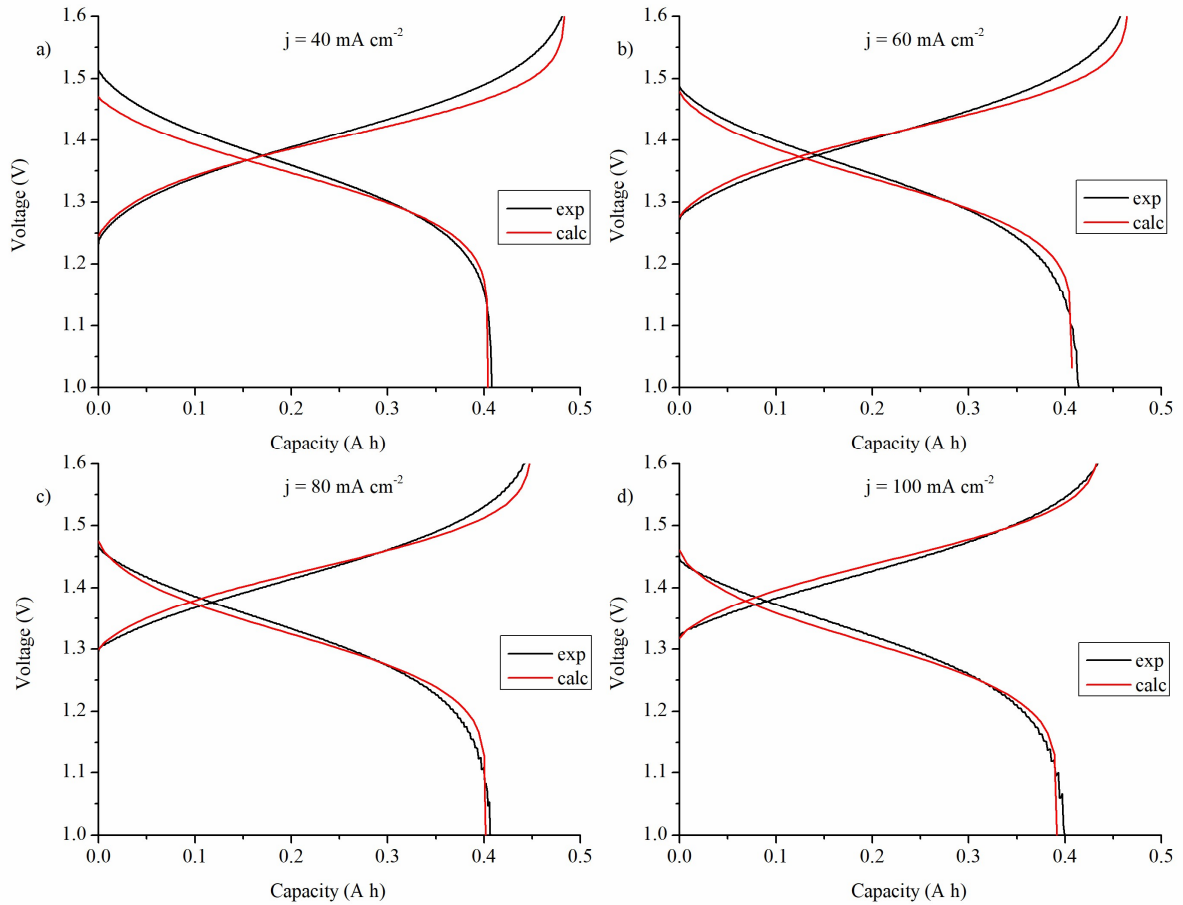


Fig. 22. Experimental and simulated charge-discharge curves (exp – experimental data; calc – calculations; $Q_3 = 8.6 \cdot 10^{-7} \text{ m}^3 \text{ s}^{-1}$).

In addition, we need to note that calculations for low current densities are located lower than experimental curves at the end of charge and beginning of discharge processes. This is likely due to the fact that experimental measurements for each current density were carried out in the sequence (one after another) starting from the higher current. Hence, the electrolyte imbalance caused by crossover became more pronounced in each next measurement. As far as the cycling at lower current densities was performed at the end of

the measurements, the accumulated imbalance could be a reason for the observed difference. It is worth noticing as well that the proposed model does not consider membrane potential difference caused by the difference in proton concentration in the half-cells, which can give a contribution to the voltage difference between calculated and measured curves as well [64].

A bit smaller capacity observed for all calculated discharge curves in comparison to experimental data is likely due to a slight overestimation of crossover flux. This might be addressed to convection term, which was estimated using the values for water content and partitioning coefficients taking from the literature, while in our experiments, they can be a bit different due to slight deviations in the membrane preparation procedure, described in Sec. 3.7. Never the less, the maximum calculation error does not exceed 4 % for all considered current densities. The good agreement between calculations and experiments gives evidence that simulation of crossover with all transport components (diffusion, migration and convection) is able to accurately capture battery behavior in the charge-discharge process and reflects corresponding capacity loss.

For a better understanding of the crossover phenomenon, it is also important to know how different crossover components contribute to the total capacity decay. Fig. 23 elucidates the influence of crossover modes on the coulombic efficiency (CE) and their contribution to the capacity loss. The results showed that the diffusion component has a significant contribution in capacity decay at low current density leading to the drop of CE of 5% (Fig. 23a), that is nearly the half of the total losses for this current (Fig. 23b).

However, the share of diffusion in the capacity decay plummets down with the increase of current density, presenting only 2% of total loss for higher current. The impact of the migration component is well under diffusion at low current, but it shows an upward trend with an increase of current density and dominates under diffusion at higher current, presenting 6% of the total loss. The major contribution in the observed capacity decay belongs to the convection-driven component, which impact is well over migration and diffusion. Presenting more than half of the capacity decay at the low current, the share of convection goes up with an increase of current and represents more than 90% of the total capacity loss for higher current density (Fig. 23b). Hence, it indicates that consideration of convection is indispensable for crossover simulation. It is worth noting that on Fig. 23a the calculated curve with all three modes of crossover (dashed blue line) is located a bit lower than the experimental data (solid black line) that might be addressed to a slight overestimation of the convection term discussed above.

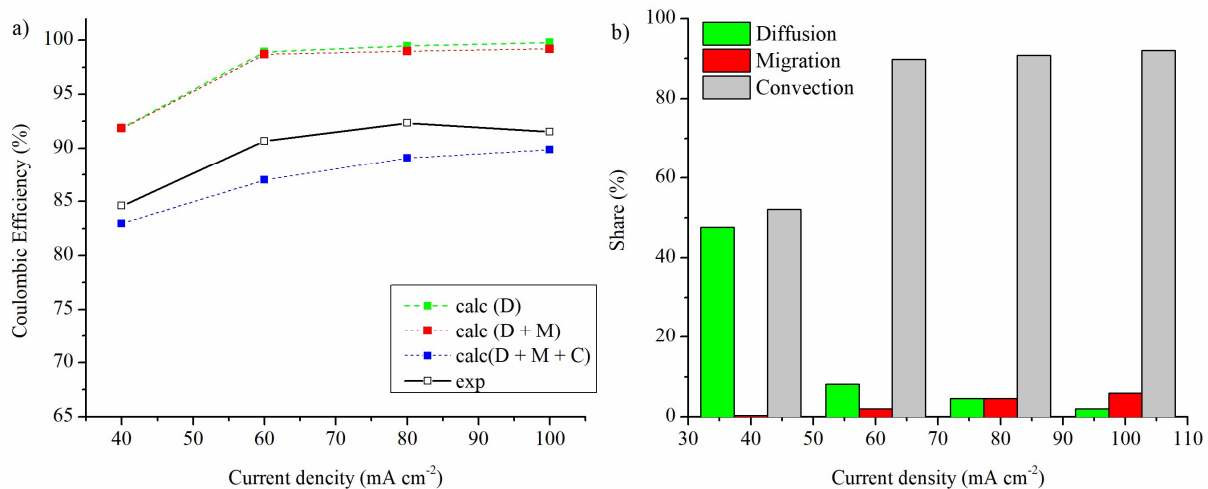


Fig. 23. Contribution of crossover components to capacity decay: a) influence of crossover modes on the coulombic efficiency; b) share of crossover components in the capacity loss.

The proposed model can estimate the performance of the cell in terms of Coulombic, voltage and energy efficiency rather well for all considered current densities (Fig. 24), capturing the trends observed in the experiments. The main difference is related to Coulombic efficiency, which is slightly underestimated by the model due to the overestimation of the crossover impact, which was discussed above. Nevertheless, the observed error is less than 5 % that is consistent with the experimental error.

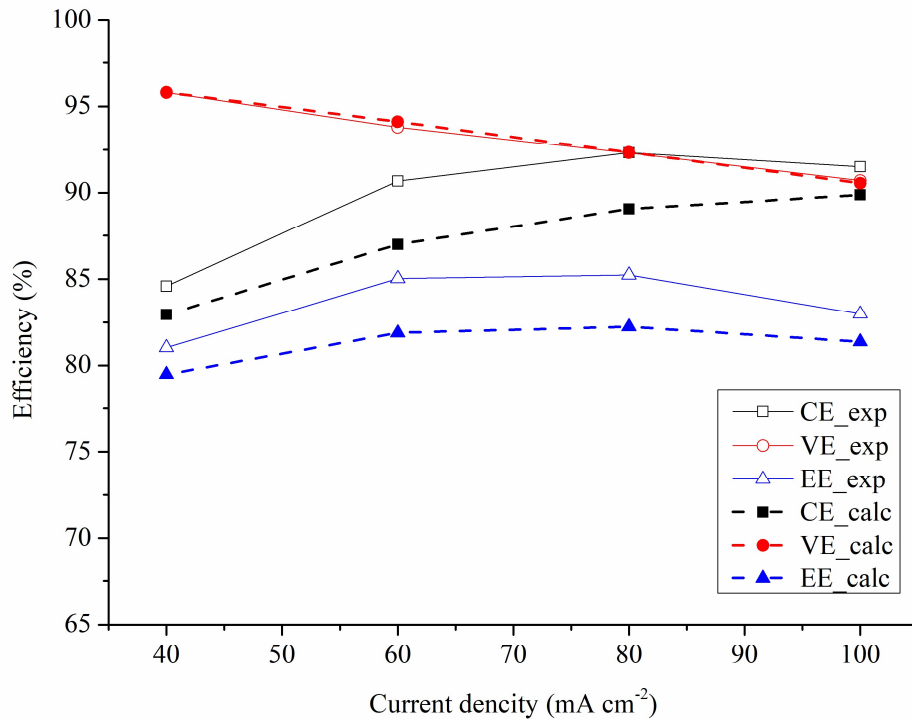


Fig. 24. Experimental and theoretical efficiencies of a single VRFB cell for $Q_3 = 8.6 \cdot 10^{-7} \text{ m}^3 \text{ s}^{-1}$ and with varying current density.

3.9 Conclusions

A 0-D dynamic model for Vanadium Redox Flow Battery (VRFB) systems has been developed targeting compromise between model accuracy and complexity to be suitable for application in control-monitoring tools and techno-economic studies.

The focus of this study is the accurate simulation of vanadium ions transport across the membrane in the framework of the macroscopic approach. The developed model was based on the state of the art approach for crossover simulation, extending it with migration

and convection components adopted from microscopic models by application of the analytical solution.

The results showed that the major contribution in the capacity decay, observed in charge-discharge cycles, belongs to the convection-driven component, which dominates under migration and diffusion. Presenting more than half of the capacity decay at the low current, the share of convection goes up with an increase of current and represents more than 90% of the total capacity loss for higher current density. Hence, consideration of convection is indispensable for crossover simulation.

Although the presented model was validated with experimental data obtained for Nafion membrane, it can be easily adapted for other membranes. Such adaptation can be done changing the coefficients related to physical membrane properties (e.g., permeability or water content), but not changing governing equations. The basic reason is that the presented model is macroscopic and, in general, averaged over the microscale inhomogeneities responsible for unique properties of the membrane.

The proposed model is able to simulate battery voltage and predict capacity decay observed in practical VRFB systems with high accuracy. Model validation showed that simulation results have a good agreement with experiments within a 5 % range. Moreover, the model has a short computational time (several seconds for a charge-discharge cycle) and does not require significant computational power (can be implemented in the ordinary laptop). Accordingly, it can be a valuable tool for the development of advanced control

strategies of electrolyte rebalancing in order to minimize the capacity loss and ensure a long service life of VRFB systems.

Chapter 4. Energy losses analysis

4.1 Introduction

As was discussed in chapter 3, the internal processes taking place in the VRFB cells can notably affect battery performance. The activation and ohmic overvoltages cause the deviation of battery voltage from the open-circuit voltage (OCV) in the whole range of operating state of charge (SOC), while concentration overvoltages become pronounced at the end of charge and discharge processes when the concentration of active species becomes limited [43]. Hence, the overvoltages can significantly change the voltage and corresponding power of the battery from its rated value. In addition, the crossover leads to the self-discharge reactions [44], which take place between the vanadium ions from different half-cells [82], reducing the amount of ‘active’ vanadium ions available for reactions [79], that in turn, shortens the available battery capacity [65]. As a result, at real working conditions, the battery will not be able to provide initial rated power and capacity. Underestimation of these parameters, in turn, can result in situations when the battery will not store enough energy while charging or provide enough energy while discharging. Therefore, the main VRFB parameters (e.g., rated power and operation time) need to be determined with high accuracy [83]. Moreover, extended sensitivity analysis of the cost-of-service for different energy storage technologies [84] showed that batteries' profitability is highly sensitive to the power and energy limits of the storage system. Hence, precise estimation of these parameters is indispensable for accurate techno-economic studies that could determine future trends for market penetration of VRFB systems.

Accurate evaluation of battery power and energy ratings required for a given loading profile can be performed through detailed simulation of internal processes taking place during battery operation. In the last decade, there were a number of works devoted to the modeling of VRFB on different levels [85]. The simplest level of modeling is based on the application of equivalent circuit models [48] that represent a cell as an electrical circuit with capacitors and resistors and thus simulating its dynamic behavior [86] also allowing to monitor battery state of charge [49] and capacity fade [50]. A more complex modeling approach is based on the lumped parameter models [51] that can simulate dynamic battery behavior [67] and can be used for advanced control strategies of large-scale VRFB systems [87] but do not provide detailed information about the spatial distribution of different parameters inside of different components of the system [53]. The most comprehensive simulations are based on 2-D [64] and 3-D models [59] that can yield information about small-scale effects [88] and internal processes in different battery components [60] but also require significant computational time [89] due to high computational complexity [90]. Hence, detailed modeling of internal processes in the VRFB systems is not feasible for applications in techno-economic studies. Therefore, many studies related to the estimation of VRFB performance at the market level usually use energy efficiency indicators (see the next paragraphs) to take into account the influence of internal processes on the battery performance.

The first simplified way for estimation of VRFB performance is to consider roundtrip energy efficiency [91], which represents the ratio of the energy released during

discharge (output energy, E_{out}) over the energy required for the charge (input energy, E_{in}) [92]. This approach can be easily applied to any system, once the value for round trip efficiency is known [24]. Roundtrip energy efficiency was used in [93] for comprehensive life cycle cost analysis of different electrical energy storage systems, while their efficiency was assumed to be constant and independent on operating conditions. After that, applying the same approach, a techno-economic study [94] was performed for large-scale VRFB systems with rated power up to 20 MW and energy capacity of 160 MWh. It should be noted that the roundtrip efficiency approach has several cons. First, energy losses can be significantly affected by the operating conditions [95]. Taking into account this factor, a study [96] was performed for cost analysis of two different RFB technologies based on vanadium and iron-chromium considering the influence of loading current on their roundtrip energy efficiency. Second, roundtrip energy efficiency has rather narrow constraints as it does not allow considering different operating conditions for charging and discharging. However, a number of studies showed that VRFB performance could be significantly improved with the application of asymmetric operation conditions (i.e., different flow rates [97] and currents [98] for charging and discharging). Thus, the battery performance needs to be investigated individually for charge and discharge modes.

The second way for evaluation of VRFB performance is based on the energy efficiency indicators individually estimated for charging and discharging. The first approach for separate analysis of energy losses in charge and discharge processes was proposed in [99] and was based on comparison with open-circuit voltage (OCV). This

approach was used for investigation of the VRFB energy efficiency depending on the SOC and on the number of cells and determination of the optimal operating conditions and stack size. Further, different charge and discharge energy efficiencies were considered for the determination of optimal VRFB size that could provide load frequency control in the power system [100]. After that, energy and voltage efficiencies were considered for a more accurate estimation of the reactor (tank with electrolyte) parameters [101] and the corresponding cost of electrolyte and reactor components [102]. While the considered studies can provide important results, they still are not able to reflect the nonlinear behavior of VRFB systems, which can be very critical for stable grid operation, especially at the rapid increase in the power consumption. Hence, more accurate approaches are required for the evaluation of VRFB performance.

The third way for estimation of the main technical indicators of VRFB systems is based on the simplified modeling approaches. Such an approach was used in [38], where a cost-performance model was based on the electrochemical model for VRFB stack [103] that allowed determining the stack size and total system cost with good accuracy. While this approach is very important for the understanding of main factors influencing the VRFB cost, it does not provide the tools that can be used for performance estimation of different systems and determination of proper usage protocols. Recently, a techno-economic study was performed considering the charging and discharging energy efficiencies obtained with the application of a lumped parameter model [104]. The efficiencies were investigated for different stacks' rated powers and further used for the determination of optimal stack size

in residential applications. This study demonstrated interesting results, but the considered efficiency was related to stack power and not to the loading current. Hence, the presented data were strongly connected to the considered stack configuration and could not be used for the performance estimation of different VRFB systems.

It is worth noting as well that, to date, there was not enough attention to capacity decay. All considered studies are mainly focused on energy losses, while they do not consider the change of capacity for different operating conditions (loading currents). However, the internal losses in the cell can significantly affect the battery capacity during operation [105]. For example, higher current in charging operation will increase the overpotentials and consequently, the battery voltage will be increased. As a result, the upper cut-off voltage will be reached earlier. Hence, the battery will operate for a smaller period of time, and in addition, less battery capacity will be used (less energy will be stored) [106]. These factors need to be taken into account while designing VRFB systems in order to avoid serious battery damages and failures in the power grid. Therefore, investigation of the operation time, peak power and available battery capacity depending on different operating conditions is a very important issue for the practical application of VRFB systems [107].

In this chapter, we present a new approach for the estimation of key characteristics of VRFB systems operating at different loading currents. The proposed method is based on the simplified energy efficiency indicators, which are derived from the results of detailed numerical simulations taking into account the non-linear behavior of the VRFB systems.

The considered approach has higher accuracy (in comparison to existing simplified solutions) for estimation of battery power/capacity and operation time while it does not require significant computational time allowing to obtain battery characteristics directly from the geometry of VRFB stacks and tanks. Accordingly, the proposed method can be used for the development of an accurate battery usage schedule (protocol) that could prevent over/underestimation of committed battery power, operation time and capacity and ensure stable battery operation at real operating conditions.

4.2 Mathematical model

The proposed energy efficiency investigation was performed using a 0-D dynamic VRFB model described in Chapter 3. The model is implemented in MATLAB and allows determining the battery voltage ($U_{bat}(t)$) depending on the main operating conditions (current density (j), electrolyte flow rate (Q) and ambient temperature (T)) focusing on precise simulation of vanadium ions crossover with diffusion, migration and convection. In this chapter, the model is extended for the case of stack simulation.

As it was discussed in Chapter 2, in order to obtain higher voltages, the VRFB cells are joint together and connected in a series circuit. Cells in the stack are connected in series circuits; hence the stack voltage (U_{bat}) presents a sum of voltages on each cell. Thus, the simplest way for stack simulation is to multiply the voltage of a single cell by the number of sells (n_{ce}). It should be noted here that we do not take into account the shunt currents due to their small impact during dynamic battery operation [108]:

$$U_{bat}(t) = n_{ce} U_{ce}(t) \quad (31)$$

where the voltage of a single cell ($U_{ce}(t)$) is calculated according to the electrochemical model Eq.(4).

In addition, the neighbor cells in the stack are connected with each other through a common bipolar plate, and thus, the total equivalent electric resistance of the battery (R_{bat}^*) should be calculated as follows:

$$R_{bat}^* = n_{ce} R_{ce}^* \quad (32)$$

In addition, the cells in the stack have a parallel connection for electrolyte supply in order to have the same electrolyte composition in the inlet. Thus, the mass transport model will be the same as it was described in the previous Chapter, with different coefficient γ that should be calculated as follows:

$$\gamma = \frac{1}{n_{ce} V_{ce}} \quad (33)$$

4.3 Model validation

The model was validated with experimental data for a kW-scale VRFB system with the stack consisted of 14 cells and a membrane area of 875 cm² [109]. The validation was made for charge-discharge curves at two different current densities of 50 and 70 mA cm⁻², respectively and the simulations showed good agreement with experimental data with an average error less than 5% (Fig. 25).

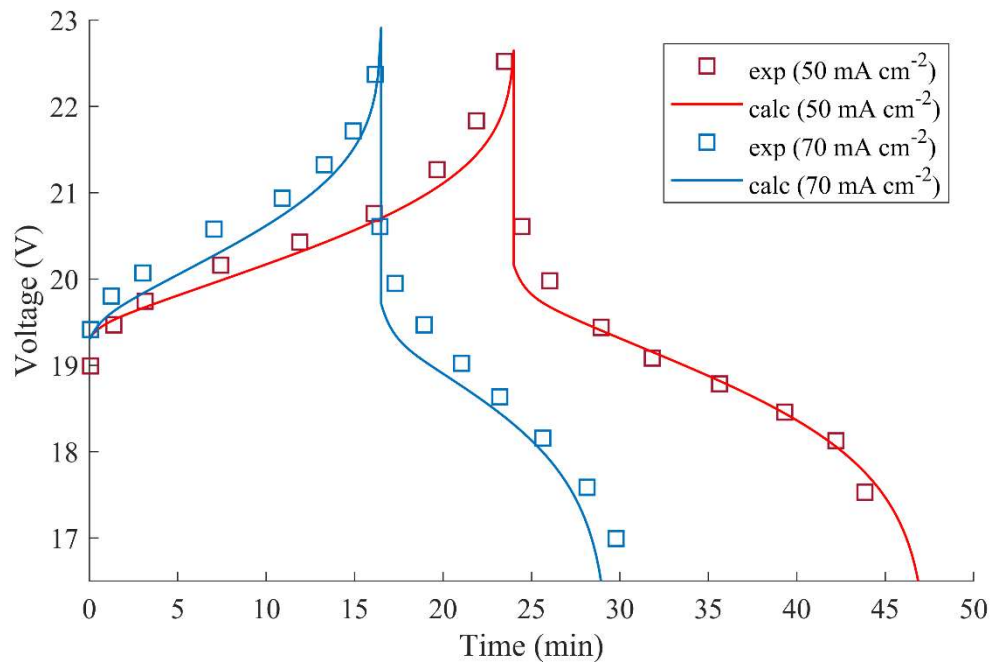


Fig. 25. Voltage of 1 kW-class VRFB stack in charge-discharge operation at fixed current density (exp – experimental data [109], calc – simulation results).

4.4 Simulated case studies

In this study, the simulations are performed for 5 kW/15 kWh VRFB system reported in the literature by Skyllas-Kazacos [43]. The battery stack consisted of 40 individual cells with a membrane area of 1500 cm². Each tank contained 200 L of electrolyte compressing 2M of vanadium and 5M of sulphuric acid. The electrolytes were circulated by the pumps through the cells with a volumetric flow rate of 1.0 L s⁻¹. Each cell was configured with Nafion 115 membrane, which separated the half-cells. The averaged cell resistivity was assumed to be constant during operation and has a value of 2 Ω cm². The detailed stack parameters are listed in Table 6.

Table 6. Specifications of the VRFB and parameters in the simulation [43].

Characteristics	Unit	Value
Faraday's constant, F	C mol^{-1}	96485
Gas constant, R	$\text{J K}^{-1} \text{mol}^{-1}$	8.31
Formal potential, U_0^*	V	1.4
Initial concentration of vanadium ions, c_0	mol m^{-3}	2000
Tank volume, V_{tk}	m^3	0.2
Number of cells, n_{ce}	-	40
Operating temperature, T	K	298
Membrane surface area, A_m	m^2	0.15
Porous electrode dimension	m	$0.5 \times 0.3 \times 0.003$
Cross-section area of electrode, A_{ed}	m^2	$9.0 \cdot 10^{-4}$
Half-cell volume, V_{ce}	m^3	$4.5 \cdot 10^{-4}$
Mass transfer coefficient, k_m	m s^{-1}	$1.6 \cdot 10^{-4} u^{0.4}$
Membrane thickness, d_m	m	$1.25 \cdot 10^{-4}$
Membrane conductivity, σ^m	S m^{-1}	6.0
Concentration of fixed sites, c_f [56]	mol m^{-3}	1200
Water electro-osmotic coefficient, ξ	-	3.0
Water content coefficient, λ [72]	-	22.0
Permeability coefficients [110]		

P_2	$\text{m}^2 \text{s}^{-1}$	$8.77 \cdot 10^{-12}$
P_3	$\text{m}^2 \text{s}^{-1}$	$3.22 \cdot 10^{-12}$
P_4	$\text{m}^2 \text{s}^{-1}$	$6.83 \cdot 10^{-12}$
P_5	$\text{m}^2 \text{s}^{-1}$	$5.90 \cdot 10^{-12}$
Partition coefficients [70]		
K_2	-	1.15
K_3	-	0.76
K_4	-	0.6
K_5	-	0.77

The simulations are conducted by using MATLAB ODE solver. The battery was simulated at four different current densities (40 mA cm^{-2} , 60 mA cm^{-2} , 80 mA cm^{-2} and 100 mA cm^{-2}). During each cycle, the VRFB was charged and discharged to cut-off voltages of 64 V and 40 V, which corresponded to $\sim 90\%$ and $\sim 10\%$ of SOC, respectively.

Proposed approach

The proposed approach is presented on Fig. 26 and based on the interpolation of the efficiencies derived from the direct numerical simulations (yellow part) and their further application for estimation of battery power and capacity under different loading currents (green part).

On the first step (yellow part), the battery performance was analyzed individually for charge and discharge. The operation time, power and energy obtained from the

simulations were related to their ideal values derived from the geometrical size of the system, and hence, voltage and coulombic efficiencies depending on different operating conditions were obtained. After that, the obtained efficiencies were interpolated and the analytical dependencies for the coulombic and voltage efficiencies on the different loading current densities were derived.

On the second step (green part), the derived dependencies were used to determine the battery characteristics for different operating conditions (loading currents) basing on the ideal battery characteristics. The advantage of the proposed approach is that the interpolated efficiencies can be easily implemented in techno-economic models while keeping the simplicity of the standard approach with constant efficiencies. The schematic representation of the proposed approach is shown in Fig. 26.

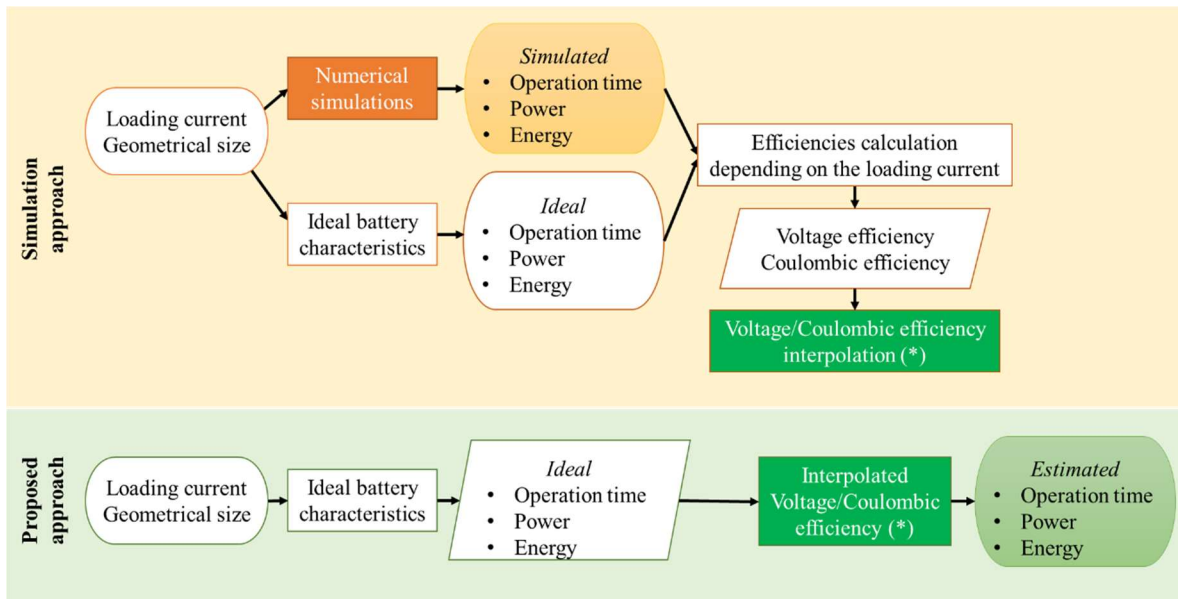


Fig. 26. The block-schema of proposed approach for estimation of the main VRFB characteristics.

4.5 Performance indicators

The influence of total losses on the battery voltage during charge and discharge is shown in Fig. 27, where the brown-grey area presents the stored amount of energy in the charging and used in discharging processes. The grey area shows the energy losses during battery operation due to the influence of internal processes in the cell. The light-orange area shows the potential capacity that could be used theoretically but is never achieved due to the impact of internal processes.

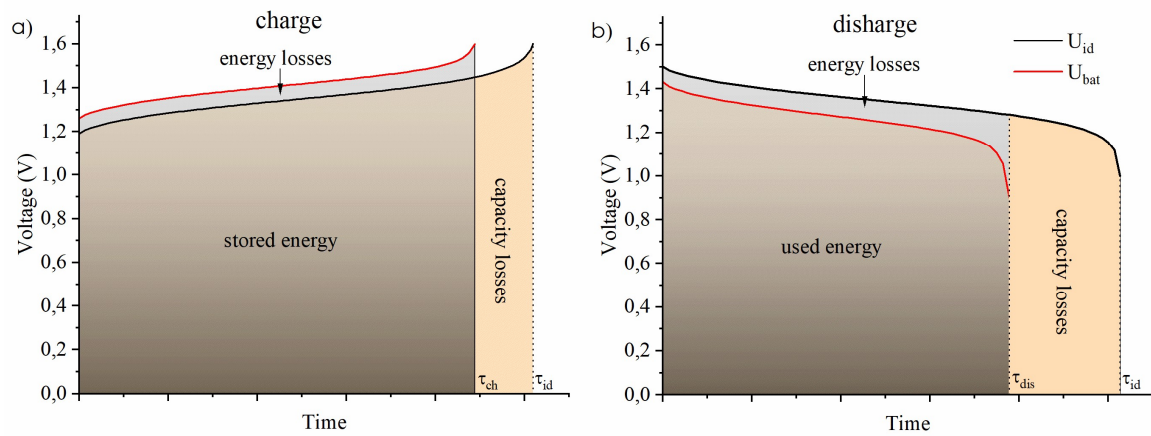


Fig. 27. Effective amount of stored/released energy and capacity losses: a) charge process; b) discharge process.

To estimate the energy performance of the battery in charging and discharging operation, some universal benchmark indicators (which are the same both for charging and discharging) are required. Hence, the most important battery parameters were related to the power and operation time determined from the geometrical sizes of the VRFB system.

The average rated power of VRFB system depending on the loading current density (j) can be determined from the geometrical cell size (if the membrane area (A_m) is known) and number of cells in the stack (n_{ce}) as following:

$$\langle P_{id} \rangle (j) \approx j A_m n_{ce} U_0^* \quad (34)$$

The operation time can be estimated from the volume of the tanks (V_{tk}), initial total vanadium ions concentration (c_0) and membrane area as:

$$\tau_{id}(j) = \frac{\kappa_{\max, id}}{I} = \frac{c_0 F V_{tk}}{j A_m n_{ce}} \quad (35)$$

It should be noted that power and time are estimated in accordance with Eq.(34) and Eq.(35) present characteristics of an ideal battery. In reality, the internal losses will lead to deviation of battery operation parameters from their ideal values.

The average power of the battery at real operating conditions can be estimated with the application of voltage efficiency (ε^v):

$$\text{for charging operation: } \langle P_{bat} \rangle_{in}(j) = \frac{\langle P_{id} \rangle (j)}{\varepsilon_{ch}^v(j)} \quad (36)$$

$$\text{for discharging operation: } \langle P_{bat} \rangle_{out}(j) = \varepsilon_{dis}^v(j) \langle P_{id} \rangle (j) \quad (37)$$

In order to estimate operation time at real conditions, the coulombic efficiency (ε^q) (which is actually dimensionless useable capacity in our case) can be applied:

$$\text{for charging operation: } \tau_{ch}(j) = \varepsilon_{ch}^q(j) \tau_{id}(j) \quad (38)$$

$$\text{for discharging operation: } \tau_{dis}(j) = \varepsilon_{dis}^q(j) \tau_{id}(j) \quad (39)$$

In addition to power and operation time, it is also important to know the amount of energy required for battery charging and energy that can be delivered to the consumer during discharge.

The energy required for charging (E_{in}) is connected with the corresponding energy stored in the battery (E_{stor}) through charging voltage efficiency (at constant current density in charging operation):

$$E_{in}(j) = \frac{E_{stor}(j)}{\varepsilon_{ch}^v(j)} = \frac{\varepsilon_{ch}^q(j)}{\varepsilon_{ch}^v(j)} \langle P_{id} \rangle(j) \tau_{id}(j) \quad (40)$$

where the stored energy is estimated as:

$$E_{stor}(j) = \varepsilon_{ch}^q \langle P_{id} \rangle(j) \tau_{id}(j) \quad (41)$$

The energy delivered (E_{out}) to the consumer during discharge is connected with stored energy as:

$$E_{out}(j) = \frac{\varepsilon_{dis}^q(j)}{\varepsilon_{ch}^q(j)} \varepsilon_{dis}^v(j) E_{stor}(j) \quad (42)$$

Finally, taking into account Eq.(41) we can rewrite it as follows:

$$E_{out}(j) = \varepsilon_{dis}^q(j) \varepsilon_{dis}^v(j) \langle P_{id} \rangle(j) \tau_{id}(j) \quad (43)$$

As can be seen from the equations presented above, the input and output parameters are connected with ideal parameters through the coulombic and voltage efficiencies, which depend on the loading current density. However, many techno-economic studies for VRFB systems do not take into account the influence of internal losses on the power and operation time, considering only charging and discharging energy efficiencies, which are assumed to

be constant. In other words, in the framework of such approach (which further we call ‘standard’), energy required for charge and provided to the consumer during discharge are connected with stored energy though following equations:

$$E_{in}^{st} = \frac{E_{stor}}{\varepsilon_{ch}^{e,st}} = \frac{\langle P_{id} \rangle(j) \tau_{id}(j) \Delta SOC}{\varepsilon_{ch}^{e,st}} \quad (44)$$

$$E_{out}^{st} = \varepsilon_{dis}^{e,st} E_{stor} = \varepsilon_{dis}^{e,st} \langle P_{id} \rangle(j) \tau_{id}(j) \Delta SOC \quad (45)$$

where $\Delta SOC = SOC_{final} - SOC_{init}$ presents the operating range of SOC (in our case $\Delta SOC \approx 0.8$).

It is worth noting, the standard approach can lead to significant errors because of disregarding the impact of internal losses. To demonstrate it, we have compared the standard approach with our method assuming that $\varepsilon_{ch}^{e,st} = \varepsilon_{dis}^{e,st} = 0.94$ [101].

4.6 Results and discussion

First, the influence of internal losses was analyzed considering the polarization curve (Fig. 28). In the ideal case, when there are no losses in the cell, the battery voltage (blue line) remains constant with a change of current density. However, in reality (black dots) the battery voltage drastically decreases with the increase of current density. It should be noted as well that the contribution of ohmic and concentration losses increases with the increase of current density. The influence of ohmic losses (grey region) has a linear behavior (due to the linear connection of ohmic overvoltages with the current in the Ohm’s law). Nevertheless, the influence of concentration losses (orange region) has significantly nonlinear behavior, noticeably enlarging with the growth of current density and leading to

a drastic drop in battery voltage. Such behavior can be explained by the mass transport limitations, which take place in the electrode||electrolyte interface due to the concentration gradient on the surface of the electrode. The increase of current density requires more reactants for “current production”; hence a larger amount of reactants moves from electrolyte in the cell to the surface of the electrode to ensure higher currents. This, in turn, causes the growth of mass transport losses on the surface of the electrode that implies an increase of the corresponding voltage drop.

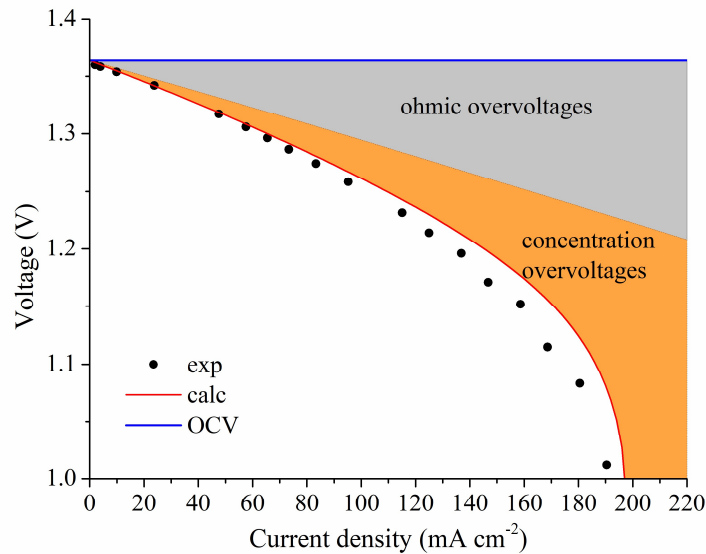


Fig. 28. Polarization curve with the influence of internal processes depending on current density: exp – experimental data [111], calc – simulation results, OCV – open-circuit voltage.

In addition to ohmic and concentration losses, the crossover phenomenon (transport of vanadium ions across the membrane) leads to the self-discharge reactions and shortens available battery capacity that can have a crucial role during battery operation. These

processes were discussed and analyzed in the previous chapter, so here we do not go into detail while the reader can find them in Sec. 3.8.

The joint effect of all of the processes discussed above can lead to a significant deviation of main battery parameters (rated power and operation time) from their ideal values that can be seen in Table 7, which presents the ideal values of the key VRFB parameters and the values obtained from numerical simulations.

Table 7. The key VRFB parameters for different current densities.

Current, A	60	90	120	150
Current density, mA cm ⁻²	40	60	80	100
τ_{id} , h	4.47	2.98	2.23	1.79
τ_{di} , h	4.03	2.65	1.95	1.51
τ_{ds} , h	3.16	2.09	1.55	1.23
$\langle P_{id} \rangle$, kW	3.36	5.04	6.72	8.40
$\langle P_{bat} \rangle_{in}$, kW	3.45	5.25	7.10	8.98
$\langle P_{bat} \rangle_{out}$, kW	3.24	4.78	6.28	7.73

The total influence of internal losses on the battery voltage during battery operation at higher current density is demonstrated in Fig. 29. The share of ohmic losses is shown by grey color and determined as the region between calculated battery voltage (red line) and battery voltage without ohmic overvoltages or ir-free voltage (black dashed line). The share of concentration losses is shown by the orange color and determined as the region between

the ir-free voltage curve and equilibrium potential curve calculated by the Nernst equation, with crossover (blue dashed line). The contribution of crossover is shown by yellow color and estimated as the region between Nernst curves with crossover (blue dashed line) and without it (solid black line).

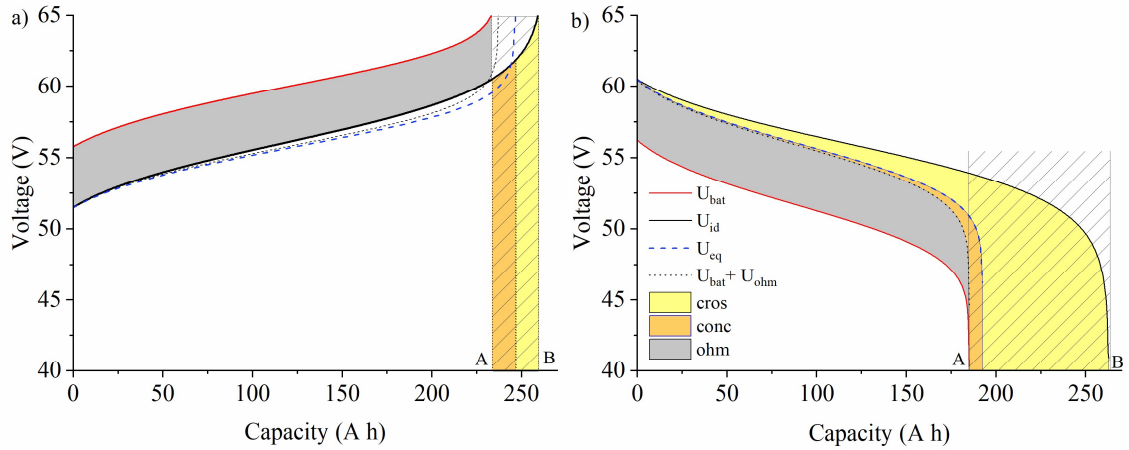


Fig. 29. Influence of internal processes on the battery voltage: a) charge; b) discharge; ohm – ohmic losses; conc – concentration losses; cros – crossover losses.

As it can be seen, the dominant role in voltage deviation belongs to ohmic losses in both charging and discharging operation, while concentration losses and crossover are mainly responsible for the capacity drop. The influence of these processes depending on the current density, will be investigated more detailed in the further sections in terms of voltage and coulombic efficiencies.

4.6.1 Voltage efficiency

In this section, the influence of internal processes on the voltage efficiency as a function of current density was analyzed. Fig. 30 shows the charging and discharging

voltage efficiencies calculated in accordance with Eq.(36) and Eq.(37). As can be seen, the voltage efficiency demonstrates the same trend in charging and discharging operation linearly declining with the increase of current density. Such linear behavior of the voltage efficiencies can be explained by the fact that the considered range of current densities corresponds to the linear region of the polarization curve where the internal processes intensify linearly with an increase of current density.

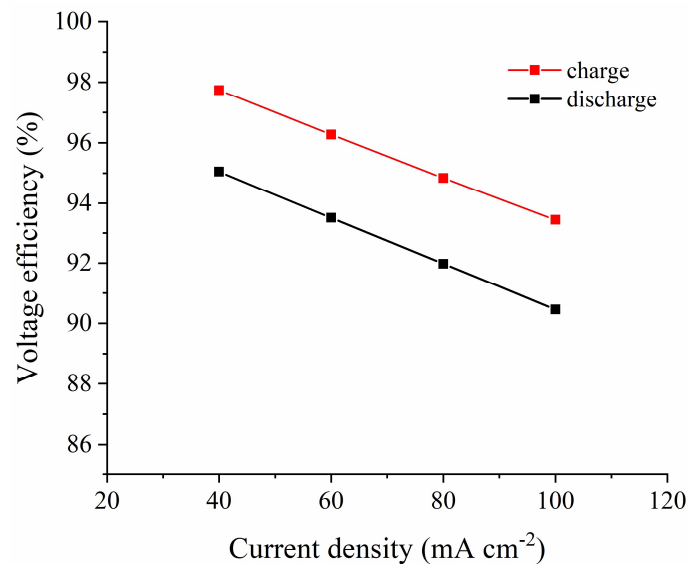


Fig. 30. Stack voltage efficiency at different charging and discharging current densities (red – charge mode, black – discharge mode).

Interpolating the obtained results, the voltage efficiency during charge and discharge could be analytically described as a function of dimensionless current density (\bar{j}):

$$\varepsilon_{ch}^v(\bar{j}) = -7 \cdot 10^{-4} \bar{j} + 1.0058 \quad (46)$$

$$\varepsilon_{dis}^v(\bar{j}) = -8 \cdot 10^{-4} \bar{j} + 0.9811 \quad (47)$$

Here and further, the dimensionless current density (\bar{j}) presents the current density related to 1 mA cm⁻².

It is worth noticing as well that charging voltage efficiency is higher than discharging one for all considered current densities. To understand the reason of this phenomenon, the contribution of internal processes to the corresponding voltage drops should be investigated. In order to do that, the share of each process presented in Fig. 20 was analyzed for each current density and plotted as a bar chart in Fig. 31. As it can be observed, the internal losses in charging operation are mainly constituted by ohmic and concentration overpotentials while in discharging; in addition to that, the battery voltage is also significantly affected by the crossover. It should be noted that the concentration losses have an insignificant impact on battery performance and demonstrated the symmetric influence on the voltage losses during battery operation (approx. 2% of total losses in both charging and discharging), while the effect of crossover is significantly more intensive in discharge. Thus, the lower value of voltage efficiency in discharging operation is mainly connected with the asymmetric behavior of crossover.

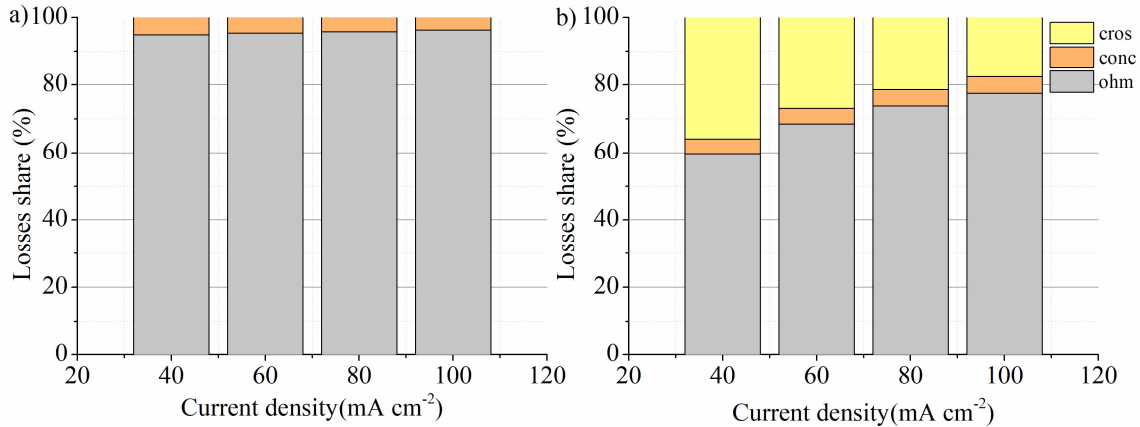


Fig. 31. Contribution of internal processes to the voltage losses in the stack: a) charge; b) discharge (ohm – ohmic losses, conc – concentration losses, cros – crossover losses).

The small impact of the concentration losses can be addressed to the fact that the considered range of operating current densities is located rather far from the limiting current. Hence, the mass transport limitations are rather small and do not dominate over the other internal processes. At such operating conditions, the concentration overvoltages become pronounced only at the beginning and at the end of battery operation, which presents a small period of time comparing to the total operation time. As a result, the integral impact of concentration overvoltages is rather small in the total voltage losses.

In order to understand the asymmetric behavior of crossover, we need to look at the main driving forces for the transport of vanadium ions across the membrane. The crossover flux is formed by three components of mass transfer [69]: diffusion (due to concentration gradient), migration (due to electric field) and convection (due to bulk movement of

electrolyte). It was shown in [63] that convection of electrolyte through the membrane is mainly driven by water electro-osmotic drag, and hence, the convective flux has the same direction as the electric field in the membrane. Thus, migration and convection fluxes are directed in the same way as electric current. As it was discussed in the previous chapter, the diffusion of V^{2+}/V^{3+} ions is directed towards the positive half-cell, while the diffusion of VO^{2+}/VO_2^+ ions has the opposite direction. It is worth noting as well that the diffusion fluxes have the same direction both in charge and discharge modes. It might be addressed to the fact that the transferred V^{2+}/V^{3+} ions do not exist in the positive half-cell owing to their fast reactions with VO^{2+}/VO_2^+ ions there. Thus, the concentration of V^{2+}/V^{3+} ions is always higher in the negative half-cell and their concentration gradient is directed towards the positive half-cell. The same explanation can be applied for the diffusion flux of VO^{2+}/VO_2^+ ions, which is always directed towards to the negative half-cell. At the same time, the migration and convection fluxes change the direction in charge and discharge modes owing to different directions of charging and discharging currents. Thus, in discharge mode, the migration and convection reinforce the crossover fluxes of V^{2+}/V^{3+} ions and mitigate the crossover fluxes of VO^{2+}/VO_2^+ ions, while in charge mode, it is the other way round. In addition, it was shown in our previous work [112] that the integral effect of migration and convection for each type of vanadium ions can be accounted for as a coefficient for the corresponding diffusion flux. As a result, the intensity of the crossover flux for each ion is governed by the diffusion rate, which is determined by the ion's diffusion coefficient. The diffusion coefficients for V^{2+}/V^{3+} ions are higher than the

diffusion coefficients for VO^{2+}/VO_2^+ ions. Thus, the total crossover rate is higher in discharging and lower in charging operation.

As can be seen from Fig. 32, the operation time for the ideal battery has a reciprocal dependency on the current density. It can be addressed to the fact that the maximum theoretical battery capacity is fixed by the volume of electrolyte in the tank and total concentrations of vanadium ions. An increase of loading current intensifies the electrochemical reactions, and hence, the battery starts to operate rapidly. As a result, the available capacity will be “taken” faster and the operation time will reduce.

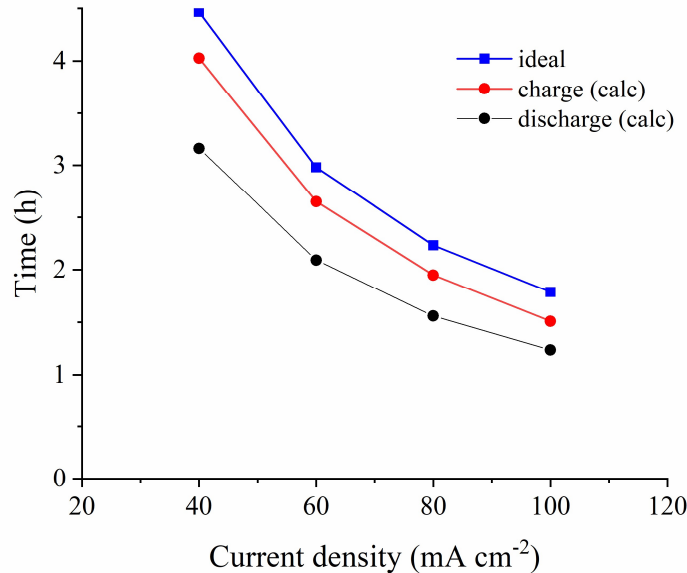


Fig. 32. Battery operation time at different charging and discharging current densities (blue – ideal case (no losses), red – simulations for charge mode, black – simulations for discharge mode).

The influence of internal processes results in a larger decrease of operation time than in the ideal case. This can be addressed to the fact that an increase of current density

accelerates the internal processes, and consequently, intensify the corresponding overvoltages. As a result, the deviation of battery voltage from the voltage of the ideal battery (which corresponds to equilibrium potential) will increase and the cut-off limits will be reached earlier, leading to shorter operation time. Moreover, the simulations showed that in discharging operation, the battery operation time is significantly shorter than the ideal value (Fig. 32). That can be addressed to the influence of crossover, which represents the main reason for the observed decrease of operation capacity (and time) (Fig. 29). As was discussed above, the crossover has an asymmetric behavior having a stronger impact in the discharge process, and hence, leading to a more notable time shortage.

4.6.2 Coulombic efficiency

In this section, the influence of internal processes on the coulombic efficiency was investigated. As it was shown in Fig. 27, in real operating conditions, the useable amount of battery capacity is smaller than the theoretical value. Fig. 33 shows the coulombic efficiencies calculated in accordance with Eq.(38) and Eq.(39). As it can be seen, the useable battery capacity reduces with the increase of current density. It can be addressed to the fact that higher current density intensifies the internal losses and implies the reduction of operation time. The shorter operation time, in turn, shortens the amount of electrolyte used for battery operation. As a result, not all vanadium ions that could potentially react were involved in the process, determining the battery capacity decay. It is worth noting as well, that battery demonstrated better performance in charging operation with charging coulombic efficiency around 88%, which is notably higher the discharging

one (which is around 70%). Moreover, as it can be observed from Fig. 33, the charging efficiency manifests slightly nonlinear behavior with an increase of current density.

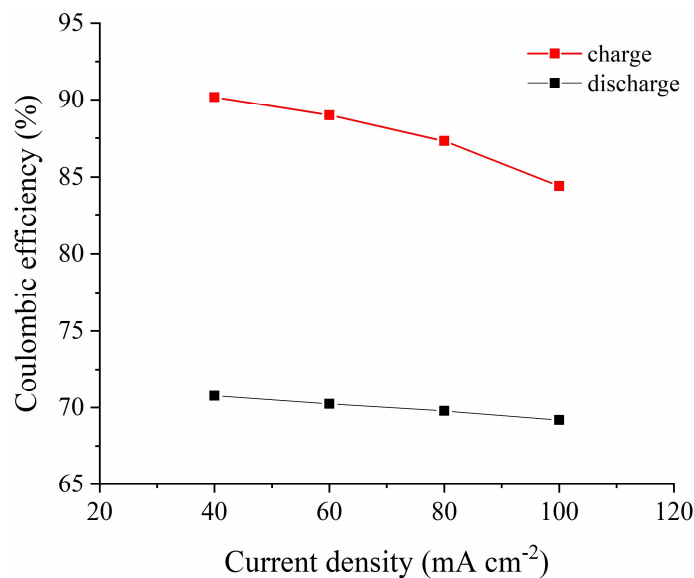


Fig. 33. Coulombic efficiency (useable battery capacity) at different charging and discharging current densities (red – charge mode, black – discharge mode).

In order to understand such nonlinear behavior, we need to look at the main internal processes, which contribute to the capacity decay. Fig. 34 illustrates that the observed shortage of capacity is mainly determined by concentration overvoltages and crossover. The nonlinear behavior of coulombic efficiency in charging operation can be attributed to the influence of concentration overvoltages, which have a larger share in charge than in the discharge process and grow with an increase of current density (due to intensification of mass transport processes on the surface of electrodes).

At the same time, the capacity drop in discharging operation demonstrates the linear decay and shows an insignificant sensitivity to the increase of current density, gradually

decreasing from 71% to 69%. It can be attributed to the fact that capacity decay in discharge is mainly (more than 90%) caused by the crossover. Insignificant change of crossover flux for different current densities can be addressed to the fact that for large scale cells, the crossover flux is mainly governed by the diffusion component, which does not depend on the current density. It also should be noted that the influence of crossover is more significant in discharging than in charging operation, as explained in Sec. 4.6.1.

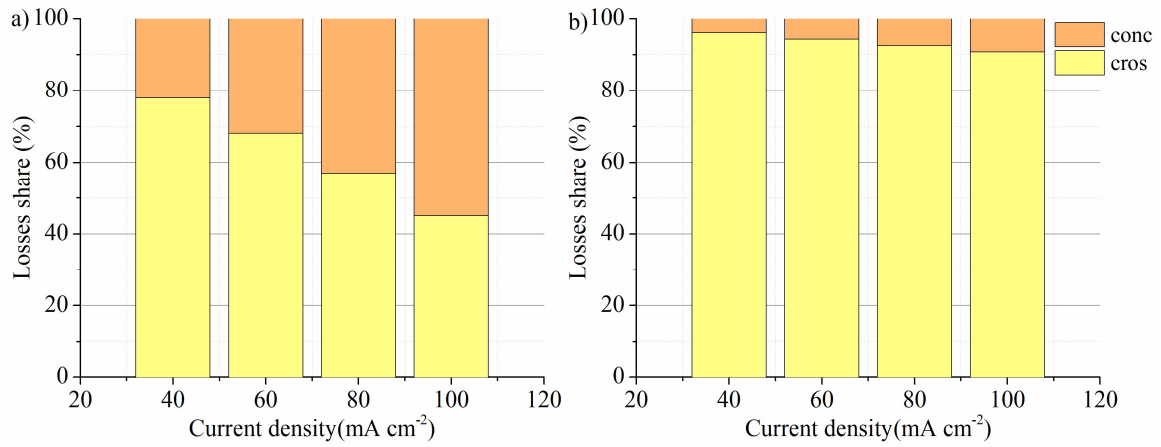


Fig. 34. Contribution of internal processes to the capacity decay during battery operation: a) charge; b) discharge (conc – concentration losses; cros – crossover losses).

Interpolating the obtained results, we proposed the analytical dependencies for charging and discharging coulombic efficiencies as a function of dimensionless current density (\bar{j}):

$$\varepsilon_{ch}^q(\bar{j}) = -10^{-5}\bar{j}^2 + 5 \cdot 10^{-4}\bar{j} + 0.8965 \quad (48)$$

$$\varepsilon_{dis}^q(\bar{j}) = 3 \cdot 10^{-4}\bar{j} + 0.7182 \quad (49)$$

4.6.3 Charge-discharge operation

In this section, we studied the charge-discharge battery operation considering different loading currents and comparing different approaches for estimation of battery performance described in Sec.4.5.

First, the most extreme cases for battery operation were considered: slow charge – slow discharge (SC-SD) and fast charge – fast discharge (FC-FD). The battery was charged starting from initial SOC of 10% till the upper cut-off voltage of 64 V. After that, the battery was discharged with the same current density till the lowest cut-off voltage of 40 V. The corresponding loading profiles and voltage curves are presented in Fig. 35.

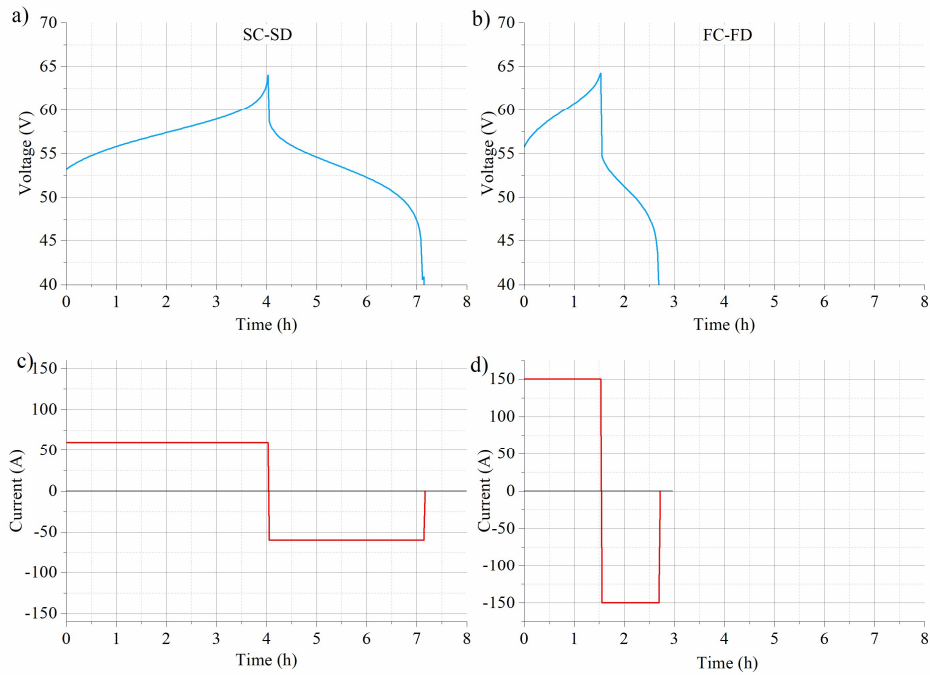


Fig. 35. Current profiles and voltage curves for SC-SD and FC-FD operation modes: a) voltage profile (slow mode); b) voltage profile (fast mode); c) loading current (slow mode); d) loading current (fast mode).

In the slow mode, which is related to the lowest current density (40 mA cm^{-2}), the internal processes are not very intensive, and as a result, the losses are low. On the contrary, the fast mode corresponds to the highest current density (100 mA cm^{-2}), which notably accelerates the internal processes leading to significant losses. The corresponding amounts of energy taken from the grid (E_{in}) and delivered back (E_{out}) are shown in Fig. 36.

In the presented data (Fig. 36), we assumed that the numerical simulation results (labeled as ‘NS’) could be used as a reference value for comparison of the proposed approach (labeled as ‘PR’) and standard approach (labeled as ‘ST’) described in Sec.4.5. First, comparing the battery performance in slow and fast modes, we can see that the energy required for battery charging in these two cases is nearly the same and presents the value of 14 kWh. It should be noted that this value is smaller than the theoretical one on the 10% that is mainly related to the initial SOC of 10%.

The discharge mode is characterized by larger energy losses, and thus, a smaller amount of energy can be delivered to the consumer (E_{out}). Moreover, in the fast mode, the delivered energy is smaller on 1 kWh than in the slow mode and presents a value of 9 kWh that is 60% of theoretical capacity. It can also be observed that the proposed approach slightly overestimates the battery performance both in charging and discharging operation, and hence, demonstrates a smaller amount of energy required for charge and a higher amount of energy released during discharge. It can be addressed to our assumption that averaged equilibrium potential equals formal potential ($U_o^*=1.4 \text{ V}$). However, in reality, this value is slightly smaller due to shorter battery operation time and a smaller range of

OCV (which corresponds to the equilibrium potential in our considerations). Nevertheless, the highest error for estimation of energy amounts in the framework of the proposed approach (that was observed for the fast mode operation) presents less than 6%. At the same time, the standard approach showed a notable deviation from the simulated results leading to an error of 20%.

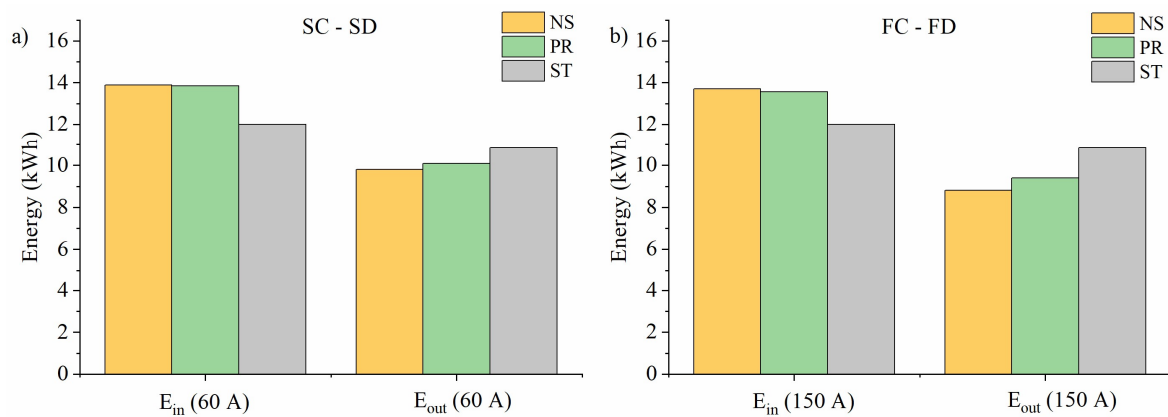


Fig. 36. Energy required for battery charge and delivered to the grid during discharge: a) SC-SD mode; b) FC-FD mode; NS – numerical simulations; PR – proposed approach; ST – standard approach.

In addition to the estimation of energy amounts, it is also very important to look at the battery usage protocol (the schedule how the battery is used) that includes the loading power (which is assumed to be averaged over time) and corresponding operation time. The usage protocol is used in practical applications for planning of preliminary battery schedule and for estimation of battery performance in long-term operation. Fig. 37 presents the usage protocols for slow and fast operation modes considered above. As can be seen, the usage

profile obtained in the framework of the proposed simplified approach (blue line) has a good agreement with the profile based on the data from detailed numerical simulations (black dashed line) (average error less than 3%). On the contrary, the standard approach with constant efficiencies (red line) leads to significant error and can overestimate battery operation time up to 1 hour. Such error can be critical for stable operation of the grid, as according to this profile, the battery should provide the power to the grid, while in reality, it is not able to fulfill this requirement. As a result, the additional power sources need to be applied at this time in order to support the given loading profile. It should be noted as well that this error has an accumulative effect and will increase with the number of cycles leading to the drastic difference in the real and expected battery operation profile, that can be either dangerous for the battery or for the entire grid.

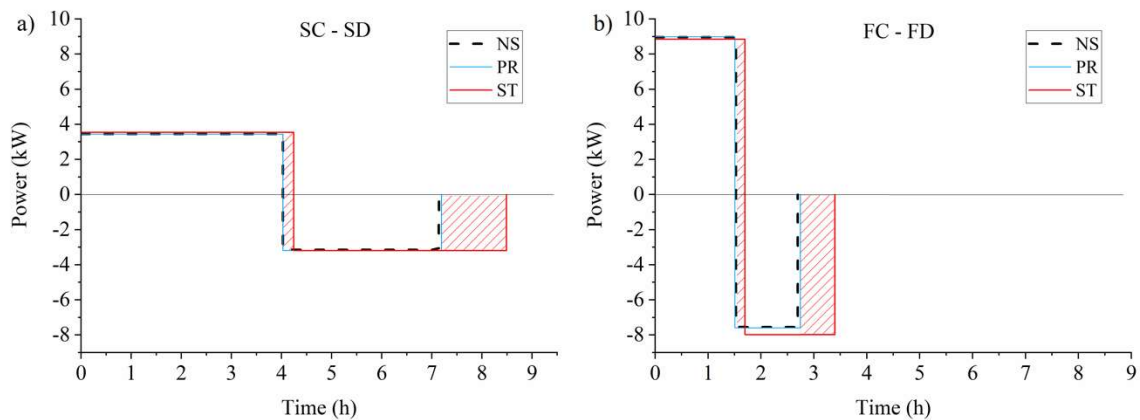


Fig. 37. Simplified battery usage profiles in different operation modes: a) slow mode; b) fast mode; NS – numerical simulations; PR – proposed approach; ST – standard approach.

After that, the combination of slow and fast modes in charge and discharge was considered: slow charge – fast discharge (SC-FD) and fast charge – slow discharge (FC-SD). As in the previous case, the battery was charged with one current starting from initial SOC of 10% till the upper cut-off voltage of 64 V. After that, the battery was discharged with the other current till the lowest cut-off voltage of 40 V. The corresponding loading profiles and voltage curves are presented on Fig. 38.

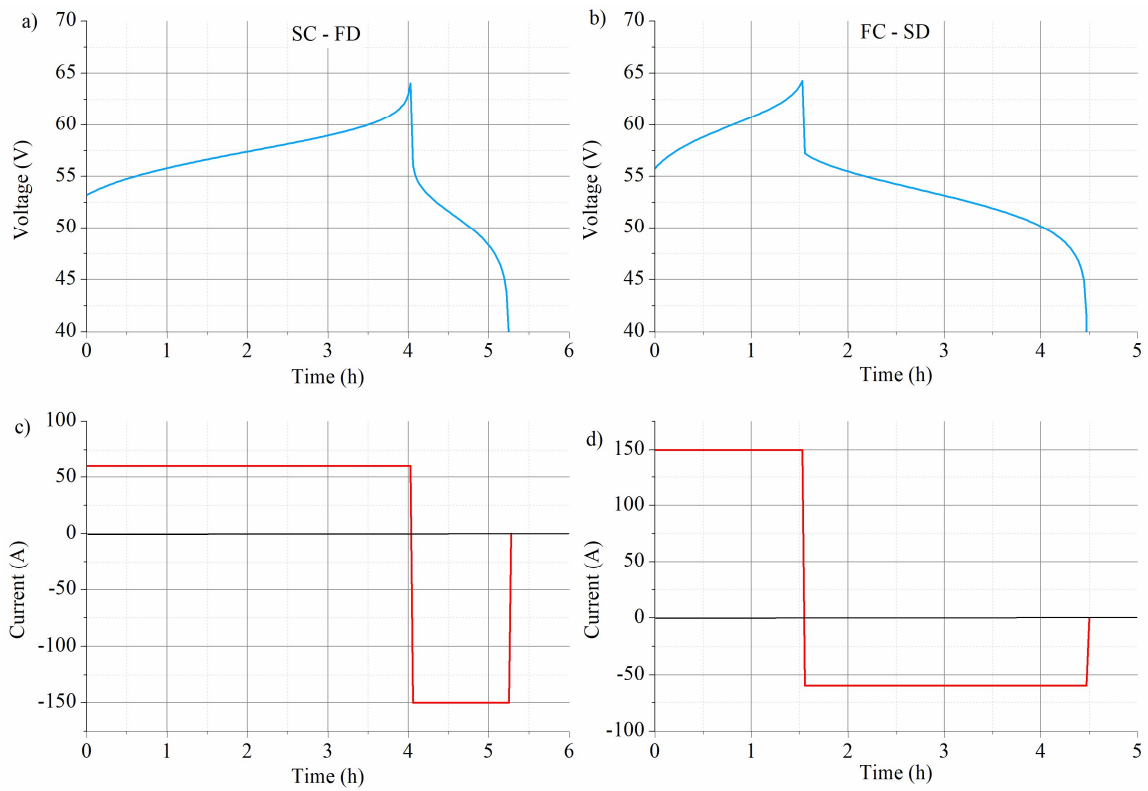


Fig. 38. Current profiles and voltage curves for SC-FD and FC-SD operation modes: a) voltage profile SC-FD mode; b) voltage profile FC-SD mode; c) loading current SC-FD mode; d) loading current FC-SD mode.

The considered modes can be interesting for some practical tasks. The first combination (SC-FD) has a practical value for the situation when the grid cannot provide high power for battery operation (slow charge mode), but afterward, while discharging, the battery will need to compensate significant power dispatch in the grid (fast discharge mode). The second combination (FC-SD) can be considered for cases when the battery can be charged fast (e.g., due to sudden fluctuation in the power generation from the renewables) and need to be used for longer electricity supply with low power.

The comparison of energy amounts (Fig. 39) showed that the proposed approach allows estimating battery operation more accurately than in the cases considered before. That is likely due to a smaller error for smaller currents in the proposed approach, and as far as here we considered the combination of high and low currents, the integral error is smaller than in the previous cases when the currents in charge and discharge were equal. In addition, the standard approach demonstrated the same significant error for both cases that can achieve nearly 20%.

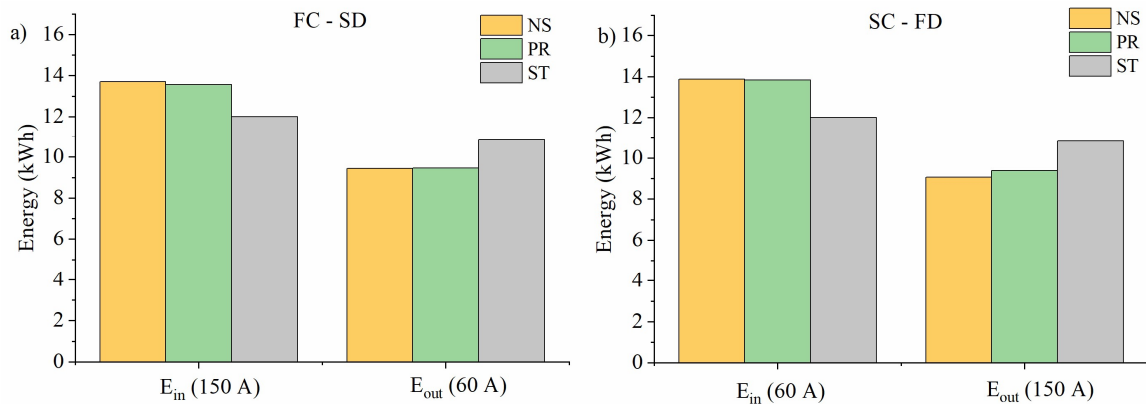


Fig. 39. Energy required for battery charge and delivered to the grid during discharge: a) FC-SD mode; b) SC-FD mode; NS – numerical simulations; PR – proposed approach; ST – standard approach.

The battery usage profiles for the considered cases are shown in Fig. 40. As can be seen, the standard approach (red line) demonstrated the same error as in the previous cases leading to a mistaken estimation of battery operation time around one hour. At the same time, the proposed approach (blue line) showed a good agreement with numerical simulations (black dashed line) with an average error of less than 3%. As a result, the proposed approach can be used for the development of usage profiles for real VRFB systems working at different operating conditions.

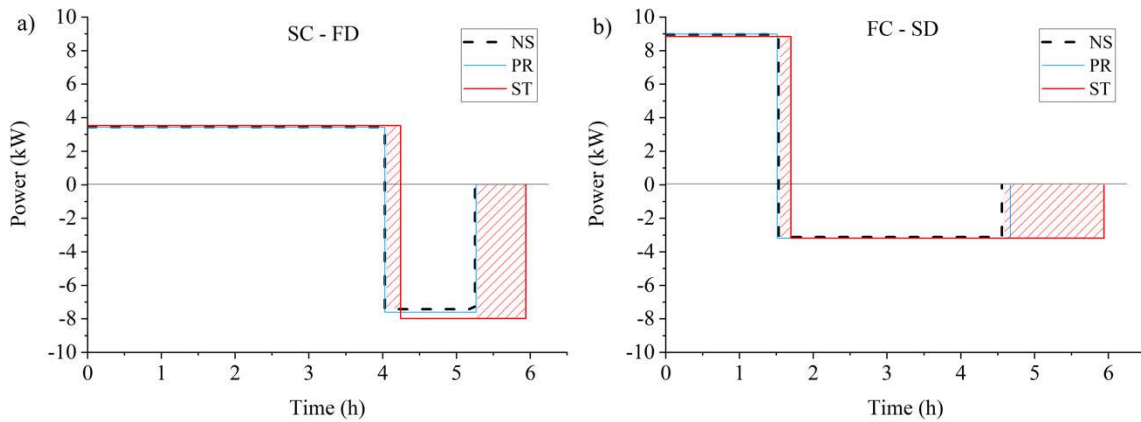


Fig. 40. Simplified battery usage profiles in mixed operation modes: a) SC-FC mode; b) FC-SD mode; NS – numerical simulations; PR – proposed approach; ST – standard approach.

4.7 Conclusions

The development of practical tools for estimation of Vanadium Redox Flow Battery (VRFB) performance is fundamental for the determination of design parameters (membrane area and volume of the tanks) and proper operation constrains (operation time and power) that could ensure reliable operation of these systems. In this study, we have proposed a new method, which is able to relate the key properties of real VRFB systems, such as rated power, energy capacity and operation time to their ideal characteristics determined from the geometrical size of the system. Such an approach allows estimating VRFB performance in charging and discharging operation separately that brings an added value for the understanding of internal physical processes and their impact on the aggregated VRFB characteristics.

First, the analysis of voltage and coulombic efficiencies in charging and discharging operation depending on different loading currents is performed basing on the detailed numerical simulations of the considered VRFB system. The main findings can be summarized as the following:

(1) The voltage efficiency declines linearly with the increase of current density both in charging and discharging operation. Such behavior can be addressed to the fact that in the considered range of current densities ($40 - 100 \text{ mA cm}^{-2}$) the internal processes intensify linearly with an increase of current, leading to linear growth of corresponding losses. In the charge mode, the voltage losses are mainly presented by the ohmic overvoltages, while in discharge mode, the crossover also starts to affect the battery voltage

resulting in lower voltage efficiency. In addition, it should be noted that the voltage efficiency in discharge is lower than in charge, which is attributed to the asymmetric behavior of crossover, which is more intensive in discharge mode that was explained in Sec. 4.6.1.

(2) The useable battery capacity is smaller than the capacity determined by the amount of chemicals contained in the tanks (maximum theoretical capacity) and this deviation becomes more pronounced for high current densities. Our investigations revealed that the observed capacity decay is a result of the joint effect of mass transport limitations on the electrodes and transport of vanadium ions across the cell's membrane. Moreover, the charging coulombic efficiency showed nonlinear behavior with an increase of current density that can be addressed to the impact of concentration losses, which have a larger share in charge mode. In addition, the results showed that discharge mode is characterized by stronger capacity decay, which showed negligible sensitivity to current density presenting around 30% of the maximum theoretical capacity for all considered current densities. Such behavior is mainly attributed to the intensification of net crossover fluxes in discharging operation.

After that, the simplified methodology is proposed, characterizing the efficiencies as a function of current density. The approach was validated considering the extreme cases of battery operation strategies related to slow and fast modes. The results showed that the proposed methodology has a good agreement with the results of detailed numerical simulations (with averaged error less than 3% for averaged power and time and 6% for

stored energy). Thus, the proposed methodology can be used as a simple tool for correct estimation of battery power and operation time in grid-scale simulations. It can be especially important for the development of accurate battery usage protocols that allow avoiding over/underestimation of rated power/capacity and operation time of the VRFB system at real operating conditions, that in turn can prevent serious failures in the entire grid (in case of micro-grid application) or fines for system operator (in case of grid-connected storage application).

Chapter 5. Control of electrolyte flow rate

5.1 Introduction

One of the key components of VRFB is the battery management system (BMS), which monitors and controls such parameters as loading current, battery temperature and electrolyte flow rate in order to ensure stable battery operation with high efficiency and low degradation [19,113]. The connection of the battery to the grid with the application of BMS is shown in Fig. 41, where the BMS is connected with the battery and the power electronic converter that transforms voltage to the required range and current from the AC to DC. At the same time, the BMS receives information about battery voltage, the instant temperature of the stack and battery SOC. Basing on that and considering the requirements from the grid, the BMS forms the control actions that ensure stable battery operation:

- the current is determined by the power electronic converter, depending on the battery state of charge (SOC) and required power for the grid;
- the battery temperature is controlled by a thermal management unit, which keeps the battery in an admissible range of temperatures [61];
- the flow rate controller adjusts the flow rate of electrolyte in the VRFB cell depending on different operating conditions [114].

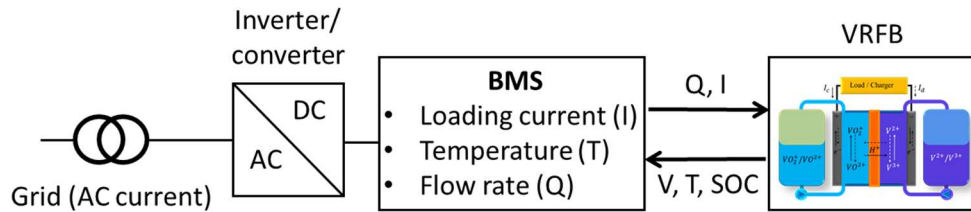


Fig. 41. Grid connection of the battery. AC and DC are alternative and direct current, respectively; BMS – the battery management system; SOC – the battery state of charge.

Although the control of current and temperature is common for all types of batteries, the flow rate control is one of the unique features of VRFB technology that gives additional benefits for its application (in comparison to conventional batteries such as Li-ion). A properly designed flow rate control system reduces internal losses related to pumps' consumption [115] while increasing battery lifetime due to lower pressure gradients in the hydraulic circuit [99]. Moreover, to assure stable battery operation, the controllers should be fast enough to work in real-time mode with good damping of oscillations caused by dynamically changing loading conditions. Fig. 42 shows an example of the battery response for a sudden change of the loading current. As it can be seen, at the maximum flow rate, the battery is able to track the changes in the load, while at the minimum flow rate, it was not able to follow the changes reaching the lower cutoff voltage, and thus, the battery was terminated soon after the current jump. The reason for such behavior will be discussed in the next sections, while here we would like to highlight the importance of the flow rate regulation.

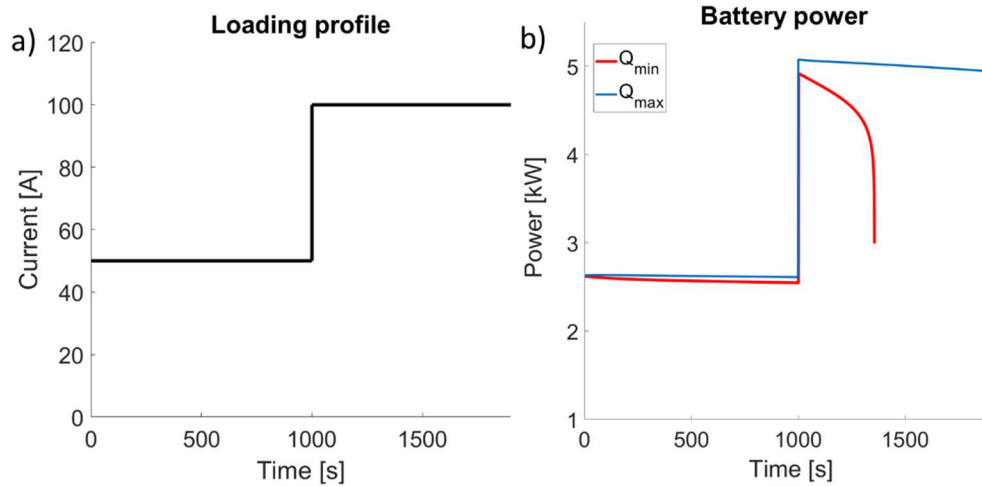


Fig. 42. The battery response for a sudden change of the loading current: a) loading current profile; b) battery power at maximum (blue line) and minimum (red line) flow rates.

A number of studies devoted to different strategies of flow rate control have been published during the last decade. The simplest control systems are based on open-loop approaches and directly regulate the flow rate utilizing empirical laws. Some open-loop controllers use pulsating flow rate by switching on/off the pumps, and thus, reducing the pumping energy consumption as compared to the constant flow rate [116]. Nevertheless, these discontinuous control approaches have limitations, as frequent switches do not guarantee efficient energy management but speed up the equipment aging and battery degradation. In addition, the determination of proper periods for on/off modes is getting complicated at suddenly changing loading conditions. Thus, flow rate regulation within a continuous open-loop control framework can ensure a more reliable and efficient battery operation during sudden oscillations of the loading current. More advanced control strategies utilize the Faraday's law of electrolysis. Within these strategies, the controller

continuously varies the flow rate providing the balance between feeding and consumed ions (equilibrium state) in the cell [43,117]. The notion of a specific constant/varying gain referred to flow factor was used for further improvement of the approach [87,118,119]. Another extension proposed in [120] modified the Faraday's law with power-law approximation dependent on the SOC. The open-loop control approaches have some advantages and limitations. On the one hand, they are very simple, and thus, can be applied for real-time regulation of flow rate. On the other hand, the open-loop systems are not robust in practical applications as they adjust the flow rate using some empirical laws without consideration of the battery output. Moreover, battery parameters are changing during long-term operation due to the degradation of internal components that should be taken into account for proper control.

Some more advanced control strategies utilize optimization techniques for computation of flow rate that would ensure the maximization of some desired battery parameters like efficiency, capacity, operation time [121–127]. Although these approaches look more beneficial than pulsating flow rate/flow factor strategies, they require time-consuming computations and therefore are not applicable in real-time control tools. In addition, the transient battery performance (magnitudes/durations of overshoots and oscillatory behavior) under time-varying loads is out of the scope within such approaches. On the contrary, the implementation of closed-loop control strategies can avoid the mentioned drawbacks due to the presence of a controller that takes into account measurements of current battery outputs and minimizes the tracking error.

To the best of our knowledge, only a few works have studied feedback approaches for electrolyte flow rate control. The paper [97] reported simple nonlinear feedback based on switching the pumps from minimum to maximum flow rate at some certain voltage. However, such an approach has the same drawbacks as discontinuous control methods discussed in the beginning. The authors of another work [67] proposed a classical closed-loop control approach using a proportional and integral (PI) controller. The designed controller adjusts the electrolyte flow rate in order to ensure good electrochemical conversion in the cell. This strategy was proven to be robust against sudden changes in load, tracking a desired reference trajectory with high accuracy. However, the straightforward application of this approach in practice is obstructing, as long as accurate measurements of conversion coefficient are not feasible in real VRFB systems. Moreover, the real-time computation of the proposed reference trajectory requires significant computational power. Some results based on control fuzzy logic ensuring the good dynamic performance of the battery with fast response, were studied in [98]. Nevertheless, the developed controller has significant computational complexity and may require the application of sophisticated and expensive hardware.

The main features of the control strategies mentioned above are summarized in table 8.

Table 8. Control strategies for flow rate regulation.

Paper	Control approach	Effect
[116]	Pulsating flow rate regulation (periodical switch on/off pumps)	Reduction of pumps' consumption by two times in comparison to constant flow rate
[97]	Switching the pumps from minimum to maximum flow rates at some certain voltage	Increase of total energy efficiency by 8% in comparison to the fixed high flow rate
[43]	Faraday's law of electrolysis with fixed flow factor	Reduction of pumps' consumption by two times in comparison to constant flow rate
[118]	Faraday's law of electrolysis with variable flow factor	Increase of total energy efficiency by 8% in comparison to the fixed flow factor
[120]	Approximation of Faraday's law by power law function of SOC	Increase of total energy efficiency by 3.5% in comparison to the constant flow rate
[121]	Optimization of battery operation by maximizing the battery power while minimizing pumps' consumption	Increase of total energy efficiency by 10% in comparison to the constant flow rate
[122]	Combination of losses minimization with the flow factor strategy	High system energy efficiency (more than 87%) at dynamic loading conditions
[123]	Combination of losses minimization with the flow factor strategy	Reduction of the VRFB operation cost by 11 – 20% in comparison to non-optimized battery operation
[124]	Minimization of total energy losses	Increase of the battery capacity up to 5.4% in comparison to flow factor strategy
[125]	Minimization of total energy losses	Improvement of the system energy efficiency up to 34% as compared to constant flow rate

[128]	Model predictive control with application of neural networks	Slight improvement of voltage battery efficiency (around 1%) in comparison to constant flow rate battery operation
[126]	Minimization of total energy losses in charging process	Increase of system energy efficiency up to 5 % in comparison to flow factor strategy
[67]	PI controller with gain scheduling	Good battery performance at dynamic loading conditions with constant conversion in the cell
[98]	Fuzzy logic controller	Good dynamic battery performance with fast response in different modes of operation (power and energy savings modes)

It should also be noted that the papers considered above are mainly focused on the control of mass transfer in the cell. However, the performance of VRFB systems is also notably affected by the mass transport processes in the porous membrane caused by the crossover (transfer of vanadium ions across the membrane) [44]. The crossover implies an imbalance of electrolytes in the negative and positive sides, reducing usable battery capacity. Thus, in addition to the mass transfer control in the cell, such imbalance also needs to be detected and periodically corrected by a specific class of electrolyte control strategies. These strategies are aimed at recovering initial capacity using electrolytes' rebalancing [129] with periodic remixing [130] or hydraulic shunt [131]. Therefore, such complex nonlinear dynamics of VRFB imply multi-stage control problems to be systematically identified, analyzed, and resolved in a consistent fashion for the design of efficient BMS.

In this chapter, we propose a novel strategy for flow rate control in VRFB systems. The contribution of our work is twofold. First, we introduce a hierarchical classification of tasks related to flow rate regulation. Such methodology allows ranking different control problems according to their nature and characteristic time of underlying VRBF processes. Second, we design a closed-loop control system that ensures stable and robust battery operation at drastically changing loading conditions and improves the existing feedback control approaches [67]. The cornerstone of our method is the algorithm for the determination of optimal reference OCV that significantly reduces computational complexity and provides necessary performance in terms of control actions, equipment aging and energy savings.

5.2 Timescales and three-stage flow rate control

Each component of the VRFB system can be characterized by different time constants (or characteristic times) of the processes taking place in the corresponding domain (tanks, pumps or cell). For example, the transport of vanadium ions across the membrane is a slow process and plays a significant role only after several cycles, while the mass transport processes within chemical conversion in the cell are important during a single cycle. Finally, the processes related to hydraulic inertia of the system and transport of ions in the pipes are getting important during transient periods only at drastic changes of loading conditions. Based on the characteristic time of the mass transport processes, each of them can be controlled independently by local feedback controllers. Thus, a three-

stage control system can be proposed in order to keep the desired battery performance within each timescale (Table 9). The general control hierarchy may look as follows:

The first stage deals with the fastest processes in the system (hydraulic inertia, transport delay). This can be performed by means of a dynamic pump controller, ensuring the required behavior of pumps;

The second stage is related to control of chemical conversion in the cell in cycling operation and can be based on the Faraday's law/real-time optimization/feedback control;

The upper level controls the slowest processes related to mass transport in the membrane. The corresponding control can be based on the periodical rebalancing of electrolyte in the tanks.

Table 9. Three-stage control hierarchy.

Timescale	Physical processes	Control level	Battery component
10 – 100 cycles	Electrolyte imbalance in the tanks due to crossover	3 rd level of control	Tanks/Cells
1 cycle (1000 s)	Mass-transport in the cell during cycling operation	2 nd level of control	Cells/Pipes
ms – s	Transport delay in the pipes and inertia of the pumps	1 st level of control	Pumps/Pipes

This hierarchy shows that all hydraulic related processes in the VRFB system live within their own timescales. Thus, the entire control system can be decomposed into three independent parts related to the corresponding control stages. Such decomposition and multistage control techniques have many benefits, including [132]:

- possibility of using different types of controllers for each local problem;
- reduced computational requirements;
- increased robustness, security and reliability.

Among the control levels presented in Table 9, the second one is of special practical interest. A single cycle operation can be considered as a unit (or elementary) time interval that repeats during long-term battery operation. In this study, we mainly focus on the 2nd level of control, neglecting the effects of transport delays, hydraulic inertia of the system and crossover. Such an assumption significantly simplifies the mathematical model, while the neglected phenomena can be analyzed and controlled within the corresponding levels of three-stage hierarchy.

5.3 Controller design

The block diagram of the proposed closed-loop system for flow rate regulation is presented in Fig. 43. It should be noted that in our simulations, the block **Loading profile** is represented by a test signal defined in advance (current in charge/discharge mode), while in real applications, the loading current I is formed by the power electronic converter in order fulfill requirements of the external grid. The **Reference** block transforms the desired voltage into a function of time (the method to obtain the reference trajectory will be

discussed in Sec. 5.5). The **Battery model** represents battery dynamics. The **Controller** consists of proportional and integral (PI), and feedforward (if needed) components with three adjustable coefficients.

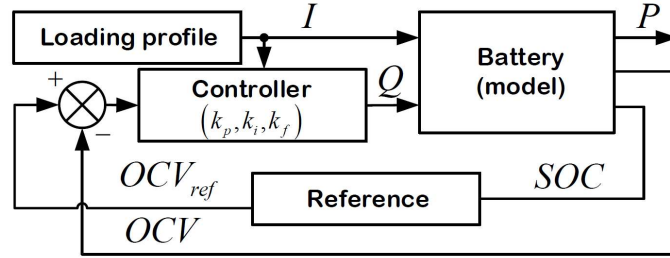


Fig. 43. Flowrate control system with proportional-and-integral (PI) and feedforward (FF) controllers.

The cornerstone of our approach is the algorithm for the determination of the desired OCV (see Sec. 3). Such a reference signal provides near-optimal performance at a lower cost in terms of the flow rate and pumps energy consumption. One can note that the original bilinear model of the VRFB system (see Sec. 3.3) can be linearized around operating points, which correspond to optimal flow rates [67]. The simplified linear model of the open-loop system has the form of two first-order differential equations. Therefore, the use of a conventional PI controller supplemented by a feedforward gain is enough to remove steady-state error and reach the desired performance. Relatively easy tuning of the controller coefficients and its simplicity are the main advantages of this control strategy along with good performance. Thus, the control law has the following form:

$$Q(t) = k_p e(t) + k_i \int e(\tau) d\tau + k_f I(t), \quad (50)$$

where $e(t) = OCV_{ref}(t) - OCV(t, k_p, k_i, k_f)$ is the error between the desired and real voltages and k_p, k_i, k_f are the adjustable parameters of the controller.

Suppose that the time interval $[0, \tau]$ corresponds to the duration of the test loading profile. Then, based on this profile, we can minimize the integral square error to find the coefficients of the controller:

$$\int_0^{\tau} (OCV_{ref}(t) - OCV(t, k_p, k_i, k_f))^2 dt \rightarrow \min_{k_p, k_i, k_f} . \quad (51)$$

Due to the low dimensionality of the parameter space, this task can be solved by the application of Monte Carlo random sampling and direct computation of the objective function.

5.4 Mathematical model

The concentrations in the cell are obtained from a solution of mass balance equations in the cells and in the tanks introduced in Chapter 3 and further extended in Chapter 4 for simulation of the stack. The model has been simplified by neglecting the crossover term. Such simplification can be applied within the three-stage control system proposed in Sec. 2. In the absence of crossover, there is no imbalance in vanadium concentrations and the SOCs of the negative and positive sides are equal, while the system of mass balance equations can be significantly simplified and written as follows:

$$\frac{d\vec{x}}{dt} = \underline{Q}\mathbf{A}\vec{x} + I\vec{S}, \quad (52)$$

where

$$\vec{x} = (x_1, x_2, x_3, x_4, x_5, x_6, x_7, x_8)^T = (c_2^{tk}, c_3^{tk}, c_4^{tk}, c_5^{tk}, c_2^{ce}, c_3^{ce}, c_4^{ce}, c_5^{ce})^T, \quad (53)$$

$$\vec{S} = \left(0, 0, 0, 0, \frac{1}{FV_{ce}}, -\frac{1}{FV_{ce}}, -\frac{1}{FV_{ce}}, \frac{1}{FV_{ce}} \right)^T, \quad (54)$$

$$\mathbf{A} = \begin{pmatrix} -\theta & 0 & 0 & 0 & \theta & 0 & 0 & 0 \\ 0 & -\theta & 0 & 0 & 0 & \theta & 0 & 0 \\ 0 & 0 & -\theta & 0 & 0 & 0 & \theta & 0 \\ 0 & 0 & 0 & -\theta & 0 & 0 & 0 & \theta \\ \gamma & 0 & 0 & 0 & -\gamma & 0 & 0 & 0 \\ 0 & \gamma & 0 & 0 & 0 & -\gamma & 0 & 0 \\ 0 & 0 & \gamma & 0 & 0 & 0 & -\gamma & 0 \\ 0 & 0 & 0 & \gamma & 0 & 0 & 0 & -\gamma \end{pmatrix} \quad (55)$$

Here $\mathbf{A} \in \mathbb{R}^{8 \times 8}$ is the matrix related to convection between the cell and the tank,

$$\theta = 1 / V_{tk} \text{ and } \gamma = 1 / n_{ce} V_{ce}.$$

The battery power is calculated as a product of stack voltage and instant loading current:

$$P_{bat} = U_{bat} I. \quad (56)$$

Since we have neglected the crossover, the state of charge of the electrolyte in the tanks is assumed to be equal and is given by:

$$SOC_{tk} = \frac{c_2^{tk}}{c_2^{tk} + c_3^{tk}} = \frac{c_5^{tk}}{c_4^{tk} + c_5^{tk}}. \quad (57)$$

Simulated case study

In this study, we consider 5 kW/15 kWh VRFB system with technical specifications reported in Chapter 4. The system is based on the battery stack comprised by 40 cells with

Nafion 115 membrane (area of 1500 cm²), which separates the half-cells. The tanks contain 200 L of electrolyte (each) composed of 2M of vanadium and 5M of sulphuric acid. The electrolytes are pumped through the cells with a volumetric flow rate in the range of 0.05 – 1.0 L s⁻¹. The averaged cell resistivity is assumed to be 2 Ω cm² and constant during battery operation. The detailed stack parameters are listed in Table 6 (Sec. 4.4). It should be noted that a proper selection of membranes and their pre-treatment can notably affect the energy efficiency and electrolyte utilization of the VRFB system [133–135], while we have taken the standard parameters for Nafion 115, as it is the most well-studied membrane in the literature. In addition, the considered VRFB system is one of the possible demonstrative examples, however, our approach can also be applied to other systems with different electrolyte compositions, as far as it is based on the general physical equations that describe processes inside the VRFB system.

The simulations are performed by using in-house software developed in MATLAB environment. The differential equations have been solved numerically using MATLAB ODE solver. The developed approach has low computational complexity and demonstrates a modest computational time (several seconds for simulation of 1-hour physical operation), and thus, can be suitable for application in real-time closed-loop control systems. The battery operation is simulated in the wide range of operating loading currents (20 – 180 A). The upper and lower cut-off voltages are set as 64 V and 40 V, which corresponds to ~90% and ~10% of SOC, respectively.

5.5 Optimal OCV and the reference trajectory

First, we have performed parametric sweep calculations varying the flow rate with constant step 0.05 L s^{-1} from minimum to maximum values at fixed current density. The results have revealed the convergence of OCV curves with the increase of flow rate (Fig. 44). Similar results were also observed experimentally in [119]. For the sake of simplicity, we show the results of calculations only for one loading current ($I = 100 \text{ A}$) while similar results were obtained for all considered currents. As it can be observed, the flow rate notably affects the battery voltage as along with the available capacity that can be used during battery operation. The maximum flow rate provides good battery performance with the utilization of nearly the whole battery capacity (black dashed line); on the contrary, operation at a minimum flow rate (blue line) results in significantly worse performance with a rather small capacity utilization (less than 60% of the available capacity). In fact, the battery can operate at a maximum flow rate that can guarantee good mass transfer in the cell at all considered loading currents. However, a high flow rate induces high pressure drops in the stack and pipes that increases risks of leakages and also leads to higher deterioration of internal components in the cell, thus significantly reducing battery lifetime. In addition, as it will be shown later, the maximum flow rate in many cases is notably higher than the optimal value that can ensure the same or nearly the same battery performance, and therefore, such strategy also results in additional energy losses. Thus, the determination of optimal flowrates that could assure proper battery performance is very important for efficient VRFB operation.

The parametric sweep calculations also have shown that the maximum difference between the OCV curves is observed at the highest SOC (SOC = 90%) and the lowest SOC (SOC = 10%) for charge and discharge, respectively, as in these states, the system is the most sensitive to the flow rate due to low concentration of active species. Nevertheless, for any loading current, it is possible to find a value of flow rate, after which the further increase does not significantly change the battery OCV. For example, for considered current ($I = 100$ A), the maximum difference between OCVs for corresponding flow rates of 0.25 L s^{-1} (red dashed line) and 1.0 L s^{-1} (black dashed line) is only around 2% at SOC = 90% (for charge) and SOC = 10% (for discharge).

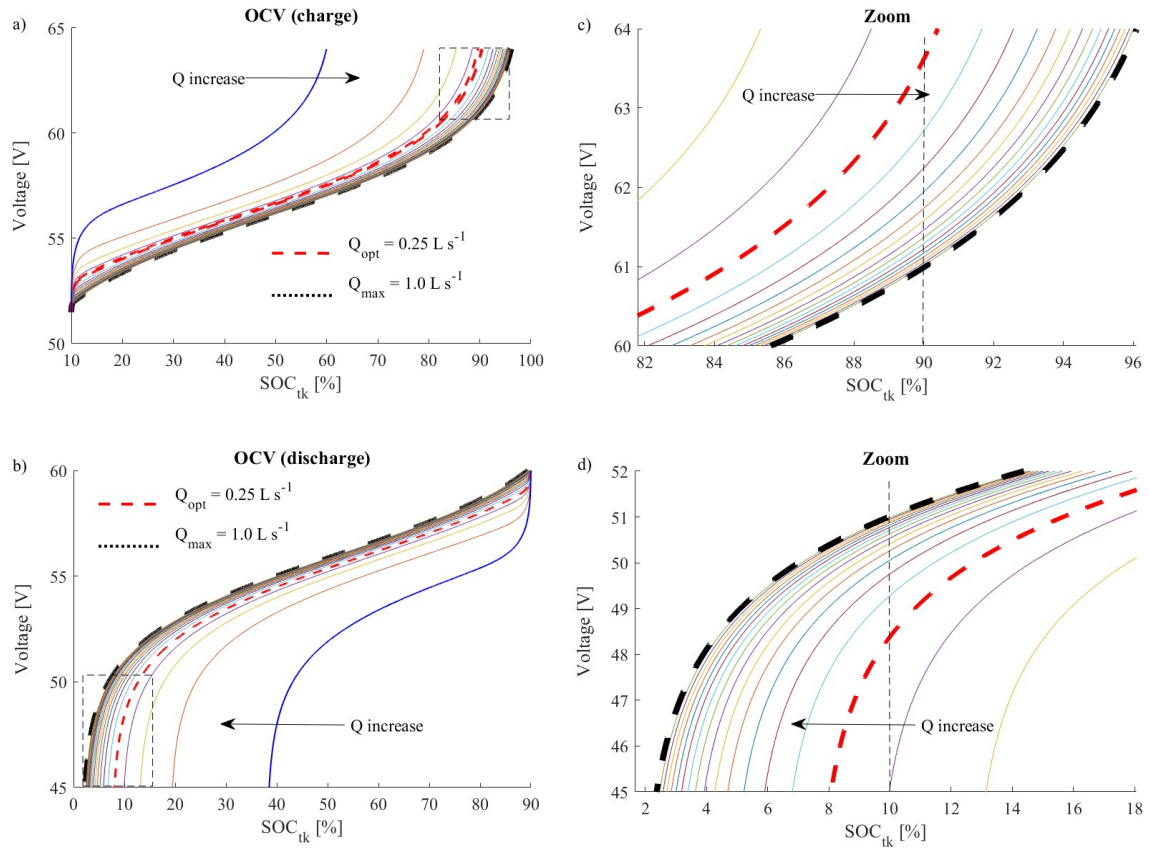


Fig. 44. Parametric sweep calculations for varied flow rate at loading current $I = 100$ A, a) charge process, b) discharge process, c) zoom (charge), d) zoom (discharge); black dashed line – $Q_{max} = 1.0 \text{ L s}^{-1}$; blue line – $Q_{min} = 0.5 \text{ L s}^{-1}$; red dashed line – $Q_{opt} = 0.25 \text{ L s}^{-1}$;

To analyze the effect of flow rate on the OCV behavior, we have considered dimensionless parameter ξ calculated as the difference between the nearest OCVs at these SOC with respect to the OCV at maximum flow rate:

$$\xi = \frac{OCV(Q_{n+1}) - OCV(Q_n)}{OCV(Q_{max})} \quad (58)$$

The results (Fig. 45) show when the parameter ξ reaches the value of 2%, further increase of electrolyte flow rate does not have a notable effect on OCV. It also should be noticed, the relative OCV difference has been lower than 2% at the same flow rate for the same currents both in charge and in discharge. As a result, we propose the following strategy for the determination of the optimal flow rate:

- parametric sweep calculations with varied flow rate at fixed loading current;
- the lowest flow rate that ensures less than 2% difference between the nearest OCVs with respect to maximum OCV at SOC = 90% (for a charge) and SOC = 10% (for discharge) can be chosen as optimal (marked by red stars on Fig. 43b).

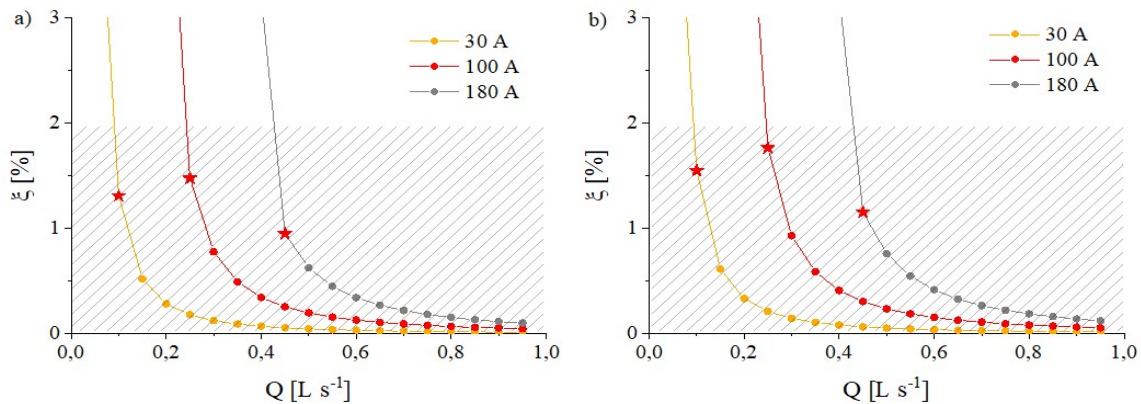


Fig. 45. Sensitivity of battery OCV to the change of flow rate at fixed loading current, a) charge (SOC = 90%), b) discharge (SOC = 10%).

The application of the proposed strategy allows obtaining the OCV close to maximum flow rate while requiring significantly lower flow rates for all loading currents in a range. Moreover, this strategy can be easily used for the determination of optimal flow

rates in real systems where the first step can be performed by direct experimental measurements of charge-discharge curves at different flow rates. The obtained OCV has similar behavior both in charge and in discharge for all considered currents. As a result, we have used this OCV as a reference for the development of the closed-loop control system.

Furthermore, the effect of flow rate on the main energy performance indicators of VRFB (as Voltage Efficiency (VE), Energy Efficiency (EE) and Electrolyte Utilization (EU)) is analyzed (Table 10). For this reason, we consider a single charge-discharge cycle with fixed loading current for three different values (30 A, 90 A, 150 A) and three flow rates ($Q_{min} = 0.05 \text{ L s}^{-1}$; $Q_{max} = 1.0 \text{ L s}^{-1}$; Q_{opt} = the flow rate determined within the strategy described above).

The VE is calculated as a ratio of the average voltage in discharge to the average battery voltage in charge (here the average value is calculated over the time of the corresponding process: τ_{dis} and τ_{ch} respectively):

$$VE = \frac{\langle U_{bat} \rangle_{dis}}{\langle U_{bat} \rangle_{ch}} = \frac{\frac{\int U_{bat} dt}{\tau_{dis}}}{\frac{\int U_{bat} dt}{\tau_{ch}}} \quad (59)$$

The EE is calculated as the ratio of the total energy released during discharge to the total energy consumed during charge, taking into account pumps' consumption:

$$EE = \frac{\int_{\tau_{dis}} (IU_{bat} - P_{pump}) dt}{\int_{\tau_{ch}} (IU_{bat} + P_{pump}) dt} \quad (60)$$

To determine pumps' power consumption, we take into account that the VRFB system considered in this study is based on the cells with flow-through topology, where electrolyte soaks through the porous electrode. It was shown in [136] that for such configurations, the pressure drop in the porous electrodes makes up the major part (around 70%) of pressure losses in the entire VRFB system. Thus, we have estimated the total pressure drop as the following:

$$\Delta p_{tot} \approx 1.5\Delta p_{el} \quad (61)$$

The flow regimes in the cell correspond to the low Reynolds numbers ($Re \sim 1$) [125], thus the pressure drop in the porous electrode can be estimated with the application of Darcy's law [43]:

$$\Delta p_{el} = \frac{\mu L Q}{\kappa A_{ed}} \quad (62)$$

Finally, the pumps' power consumption can be estimated as [43]:

$$P_{pump} = \frac{\Delta p_{tot} Q}{\varepsilon_{pump}} \quad (63)$$

Another important indicator is related to the estimation of Electrolyte Utilization (EU) during battery operation. The EU is calculated as a ratio of the sum of battery capacity stored in charge mode and released in discharge mode to the theoretical one:

$$EU = \frac{\int_{\tau_{ch}} Idt + \int_{\tau_{dis}} Idt}{2\kappa_{th}} = \frac{n_{cell} I (\tau_{ch} + \tau_{dis})}{2c_0 F V_{tk}} \quad (64)$$

Table 10. Effect of different flow rate strategies on the main VRFB efficiency indicators.

Current, A	30			90			150		
Eff. indicator	<i>VE</i>	<i>EE</i>	<i>EU</i>	<i>VE</i>	<i>EE</i>	<i>EU</i>	<i>VE</i>	<i>EE</i>	<i>EU</i>
Q_{min}	0.931	0.945	0.841	0.835	0.574	0.481	0.782	0.183	0.169
Q_{max}	0.968	0.636	0.872	0.908	0.791	0.895	0.850	0.782	0.812
Q_{opt}	0.933	0.940	0.875	0.881	0.861	0.824	0.830	0.790	0.742

As it can be seen from Table 10, the minimum flow rate provides good battery operation only at low current (30A) with high electrolyte utilization (84% of total theoretical capacity). Nevertheless, at higher currents, it does not allow to use the full capacity of the battery providing only 48% and 17% of electrolyte utilization for 90 A and 150 A, respectively. The maximum flow rate ensures more than 80% of capacity for all considered currents, but it results in low total energy efficiency that can be specially noted at low currents when the battery efficiency was around 64% due to the high energy consumption of the pumps. The proposed flow rate strategy (Q_{opt}) provides slightly lower voltage efficiency and lower electrolyte utilization as compared to the maximum flow rate while ensuring higher total energy efficiency (more than 79%) for all considered currents.

5.6 Results and discussion

5.6.1 Short-term operation and transient battery behavior

First, the investigation of transient battery behavior at dynamic loading conditions is performed both in charge (Fig. 46) and discharge (Fig. 47) modes. Here we consider worst-case disturbances affecting battery operation, namely sudden switches between the minimum and the maximum currents (Fig. 46a and Fig. 47a). The drastic changes in loading current should also lead to similar changes in the electrolyte flow rate since it should ensure equilibrium between production and consumption of ions. The results show that, in general, the proposed control strategy assures good damping of the load changes. However, the flow rate exhibits some transient behavior with smooth exponential switching between the regimes (Fig. 46b and Fig. 47b). This can be attributed to the internal hydraulic inertia of the entire VRFB system related to the volumetric transport of ions in the tanks and cells. Nevertheless, the designed controller is able to track reference trajectory with high accuracy, the maximum deviations between the calculated voltage (orange line) and reference one (red dashed line) are observed only at the transient points and present less than 0.2% for the charge (Fig. 46c) and 0.15% for discharge (Fig. 47c).

As a next step, we consider the application of feedforward gain using the approach proposed in [67]. The feedforward controller eliminates the effects of changes in current, thus keeping the system invariant regarding all disturbances. Finally, the application of feedforward gain results in faster switches of the flow rate (blue line) as depicted in Fig. 46b and 47b. The tracking of reference voltage trajectory with and without feedforward

gain is presented in Fig. 46c and 47c. The average error between the reference (red dashed line) and calculated (blue line) voltages is shown to be less than 0.0005 %. Therefore, in further simulations, we used a control system with feedforward gain.

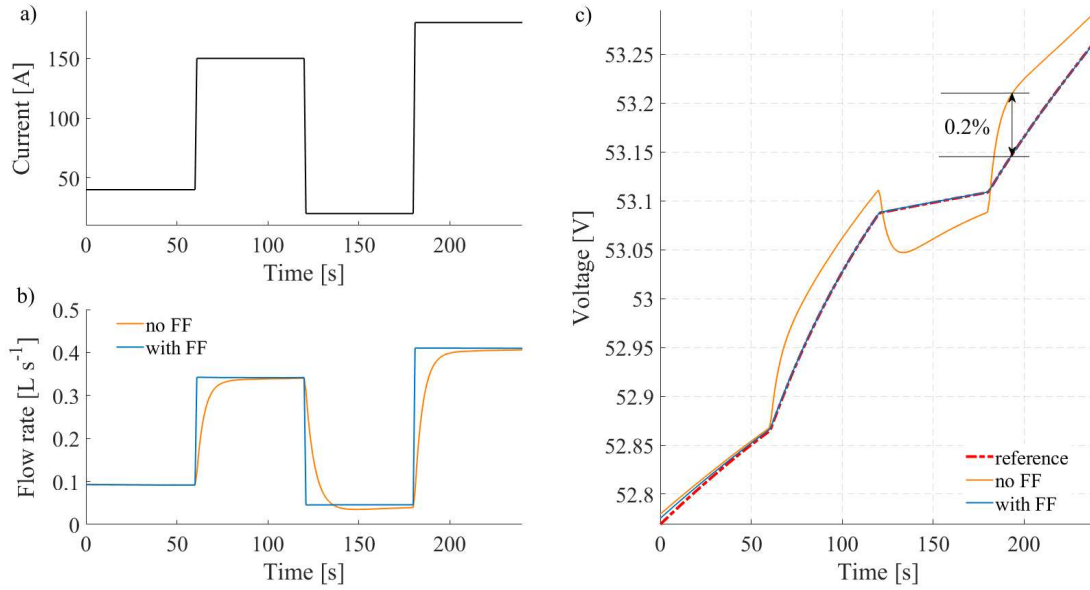


Fig. 46. Battery transient behavior in short-term charging operation: a) loading current; b) flow rate profile; c) battery OCV voltage.

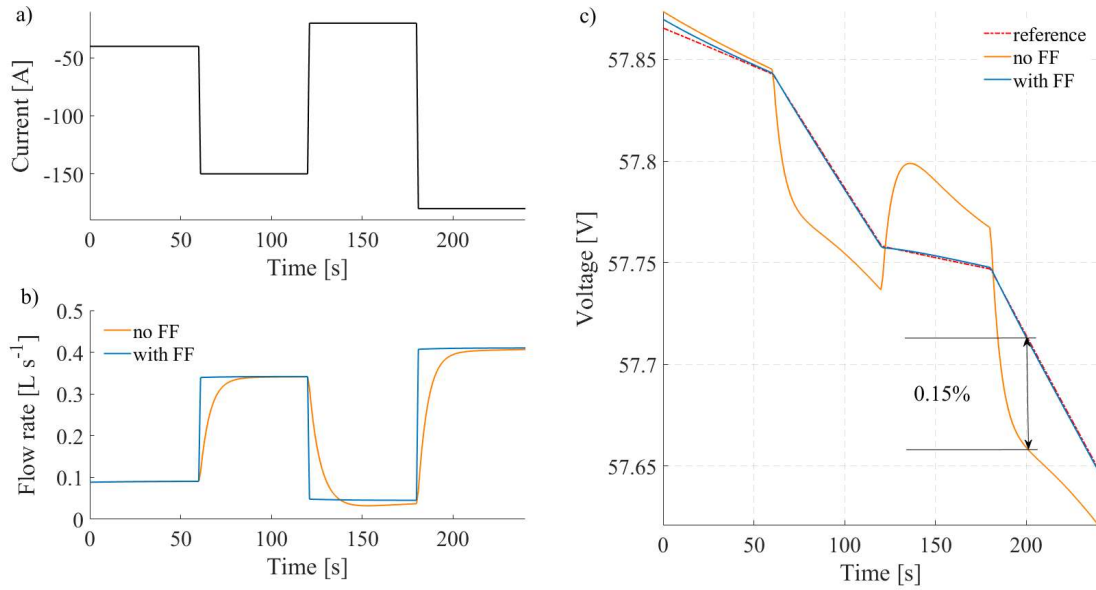


Fig. 47. Battery transient behavior in short-term discharging operation: a) loading current; b) flow rate profile; c) battery OCV voltage.

5.6.2 Long-term battery operation

In this section, we consider the battery operation in the time of one charge or discharge cycle. First, to understand the limitations of our system, we analyze battery operation under two constant flow rates of $Q_{min} = 0.05 \text{ L s}^{-1}$ and $Q_{max} = 1.0 \text{ L s}^{-1}$, further referred to as minimum and maximum flow rates, respectively. The profiles for loading current are chosen to test a wide range of operating conditions, including the most complicated cases for battery operation with several sudden surges during charge (Fig. 48a) and discharge modes (Fig. 49a).

As expected, the simulations with maximum flow rate demonstrate good battery behavior in the whole range of operating SOC's both in charge (Fig. 48d) and discharge

modes (Fig. 49d), proving that the considered profiles are chosen in a proper way, and the battery can follow them fulfilling the loading requirements.

On the next step, operation with a minimum flow rate is simulated. The results show that this flow rate allows keeping the output power quite high despite the changes in loading profile at the beginning of both charge and discharge modes even at high jumps of current (Fig. 48d and 49d). Nevertheless, the deviations of battery power in comparison to the operation with the maximum flow rate can be observed. Moreover, in charge, after the time of 4200s, the battery power notably increased, and finally, the battery stops operation at the time of 4800s due to reaching the higher cut-off voltage. This behavior can be attributed to the fact that at the beginning of the charging process, at lower SOCs, electrolytes contained a large amount of active species (V^{+3} and V^{+4} ions) sufficient for electrochemical conversion in battery charge mode. However, with time during charging process, the electrolytes become depleted, containing a lower concentration of active reactants. That, in turn, increases the mass transport polarization in the cell leading to higher concentration overvoltages [43] and, as a result, higher battery voltage. Thus, the upper cut-off voltage is reached earlier and further battery operation is terminated. In discharge processes, we have observed the opposite behavior: the battery power significantly reduces after crossing the point of 4000 s. Finally, the battery is switched off at the time of 4600 s due to the reaching of lower cut-off voltage. This behavior can be explained in the same way as in the charging process. The active species (V^{+2} and V^{+5} ions in this case) also became limited

at the end of the process leading to higher concentration overvoltages and faster reaching of lower cut-off voltage.

After that, operation with a variable electrolyte flow rate was simulated. The results show that the proposed control strategy can ensure stable battery operation in the whole range of operating SOCs with the output power very close to that obtained at a maximum flow rate (the average deviation less than 1 % both in charge (Fig. 48d) in discharge modes (Fig. 49d)). One can see that the values of the flow rate determined by the controller were significantly lower than the maximum flow rate for all considered changes in the loading profile. For example, in charge, at the time of 4500 s, the controlled flow rate was 0.45 L s^{-1} , which was more than two times less than the maximum flow rate (1 L s^{-1}). Such a reduction of flow rate can notably improve the total energy efficiency of the battery and reduce pressure drops in the cells. In order to evaluate these effects, we perform some estimations for the pressure drop in the system and pumps energy consumption. As can be seen from Eq. (62), the pressure drop in the cell is linearly proportional to the flow rate. Therefore, the reduction in flow rate by two times also leads to the same reduction in pressure drop. Furthermore, lower pressure drops result in slower mechanical degradation and lower possibility of leakages, thus improving system reliability and lifetime. According to Eq. (63), pumps' power consumption is proportional to the squared flow rate, and the reduction in flow rate by two times reduces the power consumption by four times.

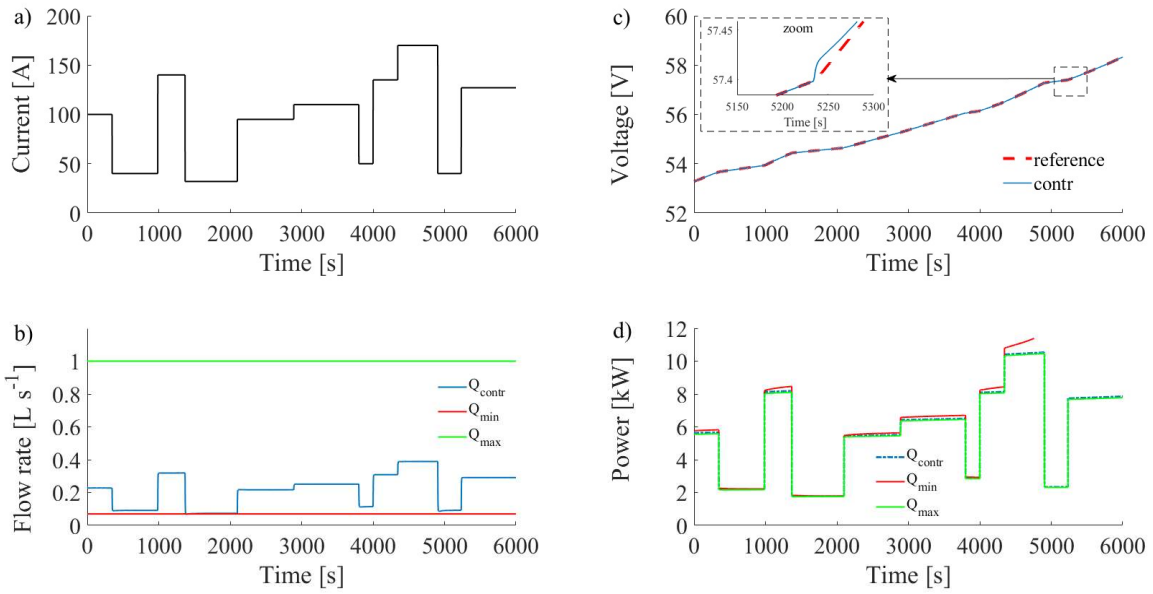


Fig. 48. Battery operation in charging process at different flow rates: a) loading current; b) flow rates; c) reference and actual OCVs; d) battery power; green line – $Q_{max} = 1.0 \text{ L s}^{-1}$; red line – $Q_{min} = 0.05 \text{ L s}^{-1}$; blue line – Q_{contr} the proposed control strategy.

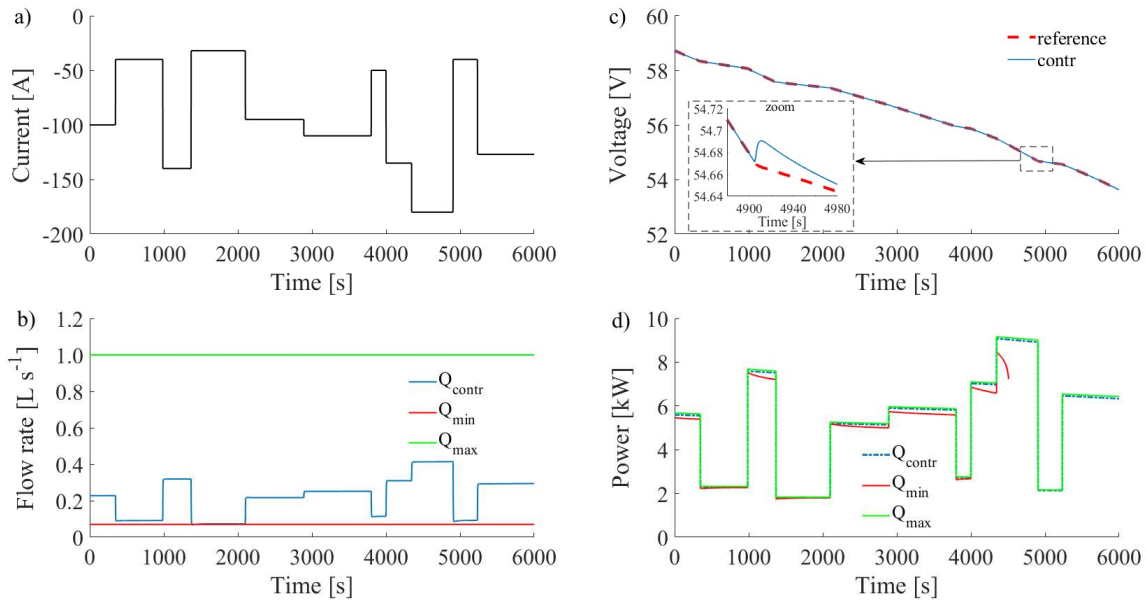


Fig. 49. Battery operation in discharging process at different flow rates. a) loading current. b) flow rates. c) reference and actual OCVs. d) battery power; green line – $Q_{max} = 1.0 \text{ L s}^{-1}$; red line – $Q_{min} = 0.05 \text{ L s}^{-1}$; blue line – Q_{contr} the proposed control strategy.

The proposed control strategy is also compared with the strategy developed by Li [67], where the authors proposed a controller aimed to ensure the constant electrochemical conversion in the cell. The electrochemical conversion shows the number of ions used in the reactions for a fixed elementary volume of electrolyte passing through a cell during battery operation. Thus, the higher conversion means higher usage of electrolyte in a single electrolyte pass. The conversion can be controlled by the electrolyte flow rate that regulates electrolyte refreshment in the cell, and therefore, a higher flow rate ensures lower conversion in the cell.

For comparison, we have considered one of the loading profiles from [67] (here we present only the results related to discharge operation, while similar effects have also been observed for a charge). The results of simulations show that our approach can ensure nearly the same battery performance providing notably lower flow rates (Fig. 50). This fact can be specially noticed at high SOC (for a charge) and low SOC (for discharge) when the difference between the flow rates is more than two times, while the difference in the corresponding powers was less than 1 %. It can be addressed to the fact that the fixed conversion ratio is a very strict condition that can be fulfilled only with high flow rates at a low concentration of reactants that takes place at the end of charge or discharge processes. However, at the end of these processes, the low conversion rate is not essential, as it does not notably improve the battery voltage, and thus, a higher conversion rate at the end of charge and discharge (observed in our approach) does not significantly reduce battery power. In order to estimate the effect of flow rate difference on the battery energy efficiency and degradation, we use Eq.(62) considering the maximum difference between the flow rates that was around 1.5 times at the time of 5700 s, resulting in a pressure drop difference of 1.5 times.

The pumps energy consumption can be estimated by integration of Eq.(63) over the operation time (τ):

$$E_{pump} = \int_0^{\tau} P_{pump} dt = \int_0^{\tau} \frac{\Delta p Q}{\varepsilon_{pump}} dt \quad (65)$$

The estimation of pumping losses (Eq.(65)) revealed that pumps operating with our strategy consume 45 kJ of energy while the strategy of [29] results in a consumption of 145

kJ that is more than three times higher. Therefore, our strategy notably decreases pressure drops resulting in smaller mechanical degradation of internal battery components and improves the energy performance of the battery.

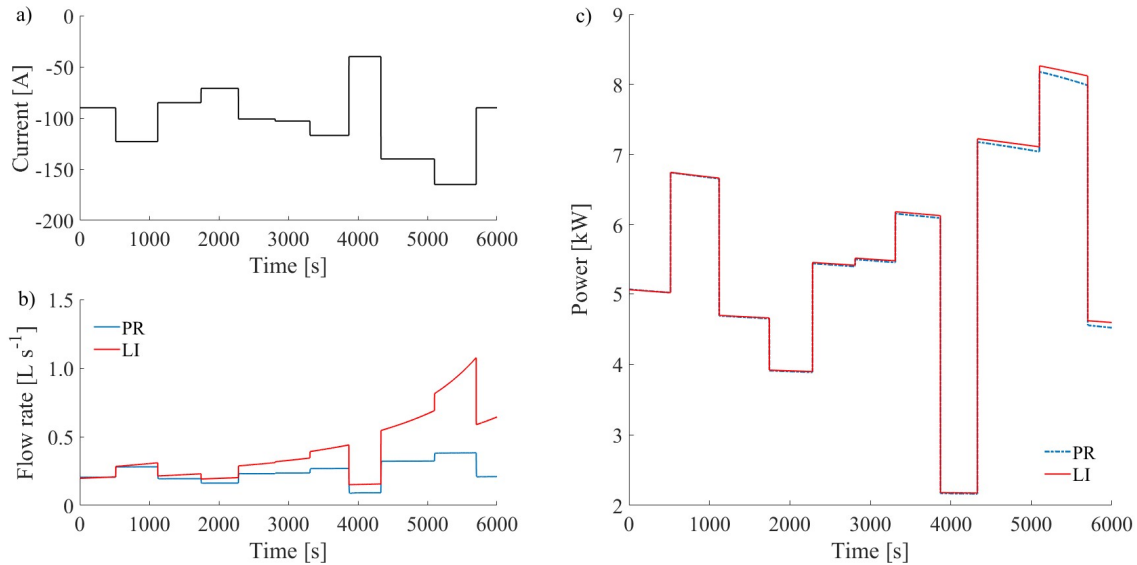


Fig. 50. Discharging process: a) loading current; b) flow rates; c) battery power; PR – control strategy proposed in this study; Li – control strategy proposed in [67].

5.7 Conclusions

The control system for the electrolyte flow rate is an important and unique component of the flow battery management system since the flow rate provides fresh electrolyte assuring the required output power. It is especially important at fast changes in power demand as they require corresponding responses in flow rate for stable battery operation. In addition, the flow rate affects the battery energy efficiency changing the pumps' power consumption. Therefore, the variable flow rate gives additional flexibility

for a set of optimal operating conditions in order to improve battery energy efficiency and ensure its reliable operation at fluctuating loads. In this study, we have proposed an optimal strategy for a closed-loop control system suitable for application in practical control-monitoring tools. The main findings of this chapter can be summarized as follows:

(1) A new multilevel hierarchy of VRFB flow rate control tasks has been proposed. The hierarchy consists of three levels of control, where each level is responsible for the regulation of flow rate related processes depending on their characteristic times. Hence, the entire control system can be decomposed into three parts (designed independently) that significantly simplifies the logic of control strategy while making it more robust, reliable and simpler for implementation.

(2) A novel approach for the determination of optimal battery OCV (for 2nd control level) has been derived using the parametric-sweep calculations with varied flow rates. The proposed approach provides low flow rates keeping battery OCV rather close (98%) to the one obtained for maximum flow rate. It was shown that the OCV obtained in the framework of the proposed strategy could be chosen as a reference for closed-loop control systems that significantly simplifies the control algorithm.

(3) A feedback control system for flow rate regulation at dynamically changing conditions has been developed. The results show that the application of a simple PI controller capable of mitigating the transient battery behavior with some small deviations (less than 0.2%) from the reference trajectory. A PI plus feedforward controller can further increase the tracking accuracy (with an average error of less than 0.0005%) for all possible

spikes in the loading profile. The designed controller ensures proper battery performance providing the flows notably lower (more than two times) as compared to the existing solutions that, in turn, results in lower mechanical degradation of internal battery components. In addition, the proposed strategy reduces pumps' energy consumption by more than three times, improving overall VRFB energy efficiency.

Although in this study, a kW scale system has been considered, our approach can be easily adapted for other VRFB systems with different cell configurations and electrolyte compositions. Such adaptation can be made by alteration of various physical properties of the internal battery components, but not the governing equations that describe fundamental physical processes in the battery.

As a result, the presented approach can be used for flow rate regulation in practical systems in order to ensure their long lifetime and stable operation at varying loads. Moreover, the control algorithm has a short computational time and does not require significant computational power. Accordingly, it can be a valuable tool for the development of real-time control-monitoring software essential for the reliable operation of VRFB systems.

Chapter 6. Conclusions and future steps

The results presented in this thesis provide flexible simulation tools and insight into internal physical processes taking place in the VRFB systems, which is vital for the improvement of this technology in order to identify the most critical processes and design more efficient and reliable batteries. In addition, the developed models are essential tools for the development of advanced control strategies that could provide automated battery management and ensure long-term operation of VRFB systems without significant loss of capacity. Furthermore, the results of this study can be applied for the determination of optimal operating conditions and the development of advanced optimization techniques with individual strategies for charging and discharging that could increase the energy efficiency of VRFB facilities, ensuring, at the same time, their long-term operation.

- A zero-dimensional mathematical model for simulations of the VRFB dynamic behavior is developed. The model is based on the general physical laws of mass and energy conservation and captures the essential processes inside of the battery while demonstrating optimal tradeoff between accuracy and computational time for real-time simulations. To validate the proposed approach, original experiments have been conducted, and the model shown good agreement with experimental data (averaged error less than 4%) for a wide range of current densities that is better than the state of the art models with a similar approach.
- Detailed investigation of the crossover phenomenon (transport of vanadium ions across the membrane) is performed. First, the analytical solution for crossover flux

is derived considering all transport modes presented by diffusion, migration and convection components. The application of this solution allows simulating crossover with high accuracy, taking into account the nonlinearity of concentration profiles while it does not have significant computational complexity. The influence of different crossover components on capacity decay is systematically analyzed, revealing the considerable impact of the convection component, which dominates under diffusion and migration and mainly responsible for the observed capacity loss.

- An approach for estimating battery power and operation time dependency on different loading currents is proposed. The results showed good agreement with detailed numerical simulations while the standard method (with constant efficiencies) can overestimate the operation time more than one hour. In addition, the contribution of this study is also related to the detailed analysis of the crossover impact on capacity. The results show that crossover impact is more pronounced in discharge (more than 60% of capacity losses for all considered current densities), while during charge, it presents less than half of the total capacity drop observed. However, the share of crossover in the overall capacity fade is monotonically decreasing with the increase of current density. In addition, the influence of internal processes on the energy performance of VRFB is investigated. Energy losses in charge are mainly caused by ohmic losses, while in discharge, they are influenced by all types of internal processes.

- A control algorithm for electrolyte flow rate regulation is developed. Variable flow rate gives additional flexibility for a set of optimal operating conditions in order to improve battery energy efficiency and to ensure stable battery operation at rapidly changing loading conditions. First, an easy-to-use approach for the determination of optimal reference voltage is proposed that significantly simplifies the computational complexity of the control algorithm. The proposed method is based on the parametric sweep simulations and determination of optimal battery voltage and can be adjusted for different VRFB systems. After that, the control system based on the PI-controller interface connected with the lumped parameter model has been developed. The designed controller is able to ensure stable battery operation at dynamic loading conditions in the wide range of loading currents and operating state-of-charges (SOCs).
- Long time scale battery operation was considered with the application of loading profiles that presented the worst cases for operation in charge and in discharge. The results showed that the designed controller ensured a good regulation of flow rate for dynamic loading conditions while providing the flow rates notably lower as compared to the existing solutions that, in turn, results in lower pressure drops in the system, and thus, lower mechanical degradation of internal battery components. Therefore, the proposed strategy can be used for flow rate regulation in the efficient systems, to ensure their long lifetime and stable operation at dynamic loading conditions.

Future steps

The modeling approaches developed in this PhD thesis can naturally lead to further investigation of main challenges related to the development of more efficient, reliable and less expensive RFB systems.

In regard to that, the first direction is related to the investigation of different electrolytes based on organic redox couples that would significantly reduce the cost of the battery. To understand the behavior of RFB with different electrolytes, a zero-dimensional model developed in this work is crucial as it can be extended with different chemistries that will allow simulating the dynamic behavior of new systems, estimate their energy efficiency and indicate internal processes that should be improved.

In the second direction, more advanced control strategies should be developed that could ensure fully autonomous battery operation. Regarding that, first of all, the development of rebalancing strategies that could mitigate capacity degradation is the key point. The electrolyte imbalance is caused by the crossover in particular related to water transport across the membrane. The detailed simulation of this phenomenon is a very complicated task, while the approach proposed in this study can be further extended with water transport equations, thus providing effective tools for modeling this phenomenon.

In the third direction, the development of a Battery Management System (BMS) is very important for the stable operation of VRFB systems. BMS controls the main internal parameters in the battery and regulates them to ensure reliable battery operation while providing high efficiency and low degradation. The proposed control strategy can be

further extended with a model of inverter and converter that will provide a solid basis for the development of BMS that could ensure autonomous battery operation.

Bibliography

- [1] International Renewable Energy Agency, Global Renewables Outlook: Energy transformation 2050 (Edition: 2020), Abu Dhabi, 2020. www.irena.org/publications.
- [2] Company - Vanadis Power GmbH, (n.d.). <http://www.vanadispower.com/> (accessed January 5, 2018).
- [3] UniEnergy Technologies Announces Next Utility Deployment of UniSystem™ with Terna in Sicily, Italy - UniEnergy Technologies, (n.d.). <http://www.uettechnologies.com/news/68-unienergy-technologies-announces-next-utility-deployment-of-unisystem-tm-with-terna-in-sicily-italy> (accessed January 5, 2018).
- [4] PUD invests \$11.2 million in energy-storing units | HeraldNet.com, (n.d.). <http://www.heraldnet.com/news/pud-invests-in-11-2-million-in-energy-storing-units/> (accessed January 5, 2018).
- [5] 60MWh Redox Flow Battery Starts Operations to Deal With Renewable Energy - News - Solar Power Plant Business, (n.d.). http://techon.nikkeibp.co.jp/atclen/news_en/15mk/010500287/?ST=msbe (accessed January 5, 2018).

- [6] T. Perles, Vanadium Market Fundamentals and Implications, in: *Met. Bull. 28th Int. Ferroalloys Conf.*, 2012.
- [7] S. Rehman, L.M. Al-Hadhrami, M.M. Alam, Pumped hydro energy storage system: A technological review, *Renew. Sustain. Energy Rev.* (2015). <https://doi.org/10.1016/j.rser.2014.12.040>.
- [8] T. Ma, H. Yang, L. Lu, Feasibility study and economic analysis of pumped hydro storage and battery storage for a renewable energy powered island, *Energy Convers. Manag.* (2014). <https://doi.org/10.1016/j.enconman.2013.12.047>.
- [9] M. Budt, D. Wolf, R. Span, J. Yan, A review on compressed air energy storage: Basic principles, past milestones and recent developments, *Appl. Energy*. 170 (2016) 250–268. <https://doi.org/10.1016/j.apenergy.2016.02.108>.
- [10] B. Bolund, H. Bernhoff, M. Leijon, Flywheel energy and power storage systems, *Renew. Sustain. Energy Rev.* (2007). <https://doi.org/10.1016/j.rser.2005.01.004>.
- [11] J.M. Miller, Flywheels, in: *Handb. Automot. Power Electron. Mot. Drives*, 2017. <https://doi.org/10.1201/9781420028157>.
- [12] M. Götz, J. Lefebvre, F. Mörs, A. McDaniel Koch, F. Graf, S. Bajohr, R. Reimert, T. Kolb, Renewable Power-to-Gas: A technological and economic review, *Renew. Energy*. (2016). <https://doi.org/10.1016/j.renene.2015.07.066>.
- [13] M. Sterner, Power-to-gas, in: *Handb. Clim. Chang. Mitig. Adapt. Second Ed.*, 2016. https://doi.org/10.1007/978-3-319-14409-2_89.
- [14] U. Eberle, M. Felderhoff, F. Schüth, Chemical and physical solutions for hydrogen

- storage, *Angew. Chemie - Int. Ed.* (2009). <https://doi.org/10.1002/anie.200806293>.
- [15] S. Niaz, T. Manzoor, A.H. Pandith, Hydrogen storage: Materials, methods and perspectives, *Renew. Sustain. Energy Rev.* (2015). <https://doi.org/10.1016/j.rser.2015.05.011>.
- [16] S. Satpathy, S. Das, B.K. Bhattacharyya, How and where to use super-capacitors effectively, an integration of review of past and new characterization works on super-capacitors, *J. Energy Storage.* (2020). <https://doi.org/10.1016/j.est.2019.101044>.
- [17] L. Chen, Y. Liu, A.B. Arsoy, P.F. Ribeiro, M. Steurer, M.R. Iravani, Detailed modeling of superconducting magnetic energy storage (SMES) system, *IEEE Trans. Power Deliv.* (2006). <https://doi.org/10.1109/TPWRD.2005.864075>.
- [18] X. Zhou, B. Lu, Y. Ma, Superconducting magnetic energy storage summarize, in: *Adv. Mater. Res.*, 2012. <https://doi.org/10.4028/www.scientific.net/AMR.535-537.2057>.
- [19] M.T. Lawder, B. Suthar, P.W.C. Northrop, S. De, C.M. Hoff, O. Leitermann, M.L. Crow, S. Santhanagopalan, V.R. Subramanian, Battery energy storage system (BESS) and battery management system (BMS) for grid-scale applications, *Proc. IEEE.* 102 (2014) 1014–1030. <https://doi.org/10.1109/JPROC.2014.2317451>.
- [20] M. Skyllas-Kazacos, M.H. Chakrabarti, S. a. Hajimolana, F.S. Mjalli, M. Saleem, Progress in Flow Battery Research and Development, *J. Electrochem. Soc.* 158 (2011) R55. <https://doi.org/10.1149/1.3599565>.

- [21] WhitePaper, Electrical Energy Storage. White paper. The International Electrotechnical Commission, (IEC), Geneva, Switz. (2011). https://doi.org/10.1007/978-3-319-52311-8_1.
- [22] International Renewable Energy Agency (IRENA), Electricity storage and renewables: Costs and markets to 2030, 2017. [https://doi.org/ISBN 978-92-9260-038-9](https://doi.org/ISBN%20978-92-9260-038-9) (PDF).
- [23] H. Chen, T.N. Cong, W. Yang, C. Tan, Y. Li, Y. Ding, Progress in electrical energy storage system: A critical review, *Prog. Nat. Sci.* 19 (2009) 291–312. <https://doi.org/10.1016/j.pnsc.2008.07.014>.
- [24] X. Luo, J. Wang, M. Dooner, J. Clarke, Overview of current development in electrical energy storage technologies and the application potential in power system operation, *Appl. Energy.* 137 (2015) 511–536. <https://doi.org/10.1016/j.apenergy.2014.09.081>.
- [25] M. Aneke, M. Wang, Energy storage technologies and real life applications. A state of the art review, *Appl. Energy.* 179 (2016) 350–377. <https://doi.org/10.1016/j.apenergy.2016.06.097>.
- [26] IRENA, Electricity Storage Valuation Framework: Assessing System Value and Ensuring Project Viability, Abu Dhabi, 2020. www.irena.org/publications.
- [27] A.B. Gallo, J.R. Simoes-Moreira, H.K.M. Costa, M.M. Santos, E. Moutinho dos Santos, Energy storage in the energy transition context: A technology review, *Renew. Sustain. Energy Rev.* 65 (2016) 800–822.

- <https://doi.org/10.1016/j.rser.2016.07.028>.
- [28] SBC Energy Institute, Electricity Storage, IEA Work. Energy Storage Sep, 2013. (2013) 1–13. https://doi.org/10.1007/978-88-470-1998-0_8.
- [29] A.A. Akhil, G. Huff, A.B. Currier, B.C. Kaun, D.M. Rastler, S.B. Chen, A.L. Cotter, D.T. Bradshaw, W.D. Gauntlett, DOE/EPRI 2015 electricity storage handbook in collaboration with NRECA, Sandia Natl. Lab. (2015). <http://www.sandia.gov/ess/publications/SAND2015-1002.pdf>.
- [30] D.S. Aaron, Q. Liu, Z. Tang, G.M. Grim, A.B. Papandrew, A. Turhan, T.A. Zawodzinski, M.M. Mench, Dramatic performance gains in vanadium redox flow batteries through modified cell architecture, *J. Power Sources*. 206 (2012) 450–453. <https://doi.org/10.1016/j.jpowsour.2011.12.026>.
- [31] Z. Yang, J. Zhang, M.C.W. Kintner-Meyer, X. Lu, D. Choi, J.P. Lemmon, J. Liu, Electrochemical energy storage for green grid, *Chem. Rev.* 111 (2011) 3577–3613. <https://doi.org/10.1021/cr100290v>.
- [32] GEC 金能世纪, (n.d.). <http://www.gec.com.cn/root/web/index.php> (accessed May 11, 2020).
- [33] X. Li, H.H. Zhang, Z. Mai, H.H. Zhang, I. Vankelecom, Ion exchange membranes for vanadium redox flow battery (VRB) applications, *Energy Environ. Sci.* 4 (2011) 1147. <https://doi.org/10.1039/c0ee00770f>.
- [34] M. Rychcik, M. Skyllas-Kazacos, Characteristics of a new all-vanadium redox flow battery, *J. Power Sources*. 22 (1988). [https://doi.org/10.1016/0378-7753\(88\)80005-](https://doi.org/10.1016/0378-7753(88)80005-)

3.

- [35] C. Blanc, Modeling of a vanadium redox flow battery electricity storage system, Lab. d'Electronique Ind. PhD Thesis (2009) 263. <https://doi.org/10.5075/epfl-thesis-4277>.
- [36] Pinflow energy storage, (n.d.). <http://www.pinflowes.com/> (accessed May 11, 2020).
- [37] C. Minke, M.A. Dorantes Ledesma, Impact of cell design and maintenance strategy on life cycle costs of vanadium redox flow batteries, *J. Energy Storage*. 21 (2019) 571–580. <https://doi.org/10.1016/j.est.2018.12.019>.
- [38] V. Viswanathan, A. Crawford, D. Stephenson, S. Kim, W. Wang, B. Li, G. Coffey, E. Thomsen, G. Graff, P. Balducci, M. Kintner-Meyer, V. Sprenkle, Cost and performance model for redox flow batteries, *J. Power Sources*. 247 (2014) 1040–1051. <https://doi.org/10.1016/j.jpowsour.2012.12.023>.
- [39] U. National Minerals Information Center, Vanadium, U.S. Geol. Surv. Miner. Commod. Summ. (2016) 182–183.
- [40] T.A. Nguyen, X. Qiu, J.D. Guggenberger, M.L. Crow, A.C. Elmore, Performance characterization for photovoltaic-vanadium redox battery microgrid systems, *IEEE Trans. Sustain. Energy*. 5 (2014) 1379–1388. <https://doi.org/10.1109/TSTE.2014.2305132>.
- [41] T.A. Nguyen, D.A. Copp, R.H. Byrne, B.R. Chalamala, Market Evaluation of Energy Storage Systems Incorporating Technology-Specific Nonlinear Models,

- IEEE Trans. Power Syst. 34 (2019) 3706–3715.
<https://doi.org/10.1109/TPWRS.2019.2909764>.
- [42] C. Blanc, A. Rufer, Multiphysics and energetic modeling of a vanadium redox flow battery, 2008 IEEE Int. Conf. Sustain. Energy Technol. ICSET 2008. (2008) 696–701. <https://doi.org/10.1109/ICSET.2008.4747096>.
- [43] A. Tang, J. Bao, M. Skyllas-Kazacos, Studies on pressure losses and flow rate optimization in vanadium redox flow battery, J. Power Sources. 248 (2014) 154–162. <https://doi.org/10.1016/j.jpowsour.2013.09.071>.
- [44] A. Tang, J. Bao, M. Skyllas-Kazacos, Dynamic modelling of the effects of ion diffusion and side reactions on the capacity loss for vanadium redox flow battery, J. Power Sources. 196 (2011) 10737–10747. <https://doi.org/10.1016/j.jpowsour.2011.09.003>.
- [45] M. Skyllas-Kazacos, L. Goh, Modeling of vanadium ion diffusion across the ion exchange membrane in the vanadium redox battery, J. Memb. Sci. 399–400 (2012) 43–48. <https://doi.org/10.1016/j.memsci.2012.01.024>.
- [46] X. Li, J. Xiong, A. Tang, Y. Qin, J. Liu, C. Yan, Investigation of the use of electrolyte viscosity for online state-of-charge monitoring design in vanadium redox flow battery, Appl. Energy. 211 (2018) 1050–1059. <https://doi.org/10.1016/j.apenergy.2017.12.009>.
- [47] B. Li, Q. Luo, X. Wei, Z. Nie, E. Thomsen, B. Chen, V. Sprenkle, W. Wang, Capacity decay mechanism of microporous separator-based all-vanadium redox

- flow batteries and its recovery, *ChemSusChem*. 7 (2014) 577–584.
<https://doi.org/10.1002/cssc.201300706>.
- [48] Z. Wei, T.M. Lim, M. Skyllas-Kazacos, N. Wai, K.J. Tseng, Online state of charge and model parameter co-estimation based on a novel multi-timescale estimator for vanadium redox flow battery, *Appl. Energy*. 172 (2016) 169–179.
<https://doi.org/10.1016/j.apenergy.2016.03.103>.
- [49] Z. Wei, K.J. Tseng, N. Wai, T.M. Lim, M. Skyllas-Kazacos, Adaptive estimation of state of charge and capacity with online identified battery model for vanadium redox flow battery, *J. Power Sources*. 332 (2016) 389–398.
<https://doi.org/10.1016/j.jpowsour.2016.09.123>.
- [50] Z. Wei, A. Bhattarai, C. Zou, S. Meng, T.M. Lim, M. Skyllas-kazacos, Real-time monitoring of capacity loss for vanadium redox flow battery, *J. Power Sources*. 390 (2018) 261–269. <https://doi.org/10.1016/j.jpowsour.2018.04.063>.
- [51] M.H. Li, T. Funaki, T. Hikihara, A study of output terminal voltage modeling for redox flow battery based on charge and discharge experiments, *Fourth Power Convers. Conf. PCC-NAGOYA 2007 - Conf. Proc.* (2007) 221–225.
<https://doi.org/10.1109/PCCON.2007.372971>.
- [52] A.A. Shah, M.J. Watt-Smith, F.C. Walsh, A dynamic performance model for redox-flow batteries involving soluble species, *Electrochim. Acta*. 53 (2008) 8087–8100.
<https://doi.org/10.1016/j.electacta.2008.05.067>.
- [53] A.A. Shah, R. Tangirala, R. Singh, R.G.A. Wills, F.C. Walsh, A Dynamic Unit Cell

- Model for the All-Vanadium Flow Battery, *J. Electrochem. Soc.* 158 (2011) A671.
<https://doi.org/10.1149/1.3561426>.
- [54] M. Vynnycky, Analysis of a model for the operation of a vanadium redox battery, *Energy*. 36 (2011) 2242–2256. <https://doi.org/10.1016/j.energy.2010.03.060>.
- [55] C.L. Chen, H.K. Yeoh, M.H. Chakrabarti, An enhancement to Vynnycky's model for the all-vanadium redox flow battery, *Electrochim. Acta*. 120 (2014).
<https://doi.org/10.1016/j.electacta.2013.12.074>.
- [56] D. You, H. Zhang, J. Chen, A simple model for the vanadium redox battery, *Electrochim. Acta*. 54 (2009) 6827–6836.
<https://doi.org/10.1016/j.electacta.2009.06.086>.
- [57] X. Ma, H. Zhang, F. Xing, A three-dimensional model for negative half cell of the vanadium redox flow battery, *Electrochim. Acta*. 58 (2011) 238–246.
<https://doi.org/10.1016/j.electacta.2011.09.042>.
- [58] Q. Xu, T.S. Zhao, P.K. Leung, Numerical investigations of flow field designs for vanadium redox flow batteries, *Appl. Energy*. 105 (2013) 47–56.
<https://doi.org/10.1016/j.apenergy.2012.12.041>.
- [59] K. Oh, H. Yoo, J. Ko, S. Won, H. Ju, Three-dimensional, transient, nonisothermal model of all-vanadium redox flow batteries, *Energy*. 81 (2015) 3–14.
<https://doi.org/10.1016/j.energy.2014.05.020>.
- [60] Q. Wang, Z.G. Qu, Z.Y. Jiang, W.W. Yang, Numerical study on vanadium redox flow battery performance with non-uniformly compressed electrode and serpentine

- flow field, *Appl. Energy*. 220 (2018) 106–116.
<https://doi.org/10.1016/j.apenergy.2018.03.058>.
- [61] A. Tang, J. Bao, M. Skyllas-Kazacos, Thermal modelling of battery configuration and self-discharge reactions in vanadium redox flow battery, *J. Power Sources*. 216 (2012) 489–501. <https://doi.org/10.1016/j.jpowsour.2012.06.052>.
- [62] Y. Li, M. Skyllas-Kazacos, J. Bao, A dynamic plug flow reactor model for a vanadium redox flow battery cell, *J. Power Sources*. 311 (2016) 57–67. <https://doi.org/10.1016/j.jpowsour.2016.02.018>.
- [63] R.M. Darling, A.Z. Weber, M.C. Tucker, M.L. Perry, The Influence of Electric Field on Crossover in Redox-Flow Batteries, *J. Electrochem. Soc.* 163 (2016) A5014–A5022. <https://doi.org/10.1149/2.0031601jes>.
- [64] K.W. Knehr, E. Agar, C.R. Dennison, A.R. Kalidindi, E.C. Kumbur, A Transient Vanadium Flow Battery Model Incorporating Vanadium Crossover and Water Transport through the Membrane, *J. Electrochem. Soc.* 159 (2012) 1446–1459. <https://doi.org/10.1149/2.017209jes>.
- [65] X.-G. Yang, Q. Ye, P. Cheng, T.S. Zhao, Effects of the electric field on ion crossover in vanadium redox flow batteries, *Appl. Energy*. 145 (2015) 306–319. <https://doi.org/10.1016/j.apenergy.2015.02.038>.
- [66] K. Oh, S. Won, H. Ju, A comparative study of species migration and diffusion mechanisms in all-vanadium redox flow batteries, *Electrochim. Acta*. 181 (2015) 238–247. <https://doi.org/10.1016/j.electacta.2015.03.012>.

- [67] Y. Li, X. Zhang, J. Bao, M. Skyllas-Kazacos, Control of electrolyte flow rate for the vanadium redox flow battery by gain scheduling, *J. Energy Storage*. 14 (2017) 125–133. <https://doi.org/10.1016/j.est.2017.10.005>.
- [68] D.S. Aaron, Q. Liu, Z. Tang, G.M. Grim, A.B. Papandrew, A. Turhan, T.A. Zawodzinski, M.M. Mench, Dramatic performance gains in vanadium redox flow batteries through modified cell architecture, *J. Power Sources*. 206 (2012) 450–453. <https://doi.org/10.1016/j.jpowsour.2011.12.026>.
- [69] Y. Ashraf Gandomi, D.S. Aaron, M.M. Mench, Coupled Membrane Transport Parameters for Ionic Species in All-Vanadium Redox Flow Batteries, *Electrochim. Acta*. 218 (2016) 174–190. <https://doi.org/10.1016/j.electacta.2016.09.087>.
- [70] D. You, H. Zhang, C. Sun, X. Ma, Simulation of the self-discharge process in vanadium redox flow battery, *J. Power Sources*. 196 (2011) 1578–1585. <https://doi.org/10.1016/j.jpowsour.2010.08.036>.
- [71] M. Mulder, Basic Principles of Membrane Technology, *Zeitschrift Für Phys. Chemie*. (1996) 564. https://doi.org/10.1524/zpch.1998.203.Part_1_2.263.
- [72] A.Z. Weber, J. Newman, Transport in Polymer-Electrolyte Membranes. Part 1. Physical model, *J. Electrochem. Soc.* 150 (2003) 1008–1015. https://doi.org/10.1007/978-0-387-78691-9_6.
- [73] X.L. Zhou, T.S. Zhao, L. An, Y.K. Zeng, L. Wei, Modeling of ion transport through a porous separator in vanadium redox flow batteries, *J. Power Sources*. 327 (2016) 67–76. <https://doi.org/10.1016/j.jpowsour.2016.07.046>.

- [74] W.W. Yang, Y.L. He, Y.S. Li, Performance Modeling of a Vanadium Redox Flow Battery during Discharging, *Electrochim. Acta.* 155 (2015). <https://doi.org/10.1016/j.electacta.2014.12.138>.
- [75] X. You, Q. Ye, P. Cheng, The dependence of mass transfer coefficient on the electrolyte velocity in carbon felt electrodes: Determination and validation, *J. Electrochem. Soc.* 164 (2017). <https://doi.org/10.1149/2.0401711jes>.
- [76] D. Schmal, J. Van Erkel, P.J. Van Duin, Mass transfer at carbon fibre electrodes, *J. Appl. Electrochem.* 16 (1986) 422–430. <https://doi.org/10.1007/BF01008853>.
- [77] J.D. Milshtein, K.M. Tenny, J.L. Barton, J. Drake, R.M. Darling, F.R. Brushett, Quantifying Mass Transfer Rates in Redox Flow Batteries, *J. Electrochem. Soc.* 164 (2017) E3265–E3275. <https://doi.org/10.1149/2.0201711jes>.
- [78] M.S. Kondratenko, E.A. Karpushkin, N.A. Gvozdik, M.O. Gallyamov, K.J. Stevenson, V.G. Sergeyev, Influence of aminosilane precursor concentration on physicochemical properties of composite Nafion membranes for vanadium redox flow battery applications, *J. Power Sources.* 340 (2017) 32–39. <https://doi.org/10.1016/j.jpowsour.2016.11.045>.
- [79] Q. Luo, L. Li, Z. Nie, W. Wang, X. Wei, B. Li, B. Chen, Z. Yang, In-situ investigation of vanadium ion transport in redox flow battery, *J. Power Sources.* 218 (2012) 15–20. <https://doi.org/10.1016/j.jpowsour.2012.06.066>.
- [80] D. Aaron, Z. Tang, A.B. Papandrew, T.A. Zawodzinski, Polarization curve analysis of all-vanadium redox flow batteries, *J. Appl. Electrochem.* 41 (2011) 1175–1182.

<https://doi.org/10.1007/s10800-011-0335-7>.

- [81] Q. Xu, T.S. Zhao, Determination of the mass-transport properties of vanadium ions through the porous electrodes of vanadium redox flow batteries, *Phys. Chem. Chem. Phys.* 15 (2013) 10841. <https://doi.org/10.1039/c3cp51944a>.
- [82] Y.A. Gandomi, D.S. Aaron, T.A. Zawodzinski, M.M. Mench, In Situ Potential Distribution Measurement and Validated Model for All-Vanadium Redox Flow Battery, *J. Electrochem. Soc.* 163 (2016) A5188–A5201. <https://doi.org/10.1149/2.0211601jes>.
- [83] R.L. Fares, J.P. Meyers, M.E. Webber, A dynamic model-based estimate of the value of a vanadium redox flow battery for frequency regulation in Texas, *Appl. Energy.* 113 (2014) 189–198. <https://doi.org/10.1016/j.apenergy.2013.07.025>.
- [84] E. Hittinger, J.F. Whitacre, J. Apt, What properties of grid energy storage are most valuable?, *J. Power Sources.* 206 (2012) 436–449. <https://doi.org/10.1016/j.jpowsour.2011.12.003>.
- [85] Q. Zheng, X. Li, Y. Cheng, G. Ning, F. Xing, H. Zhang, Development and perspective in vanadium flow battery modeling, *Appl. Energy.* 132 (2014). <https://doi.org/10.1016/j.apenergy.2014.06.077>.
- [86] A. Bhattacharjee, A. Roy, N. Banerjee, S. Patra, H. Saha, Precision dynamic equivalent circuit model of a Vanadium Redox Flow Battery and determination of circuit parameters for its optimal performance in renewable energy applications, *J. Power Sources.* 396 (2018) 506–518.

<https://doi.org/10.1016/j.jpowsour.2018.06.017>.

- [87] H. Chen, X. Li, H. Gao, J. Liu, C. Yan, A. Tang, Numerical modelling and in-depth analysis of multi-stack vanadium flow battery module incorporating transport delay, *Appl. Energy*. 247 (2019) 13–23. <https://doi.org/10.1016/j.apenergy.2019.04.034>.
- [88] B.W. Zhang, Y. Lei, B.F. Bai, A. Xu, T.S. Zhao, A two-dimensional mathematical model for vanadium redox flow battery stacks incorporating nonuniform electrolyte distribution in the flow frame, *Appl. Therm. Eng.* 151 (2019) 495–505. <https://doi.org/10.1016/j.applthermaleng.2019.02.037>.
- [89] M.Y. Lu, W.W. Yang, Y.M. Deng, W.Z. Li, Q. Xu, Y.L. He, Mitigating capacity decay and improving charge-discharge performance of a vanadium redox flow battery with asymmetric operating conditions, *Electrochim. Acta*. 309 (2019). <https://doi.org/10.1016/j.electacta.2019.04.032>.
- [90] K. Oh, M. Moazzam, G. Gwak, H. Ju, Water crossover phenomena in all-vanadium redox flow batteries, *Electrochim. Acta*. 297 (2019) 101–111. <https://doi.org/10.1016/j.electacta.2018.11.151>.
- [91] M. Resch, J. Bühler, B. Schachler, R. Kunert, A. Meier, A. Sumper, Technical and economic comparison of grid supportive vanadium redox flow batteries for primary control reserve and community electricity storage in Germany, *Int. J. Energy Res.* 43 (2019) 337–357. <https://doi.org/10.1002/er.4269>.
- [92] P. Mazúr, J. Mrlík, J. Beneš, J. Pociďič, J. Vrána, J. Dundálek, J. Kosek, Performance evaluation of thermally treated graphite felt electrodes for vanadium

- redox flow battery and their four-point single cell characterization, *J. Power Sources*. 380 (2018) 105–114. <https://doi.org/10.1016/j.jpowsour.2018.01.079>.
- [93] B. Zakeri, S. Syri, Electrical energy storage systems: A comparative life cycle cost analysis, *Renew. Sustain. Energy Rev.* 42 (2015) 569–596. <https://doi.org/10.1016/j.rser.2014.10.011>.
- [94] C. Minke, U. Kunz, T. Turek, Techno-economic assessment of novel vanadium redox flow batteries with large-area cells, *J. Power Sources*. 361 (2017) 105–114. <https://doi.org/10.1016/j.jpowsour.2017.06.066>.
- [95] A. Cunha, J. Martins, N. Rodrigues, F.P. Brito, Vanadium redox flow batteries: A technology review, *Int. J. Energy Res.* 39 (2015). <https://doi.org/10.1002/er.3260>.
- [96] Y.K. Zeng, T.S. Zhao, L. An, X.L. Zhou, L. Wei, A comparative study of all-vanadium and iron-chromium redox flow batteries for large-scale energy storage, *J. Power Sources*. 300 (2015) 438–443. <https://doi.org/10.1016/j.jpowsour.2015.09.100>.
- [97] X. Ma, H. Zhang, C. Sun, Y. Zou, T. Zhang, An optimal strategy of electrolyte flow rate for vanadium redox flow battery, *J. Power Sources*. 203 (2012) 153–158. <https://doi.org/10.1016/j.jpowsour.2011.11.036>.
- [98] R. Badrinarayanan, K.J. Tseng, B.H. Soong, Z. Wei, Modelling and control of vanadium redox flow battery for profile based charging applications, *Energy*. 141 (2017) 1479–1488. <https://doi.org/10.1016/j.energy.2017.11.082>.
- [99] B. Turker, S. Arroyo Klein, E.M. Hammer, B. Lenz, L. Komsijska, Modeling a

- vanadium redox flow battery system for large scale applications, *Energy Convers. Manag.* 66 (2013) 26–32. <https://doi.org/10.1016/j.enconman.2012.09.009>.
- [100] M. Martinez, M. Gustavo Molina, P. Enrique Mercado, Optimal sizing method of vanadium redox flow battery to provide load frequency control in power systems with intermittent renewable generation, *IET Renew. Power Gener.* 11 (2017) 1804–1811. <https://doi.org/10.1049/iet-rpg.2016.0798>.
- [101] R.M. Darling, K.G. Gallagher, J.A. Kowalski, S. Ha, F.R. Brushett, Pathways to low-cost electrochemical energy storage: a comparison of aqueous and nonaqueous flow batteries, *Energy Environ. Sci.* 7 (2014) 3459–3477. <https://doi.org/10.1039/C4EE02158D>.
- [102] R.D. Dmello, J.D. Milshtein, F.R. Brushett, K.C. Smith, Cost-Driven Materials Selection Criteria for Redox Flow Battery Electrolytes, *J. Power Sources.* 330 (2016) accepted. <https://doi.org/10.1016/j.jpowsour.2016.08.129>.
- [103] D. Stephenson, S. Kim, F. Chen, E. Thomsen, V. Viswanathan, W. Wang, V. Sprenkle, Electrochemical Model of the Fe/V Redox Flow Battery, *J. Electrochem. Soc.* 159 (2012) A1993–A2000. <https://doi.org/10.1149/2.052212jes>.
- [104] X. Zhang, Y. Li, M. Skyllas-Kazacos, J. Bao, Optimal sizing of vanadium redox flow battery systems for residential applications based on battery electrochemical characteristics, *Energies.* 9 (2016). <https://doi.org/10.3390/en9100857>.
- [105] A. Bhattarai, N. Wai, R. Schweiss, A. Whitehead, G.G. Scherer, P.C. Ghimire, T.M. Lim, H.H. Hng, Vanadium redox flow battery with slotted porous electrodes and

- automatic rebalancing demonstrated on a 1 kW system level, *Appl. Energy*. 236 (2019) 437–443. <https://doi.org/10.1016/j.apenergy.2018.12.001>.
- [106] W.W. Yang, F.Y. Yan, Z.G. Qu, Y.L. He, Effect of various strategies of soc-dependent operating current on performance of a vanadium redox flow battery, *Electrochim. Acta*. 259 (2018) 772–782. <https://doi.org/10.1016/j.electacta.2017.10.201>.
- [107] V.K. Yu, D. Chen, Peak power prediction of a vanadium redox flow battery, *J. Power Sources*. 268 (2014). <https://doi.org/10.1016/j.jpowsour.2014.06.053>.
- [108] A. Tang, J. McCann, J. Bao, M. Skyllas-Kazacos, Investigation of the effect of shunt current on battery efficiency and stack temperature in vanadium redox flow battery, *J. Power Sources*. 242 (2013) 349–356. <https://doi.org/10.1016/j.jpowsour.2013.05.079>.
- [109] P. Zhao, H. Zhang, H. Zhou, J. Chen, S. Gao, B. Yi, Characteristics and performance of 10kW class all-vanadium redox-flow battery stack, *J. Power Sources*. 162 (2006) 1416–1420. <https://doi.org/10.1016/j.jpowsour.2006.08.016>.
- [110] C. Sun, J. Chen, H. Zhang, X. Han, Q. Luo, Investigations on transfer of water and vanadium ions across Nafion membrane in an operating vanadium redox flow battery, *J. Power Sources*. 195 (2010) 890–897. <https://doi.org/10.1016/j.jpowsour.2009.08.041>.
- [111] M. Pugach, M. Kondratenko, S. Briola, A. Bischi, Numerical and experimental study of the flow-by cell for Vanadium Redox Batteries, *Energy Procedia*. 142

- (2017) 3667–3674. <https://doi.org/10.1016/j.egypro.2017.12.260>.
- [112] M. Pugach, M. Kondratenko, S. Briola, A. Bischi, Zero dimensional dynamic model of vanadium redox flow battery cell incorporating all modes of vanadium ions crossover, *Appl. Energy*. 226 (2018) 560–569. <https://doi.org/10.1016/j.apenergy.2018.05.124>.
- [113] B. Xiong, J. Zhao, K.J. Tseng, M. Skyllas-Kazacos, T.M. Lim, Y. Zhang, Thermal hydraulic behavior and efficiency analysis of an all-vanadium redox flow battery, *J. Power Sources*. 242 (2013) 314–324. <https://doi.org/10.1016/j.jpowsour.2013.05.092>.
- [114] L.F. Arenas, C. Ponce de León, F.C. Walsh, Redox flow batteries for energy storage: their promise, achievements and challenges, *Curr. Opin. Electrochem.* 16 (2019) 117–126. <https://doi.org/10.1016/j.coelec.2019.05.007>.
- [115] L.F. Arenas, C. Ponce de León, F.C. Walsh, Engineering aspects of the design, construction and performance of modular redox flow batteries for energy storage, *J. Energy Storage*. 11 (2017). <https://doi.org/10.1016/j.est.2017.02.007>.
- [116] C.Y. Ling, H. Cao, M.L. Chng, M. Han, E. Birgersson, Pulsating electrolyte flow in a full vanadium redox battery, *J. Power Sources*. 294 (2015) 305–311. <https://doi.org/10.1016/j.jpowsour.2015.06.020>.
- [117] S. Konig, M.R. Suriyah, T. Leibfried, Model based examination on influence of stack series connection and pipe diameters on efficiency of vanadium redox flow batteries under consideration of shunt currents, 281 (2015) 272–284.

<https://doi.org/10.1016/j.jpowsour.2015.01.119>.

- [118] D.K. Kim, S.J. Yoon, J. Lee, S. Kim, Parametric study and flow rate optimization of all-vanadium redox flow batteries, *Appl. Energy*. 228 (2018) 891–901. <https://doi.org/10.1016/j.apenergy.2018.06.094>.
- [119] M. Guarnieri, A. Trovò, F. Picano, Enhancing the efficiency of kW-class vanadium redox flow batteries by flow factor modulation: An experimental method, *Appl. Energy*. 262 (2020) 114532. <https://doi.org/10.1016/j.apenergy.2020.114532>.
- [120] W. Xiao, L. Tan, Control strategy optimization of electrolyte flow rate for all vanadium redox flow battery with consideration of pump, *Renew. Energy*. 133 (2018) 1445–1454. <https://doi.org/10.1016/j.renene.2018.09.018>.
- [121] C. Blanc, A. Rufer, Optimization of the operating point of a vanadium redox flow battery, 2009 IEEE Energy Convers. Congr. Expo. ECCE 2009. (2009) 2600–2605. <https://doi.org/10.1109/ECCE.2009.5316566>.
- [122] T. Wang, J. Fu, M. Zheng, Z. Yu, Dynamic control strategy for the electrolyte flow rate of vanadium redox flow batteries, *Appl. Energy*. 227 (2018) 613–623. <https://doi.org/10.1016/j.apenergy.2017.07.065>.
- [123] J. Fu, M. Zheng, D. Ph, X. Wang, J. Sun, T. Wang, Flow-Rate Optimization and Economic Analysis of Vanadium Redox Flow Batteries in a Load-Shifting Application, 143 (2017) 1–13. [https://doi.org/10.1061/\(ASCE\)EY.1943-7897.0000493](https://doi.org/10.1061/(ASCE)EY.1943-7897.0000493).
- [124] S. König, M.R. Suriyah, T. Leibfried, Innovative model-based flow rate

- optimization for vanadium redox flow batteries, *J. Power Sources*. 333 (2016) 134–144. <https://doi.org/10.1016/j.jpowsour.2016.09.147>.
- [125] M. Averbukh, A. Pozin, S. Sukoriansky, Electrolyte Pumping Optimization in Already Manufactured Vanadium Redox Battery Based on Experimentally Determined Electrical and Hydrodynamic Losses, *J. Energy Eng.* 143 (2017) 1–12. [https://doi.org/10.1061/\(ASCE\)EY.1943-7897.0000398](https://doi.org/10.1061/(ASCE)EY.1943-7897.0000398).
- [126] Y. Li, X. Zhang, J. Bao, M. Skyllas-kazacos, Studies on optimal charging conditions for vanadium redox flow batteries, *J. Energy Storage*. 11 (2017) 191–199. <https://doi.org/10.1016/j.est.2017.02.008>.
- [127] M.P. Akter, Y. Li, J. Bao, M. Skyllas-Kazacos, M.F. Rahman, M.P. Akter, Y. Li, J. Bao, M. Skyllas-Kazacos, M.F. Rahman, Optimal Charging of Vanadium Redox Flow Battery with Time-Varying Input Power, *Batter.* 2019, Vol. 5, Page 20. 5 (2019) 20. <https://doi.org/10.3390/BATTERIES5010020>.
- [128] H.F. Shen, X.J. Zhu, M. Shao, H.F. Cao, Neural network predictive control for vanadium redox flow battery, *J. Appl. Math.* 2013 (2013). <https://doi.org/10.1155/2013/538237>.
- [129] A. Bhattarai, N. Wai, R. Schweiss, A. Whitehead, G.G. Scherer, P.C. Ghimire, T.M. Lim, H.H. Hng, Vanadium redox flow battery with slotted porous electrodes and automatic rebalancing demonstrated on a 1 kW system level, *Appl. Energy*. 236 (2019) 437–443. <https://doi.org/10.1016/j.apenergy.2018.12.001>.
- [130] Y. Zhang, L. Liu, J. Xi, Z. Wu, X. Qiu, The benefits and limitations of electrolyte

- mixing in vanadium flow batteries, *Appl. Energy*. 204 (2017) 373–381.
<https://doi.org/10.1016/j.apenergy.2017.07.049>.
- [131] G. Scherer, P. Ghimire, R. Schweiss, A. Whitehead, A. Bhattarai, N. Wai, H. Hng, Novel Approaches for Solving the Capacity Fade Problem during Operation of a Vanadium Redox Flow Battery, *Batteries*. 4 (2018) 48.
<https://doi.org/10.3390/batteries4040048>.
- [132] V. Radisavljevic-Gajic, M. Milanovic, P. Rose, Multi-Stage and Multi- Time Scale Feedback Control of Linear Systems with Applications to Fuel Cells, Springer, 2019. <https://doi.org/doi:10.1007/978-3-030-10389-7>.
- [133] B. Jiang, L. Wu, L. Yu, X. Qiu, J. Xi, A comparative study of Nafion series membranes for vanadium redox flow batteries, *J. Memb. Sci.* 510 (2016) 18–26.
<https://doi.org/10.1016/j.memsci.2016.03.007>.
- [134] J. Xi, B. Jiang, L. Yu, L. Liu, Membrane evaluation for vanadium flow batteries in a temperature range of $-20-50\text{ }^{\circ}\text{C}$, *J. Memb. Sci.* 522 (2017) 45–55.
<https://doi.org/10.1016/j.memsci.2016.09.012>.
- [135] B. Jiang, L. Yu, L. Wu, D. Mu, L. Liu, J. Xi, X. Qiu, Insights into the Impact of the Nafion Membrane Pretreatment Process on Vanadium Flow Battery Performance, *ACS Appl. Mater. Interfaces*. (2016). <https://doi.org/10.1021/acsami.6b03529>.
- [136] S. Kim, E. Thomsen, G. Xia, Z. Nie, J. Bao, K. Recknagle, W. Wang, V. Viswanathan, Q. Luo, X. Wei, A. Crawford, G. Coffey, G. Maupin, V. Sprenkle, 1 kW/1 kWh advanced vanadium redox flow battery utilizing mixed acid electrolytes,

J. Power Sources. 237 (2013) 300–309.

<https://doi.org/10.1016/j.jpowsour.2013.02.045>.

Appendix

Analytical solution for crossover flux

A porous membrane is shown in Fig A1.

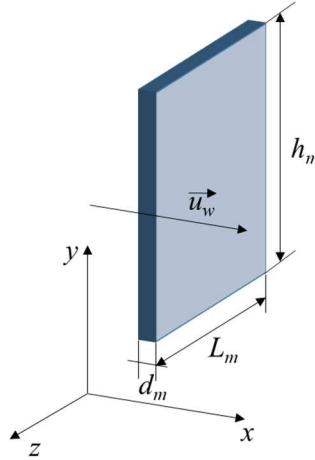


Fig. A1. Membrane and coordinate direction.

The crossover flux across the membrane is described by the Nernst-Plank equation:

$$\vec{J}_i^m = -D_i^m \nabla c_i^m - \frac{zF D_i^m c_i^m}{RT} \nabla \phi^m + \vec{u}^m c_i^m \quad (.66)$$

Where the boundary conditions are derived from the assumptions, that on the one side of the membrane the concentration of i-th ion is equal to its concentration in the cell, while on the opposite site the concentration of this ion is equal to zero due to fast chemical reactions with other ions:

$$c_{i,x}^m(0) = c_i^{ce} \quad (.67)$$

$$c_{i,x}^m(d_m) = 0 \quad (.68)$$

First, let us estimate the gradients in x, y and z directions, taking into account that the characteristic changes of the parameters inside the membrane.

The characteristic sizes of the membrane dimensions:

$$d_m \sim 10^{-4} \text{ [m]} \quad (.69)$$

$$L_m \sim 10^{-1} \text{ [m]} \quad (.70)$$

$$h_m \sim 10^{-1} \text{ [m]} \quad (.71)$$

Considering the changes of concentration, we can estimate:

$$\Delta c_{i,x}^m = c_{i,x}^m(0) - c_{i,x}^m(d_m) \sim 10^3 \text{ [mol L}^{-1}\text{]} \quad (.72)$$

Electrolyte flows in the y-direction and the cell operates in the regime when only about 10% of electrolyte are converted within one pass, thus:

$$\Delta c_{i,y}^m = c_{i,y}^m(0) - c_{i,y}^m(L_m) \sim 10^2 \text{ [mol L}^{-1}\text{]} \quad (.73)$$

In addition, the cells are designed in the way when concentration variations in the z-direction are very small and present less than 1% of the concentration in the cell:

$$\Delta c_{i,z}^m = c_{i,z}^m(0) - c_{i,z}^m(d_m) \sim 10 \text{ [mol L}^{-1}\text{]} \quad (.74)$$

As a result, the gradients in y- and z-directions are significantly smaller (4 and 5 orders of magnitude respectively) than the gradient in x-direction:

$$\frac{\frac{\Delta c_{i,y}^m}{\Delta y}}{\frac{\Delta c_{i,x}^m}{\Delta x}} \sim 10^{-4} \quad (.75)$$

$$\frac{\frac{\Delta c_{i,z}^m}{\Delta z}}{\frac{\Delta c_{i,x}^m}{\Delta x}} \sim 10^{-5} \quad (.76)$$

Similar assumptions can be performed for the estimation of the electric field gradients and water velocity that will show that they are mainly connected to the x-direction.

Hence, the initial equation (.66) can be simplified when considering only the changes in the x-direction and rewritten in the following form:

$$J_i^m = -D_i^m \frac{dc_i^m}{dx} - \frac{zFD_i^m c_i^m}{RT} \frac{d\phi^m}{dx} + u_w^m c_i^m \quad (.77)$$

The gradient of the electric field is given by the Ohm's law:

$$i = -\sigma \frac{d\phi^m}{dx} \quad (.78)$$

In addition, we assume that convection in the membrane is driven by the water flux that in turn is forced by the electro-osmotic drag:

$$N_w^m = c_w^m u_w^m = \frac{\xi i}{F} \quad (.79)$$

Thus, water velocity can be estimated as:

$$u_w^m = \frac{\xi i}{Fc_w^m} \quad (.80)$$

Finally, Eq.(.77) can be written as follows where “+” and “-“ are related to charge and discharge respectively:

$$J_i^m = -D_i^m \frac{dc_i^m}{dx} \pm \left(\frac{zFD_i^m c_i^m}{\sigma RT} + \frac{\xi c_i^m}{Fc_w^m} \right) i \quad (.81)$$

Let us make the following changes of variables assuming that the flux of i-th ion is constant along the membrane:

$$\xi = \frac{x}{d_m} \quad (.82)$$

$$\theta = \frac{c_i^m(x)}{c_i^m(0)} \quad (.83)$$

$$f = J_i^m \frac{d_m}{D_i c_i^m(0)} \quad (.84)$$

$$\chi_i = \left(\frac{zF}{\sigma RT} + \frac{\xi c_i^m}{D_i^m F c_w^m} \right) i d_m \quad (.85)$$

Then, Eq. (.81) can be written as follows:

$$f = -\frac{d\theta}{d\xi} \pm \chi_i \theta \quad (.86)$$

within the boundary conditions (.67) and (.68) can be presented as follows:

$$\theta(0) = 1 \quad (.87)$$

$$\theta(1) = 0 \quad (.88)$$

Solving Eq. (.86) within the boundary conditions of (.87) and (.88) one can obtain:

$$f = \frac{\chi_i}{e^{\chi_i} - 1} \quad (\text{for “-“}) \quad (.89)$$

$$f = \frac{\chi_i}{1 - e^{-\chi_i}} \quad (\text{for “+“}) \quad (.90)$$

Finally, taking into account Eq. (.84) we can rewrite the solution as follows:

$$J_i^m = \frac{D_i^m c_i^{ce}}{d_m} \frac{\chi_i}{e^{\chi_i} - 1} \quad (.91)$$

$$J_i^m = \frac{D_i^m c_i^{ce}}{d_m} \frac{\chi_i}{1 - e^{-\chi_i}} \quad (.92)$$